Reverberation Chamber Time and Frequency Metrology for MeerKAT Systems Shielding Evaluation

by

Joely Andrianina Andriambeloson

Dissertation presented in fulfilment of the requirements for
the degree of Doctor of Philosophy in Engineering
at the University of Stellenbosch

Promoter: Prof. Howard Charles Reader

Faculty of Engineering
Department of Electronic and Electrical Engineering,

December 2014

Declaration

By submitting this thesis electronically, I declare that the entirety of the work contained therein is my own, original work, that I am the owner of the copyright thereof (unless to the extent explicity otherwise stated) and that I have not previously in its entirety or in part submitted it for obtaining any qualification.

Date: December 2014

Abstract

Electromagnetic shielding plays a significant role in the protection of electronic equipment. Its application is essential for mitigating radio-frequency interference for the Karoo Array Telescope (MeerKAT) project in the Karoo region of the Northern Cape. In this context, time-domain (TD) methodology for small enclosure shielding effectiveness (SE) is developed using a reverberated environment technique. Interest revolves around measurement time speed-up and an extended SE response which covers the under-moded condition of small enclosures. Recommended IEC standard 61000-4-21 [1] efficiency of 0.75, for log-periodic dipole array (LPDA) antenna, is also validated from a reverberation chamber (RC) characterisation of a printed circuit-board (PCB) LPDA efficiency.

A built-in pulse generator and the Square Kilometre Array (SKA) receiver RATTY form the main elements of the TD metrology. For validation purpose, a reference coaxial airline is built. The cable is characterised with computational codes (CST and FEKO) and is also modelled with Vance and Kley's analytical expressions. The results are compared with TD transfer impedance (Z_t) measurement within the RC. The study shows that the cable fixture within an RC shapes the cable under-test (CUT) Z_t. The airline itself is also introducing an oscillating component within Z_t. The resonance is proportional to the CUT length and it is visible within the measurement data and the simulations. It is not, however, taken into account by the theoretical models.

The consequence of an incorrect antenna efficiency on RC applications is also addressed using a PCB LPDA antenna efficiency investigation. The unknown LPDA is simulated with CST for the study. The result is compared to an RC measurement validating the IEC 61000-4-21 standard efficiency recommendation of 0.75 [1]. This methodology characterised the unknown antenna parameter from a reference dipole antenna efficiency we investigated with FEKO. Simulated Wheeler-cap techniques permitted the reference antenna validation. We found that an inaccurate LPDA efficiency has little effect at higher frequency if the IEC efficiency is adopted. However, a difference of more than 7 dB can arise at low frequency if the real efficiency differs by more than 0.3 with respect to the IEC value. The study highlights the importance of a correct antenna efficiency for accurate RC applications.

The nested-enclosure technique is regarded as the conventional method of investigating small enclosures SE [2]. The technique is in general time-consuming and works for a

frequency range higher than three times the enclosure under test (EUT) lowest cut-off value. Our TD metrology covers a frequency band up to 1.4 GHz which coincides with our enclosure under-moded region. The SE characterisation is not well-documented within this particular region. The dissertation contributes to this field using a non-stirred nested-enclosure configuration. In contrast to the conventional use of the nested-enclosure methodology [2], the source is placed here within the EUT and the enclosure is treated as a normal radiator. The SE definition according to the IEEE standard in [2] is followed and the enclosure total transferred-power is computed from the port's reflection coefficient. The approach does not require a stirrer for the EUT. Our measurement shows an SE agreement between the modified and the appropriate nested-enclosure technique from 390 MHz up to 4 GHz. The investigation is faster, but in addition the TD spectrum gives a more detailed SE response than the FD approach.

Uittreksel

Elektromagnetiese skerming speel n belangrike rol in die beskerming van elektroniese komponente. Die toepassing daarvan is noodsaaklik vir die versagting van radiofrekwensie steurings in die Karoo Array Telescope (MeerKAT) projek wat tans ontwikkel word in die Karoo omgewing van die Noord-Kaap. In hierdie konteks is daar op n tydsgebied metode vir klein-omhulsel beskermingseffektiwiteit (BE) gefokus, deur gebruik te maak van n weerkatingsomgewing tegniek. Die belangstelling handel om metingstye te verkort en n uitgebreide BE reaksie wat die lae-modus toestand van klein omhulsels dek. Aanbeveelde International Electrotechnical Commission (IEC) standaard 61000-4-21 [2] effektiwiteit van 0.75, vir log-periodiese dipool-skikking (LPDA) antennas, is ook bekragtig deur n weerkaatsingskamer karakterisering van n gedrukte-stroombaanbord (PCB) LPDS antenna effektiwiteit.

n Ingeboude impulsgenerator en die Square kilometre Array (SKA) ontvanger, RATTY, vorm deel van die hoof elemente van die tydsgebiedmetings. Vir bekragtigings doeleindes is n koaksiale lugtransmissielyn gebou. Hierdie kabel is gekarakteriseer deur numeriese sagteware (CST en FEKO) en is ook gemoduleer met behulp van Vance en Kley se analitiese uitdrukkings. Die resultate is vergelyk met tydsgebied-oordragsimpedansie (Zt) metings, wat in die weerkaatsingskamer gedoen is. Die studie wys dat kabel posisie binne in die weerkaatsingskamer die Zt van die kabel-onder-toets vervorm. Die lugstreep voeg ook n ossillerende component by tot die gemete Zt. Die resonansie is eweredig aan die lengte van die kabel en is duidelik sigbaar binne die meting- en simulasiedata. Dit is egter nie in-berekening gebring in die analitiese modelle nie.

Die gevolge van n verkeerde antenna effektiwiteit in die weerkaatsingskamer toepassing is ook aangespreek deur ondersoek na die effektiwiteit van n PCB LPDA. Die onbekende LPDA is gesimuleer met CST vir hierdie studie. Die resultate is vergelyk met n weerkaatsingskamer meting, wat die IEC 61000-4-21 standaard effektiwiteit van 0.75 [1] bekragtig. Die metode karakteriseer die onbekende antenna veranderlike deur n verwysings dipool antenna effektiwiteit wat ge-ondersoek is in FEKO. Gesimuleerde Wheeler-cap tegnieke het die verifikasie van die verwysings antenna resultate toegelaat. Daar is gevind dat n onakkurate LPDA effektiwiteit n klein effek op die hoër frekwensies het, as die IEC effektiwiteit aangeneem is. Daar kan egter n verskil van 7dB voorkom by laer frekwensies, as die werklike effektiwiteit met meer as 0.3 van die IEC waarde verskil. Hierdie studie lig

die belangrikheid van n korrekte antenna effektiwiteit uit vir akkurate weerkaatsingskamer toepassings.

Die geneste-omhulsel tegniek word beskou as die konvensionele metode vir die bestudering van beskermingseffektiwiteit vir klein omhulsels. Die tegniek is gewoontlik tyd-rowend en werk net vir frekwensies wat drie maal hoër is as die af-sny waarde van die omhulsel-onder-toets. Ons tydgebiedmeting dek net n frekwensieband tot 1.4GHz, wat ooreenstem met ons omhulsel lae-modus gebied. Die beskermingseffektiwiteit karakterisering, in hierdie spesifieke veld, is nie goed gedokumenteer nie. Hierdie verhandeling dra by tot hierdie veld deur gebruik te maak van n onversteurde geneste-omhulsel konfigurasie. In teenstelling met die konvensionele gebruik van die geneste-omhulsel metode, is die bron geplaas binne die omhulsel-onder-toets en word dit gebruik as n gewone uitstraler. Die definisie van beskermingseffektiwiteit volgens die IEEE standaard in [2], is gevolg en die totale oordragskrag van die omhulsel is bereken deur gebruik te maak van n poort se refleksie koëffisiënt. Die benadering benodig nie n steurder vir die omhulsel-onder-toets nie. Ons metings se beskermingseffektiwiteit het ooreengestem met die veranderde - en die geskikte geneste-omhulsel tegniek, van 390MHz tot 4GHz in die spektrum. Hierdie ondersoek is vinniger en lewer n meer gedetailleerde beskermingseffektiwiteit reaksie as die frekwensiegebied benadering.

Acknowledgements

In the first place, my utmost gratitude and sincere praise to our Lord Jesus Christ for his limitless blessings. "But by the grace of God I am what I am", I Cor15:10.

Then my sincere acknowledgement to the following persons without whom the dissertation would not have been possible:

- My parents, sister and brother for all the encouragement and enduring support during all my studies, especially these last five years.
- Prof. Howard Reader for giving me the opportunity to do a doctoral degree in EMC and to be part of the EMRIN group. Thanks for your supervision and guidance throughout the development of the dissertation. Your feedback concerning my writing and crucial advice helped me a lot in improving my knowledge and experience.
- The South African SKA project and the National Research Foundation for the funding over the five years I have been here in Stellenbosch
- Dr Necmi Tezel, who was a Post-doctoral fellow at Stellenbosch University in 2013-2014. Big thanks for all of your valuable inputs.
- Professor P. W. Van der Walt is thanked for recommendation concerning the metallic enclosure shielding effectiveness study in chapter 5.
- Mrs Ursula Reader for proofreading my writings.
- Wessel Croukamp, Wynand Van Eeden and Lincol Saunders for the coaxial air-line and the maintenance of the reverberation chamber.
- Robert Anderson and Anneke Bester for their technical expertise during all the measurements I performed at the RF laboratory.
- the EMRIN group and all the students in the room 212 for the nice environment and for their assistance in a direct or an indirect way.

Contents

List of Figures

List of Tables

Nomenclature

ADC	Analog to Digital Converter
AUT	Antenna Under Test
AVF	Antenna Validation Factor
CEM	Computational Electromagnetic
CH1	Channel 1
CH2	Channel 2
CLF	Chamber Loading Factor
CM	Common Mode
CUT	Cable Under Test
CVF	Chamber Validation Factor
DM	Differential Mode
DUT	Device Under Test
EM	Electromagnetic
EMI	Electromagnetic Interference
EUT	Enclosure Under Test
FD	Frequency Domain
GTEM	Gigahertz Transverse Electromagnetic
ICEAA	International Conference on Electromagnetics in Advanced Applications
IEC	International Electrotechnical Commission
IEEE	Institute of Electrical and Electronics Engineers
IL	Insertion Loss
KAPB	Karoo Array Processor Building
LPDA	Log Periodic Dipole Array
LUF	Lowest Usable Frequency
MeerKAT	Karoo Array Telescopes
MoM	Method of Moment
OATS	Open Area Test Site
PCB	Printed Circuit Board
PEC	Perfect Electric Conductor
PG1	Pulse Generator 1
PG2	Pulse Generator 2
RATTY	Real Time Transient analYser
RC	Reverberation Chamber
ROACH	Reconfigurable Open Architecture Computing Hardware
SA	Spectrum Analyser
SE	Shielding Effectiveness (always a magnitude quantity, thus positive)
SKA	Square Kilometre Array
SMA	SubMiniature version A
SRD	Step Recovery Diode
ST1	Stirrer 1
ST2	Stirrer 2
SUT	Shield Under Test
TD	Time Domain
TE	Transverse Electric
TEM	Transverse electric Mode
TL	Transmission Line
TM	Transverse Magnetic
VNA	Vector Network Analyser

CHAPTER 1

Introduction

Karl Jansky discovery of cosmic radio-waves signal in August 1931 marks the beginning of the modern radio-astronomy period. This has led to various giant telescope designs for the detection of radio-waves. In this context, at the turn of the 21st century an international project was conceived for the construction of the world's largest radio telescope with the aim, among other things, of reaching back to the earliest stages of our universe's origins. The project is known as the Square Kilometre Array (SKA). Scientists and engineers are working together on the design. Currently a precursor system is being built in the Karoo region of the Northern Cape province as shown in figure 1.1. A great deal of expertise and time is being invested in this precursor system; in particular it has been recognized that a proper electromagnetic compatibility examination of the system will be crucial for the success of the project.

1.1 The SKA precursor: MeerKAT

The MeerKAT interferometer will be the most powerful radio telescope of the southern hemisphere until the SKA interferometer completion in 2024 [3]. A highly sensitive continuum survey level to μJy is expected from an interconnection of 64 dishes, with Gregorian offset configuration, where each element is similar to the one shown at the right-hand side of figure 1.1.

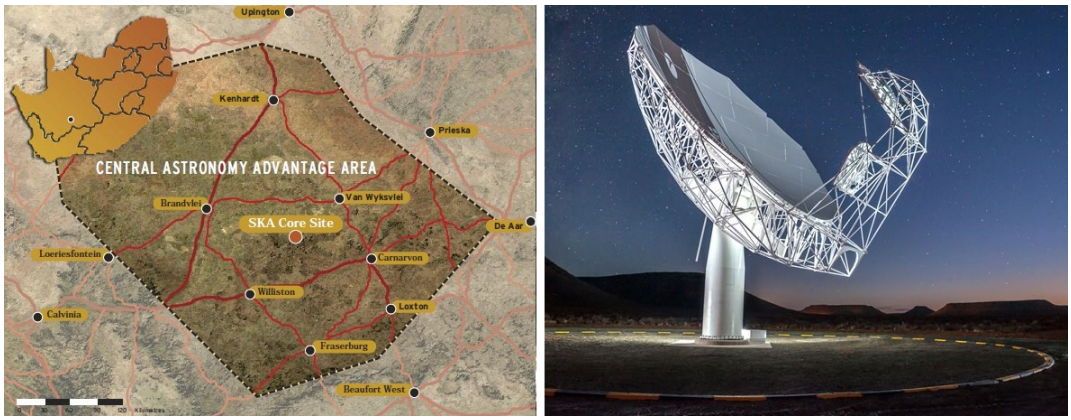

Figure 1.1: South Africa SKA core site geographical location and the first dish of the 64

A Jansky (Jy) represents the amount of radio-frequency (RF) energy per unit time, per unit area and per unit bandwidth that a radio-source in the sky emits $\left(1\ Jy = 10^{-26}\ \frac{W}{m^2 Hz}\right)$. Using a logarithmic power scale, we have $1\ Jy = -260\ \frac{dBm}{m^2 Hz}$ and this shows us how sensitive the MeerKAT interferometer is likely to be. It then becomes clear that a careful electromagnetic compatibility (EMC) examination of each stage of the design is crucial. The EMC measurements campaign started with the noise characterisation and survey of the South African SKA site in figure 1.1 many years before the MeerKAT construction. Today, the EMC investigation focuses more on signal propagation studies for shielding effectiveness (SE) optimisation and coupling cancellation.

1.2 Current EMC Development on the MeerKAT Site

The telescopes are placed at a few kilometres away from the central infrastructure, called the Karoo Array Processing Building (KAPB), where MeerKAT data will be gathered for processing. Recently, an artificial berm was constructed between the building and the telescopes to protect the core site from the radiation coming from the infrastructure. The berm SE has been characterised by the Stellenbosch University EMC group. They used a kilovolt pulse radiator [4] for time-domain (TD) SE characterisation and multi-copter measurements for aerial scan of the KAPB radiation pattern [5]. As far as the KAPB itself is concerned, it is built underground to leverage the advantage of attenuation due to the earth. Figure 1.2 and figure 1.3 show respectively the construction stages of the KAPB and the inside of the 100 dB shielded room.

Figure 1.2: KAPB development. The upper photograph shows the construction and the location of the $100dB$ shielded room of the building.

Figure 1.3: Looking up to the ceiling of the 100 dB KAPB shielded room inside the Karoo Array Processor Building

1.3 Motivation, Objectives and Methodology

Generally, the electromagnetic (EM) radiation emanating from an electronic device cannot be cancelled. It becomes clear that an enclosed environment technique constitutes the most effective and the preferred EMC technique for interference mitigation. The KAPB

design is an example of this approach, it minimises the coupling between the on-ground telescopes and the processing equipment in the building. Enclosures of various sizes will be also used inside KAPB for an internal electromagnetic interference mitigation. The dissertation takes the lead by giving an insight on small enclosures SE evaluation. The nested-enclosure technique is focused for measurement-time speed-up.

The nested-enclosure technique is based on a reverberated environment principle where the enclosure under-test and the reverberation chamber (RC) are stirred throughout a measurement. It is a time-consuming process for a standard frequency-domain analysis. The higher the number of frequencies of interest, the longer the measurement takes. In the dissertation, a TD version of the methodology is chosen for measurement-time speed-up. We believe that a wideband spectral excitation will accelerate the investigation. A TD metrology for RC application is developed in this regard using a built-in pulse generator and a sensitive SKA receiver known as the Real Time Transient analYser (RATTY).

The nested-enclosure technique is also not accurate for under-moded enclosures due to the field uniformity condition of an RC-based technique. Theoretically, this occurs for frequencies less than three times the first enclosure's resonant mode. A non-stirred-environment is focused for SE characterisations within this particular frequency range.

Antennas are extensively used in RC applications and they are represented by efficiencies in data processing. The value of 0.75 is recommended by the IEC-61000-4-21 standard for log-periodic-dipole-array antennas in case the efficiency is not known [1]. Here, the effect of an incorrect efficiency value on RC applications is examined before the enclosure SE measurements are undertaken. An efficiency characterisation methodology is presented. The study permits to de-embed the antenna contribution on measured data for accurate RC result interpretations.

1.4 Dissertation Overview

The dissertation is structured as follows:

- Chapter 2 reviews the relevant theory and literature on SE for a general understanding of the shielding principle. This introduces the reader to the main idea behind the work.
- In chapter 3, our RC calibration is examined more carefully using a proper investigation of our PCB-LPDA antenna. Simulations and measurements are compared for validation of the measured antenna efficiency. Thereafter, the new chamber

calibration factor is derived using the newly acquired LPDA efficiency.

- Chapter 4 carefully examines the Z_t of a built-in coaxial airline over a wideband up to 4 GHz. The work is concerned with our time domain metrology validation and the chapter begins with a short description of the TD chain. A frequency domain analysis is first presented to understand the cable coupling process. Afterwards, the results are compared to TD investigations for validation of the TD technique. Vance and Kley analytical coaxial cable models are considered for measurement results evaluation.
- The last main chapter of the dissertation, chapter 5, is related to the work on small enclosure SE characterisation. Here, a modified nested-enclosure setup is examined to extend the SE methodology down to enclosure under-moded condition. The approach is also intended to give a measurement time speed-up by cancelling the EUT stirrer.

CHAPTER 2

Shielding Technique Fundamentals

An electronic device and its environment are permanently in interaction through a physical process known as the electromagnetic (EM) coupling. Both parts constitute a single system satisfying Maxwell's equations, which correlate the time-varying charge within an electrical medium and the space-dependent EM-fields in its surrounding [6]. The phenomenon became clear in the twentieth century, in the beginning of the telecommunication era, when artificial EM sources diversified. Since then, engineers have used shields for electronic instruments protection against in-coming interfering signals. Fundamentals about shielding techniques are reviewed in the chapter to narrow the path for our shielded-enclosures study. In the first two sections are presented the interference coupling principles. Thereafter, in section 2.3 and section 2.3.3, analytical models of common shields that will be used in the dissertation are presented. Peer-reviewed literature on shielding is examined for a background enrichment on the topic. The shielding effectiveness SE is expressed in magnitude throughout the dissertation and will be thus referred to as a positive number.

2.1 Coupling Path Overview

The space surrounding an electronic system contains a multitude of EM-signals coming from nearby sources or self-generated by the system. Generally, the coupling happens in

four ways [7, p. 4]:

- conductive
- radiative
- capacitive
- inductive.

The conductive coupling occurs when the victim receives the unwanted signal through shared connections such as: the power network, transmission lines or the ground return-path. The three remaining paths are related to radiation and are originated from galvanic isolated interference sources. The radiative coupling represents an interference coming from a far-field plane-wave, illuminating the system. The inductive and the capacitive mechanisms refer to a near-field interaction in the receiver proximity, also known as crosstalk [8, p. 121-141]. The process can be visualised in Fig. 2.1 where the emitters symbolise the environmental sources and the receiver depicts the victim system. All the surrounding fields induce currents on the receiver metallic surfaces according to Maxwell's equations. The induced current infiltrates the system and superimposes with the output signal.

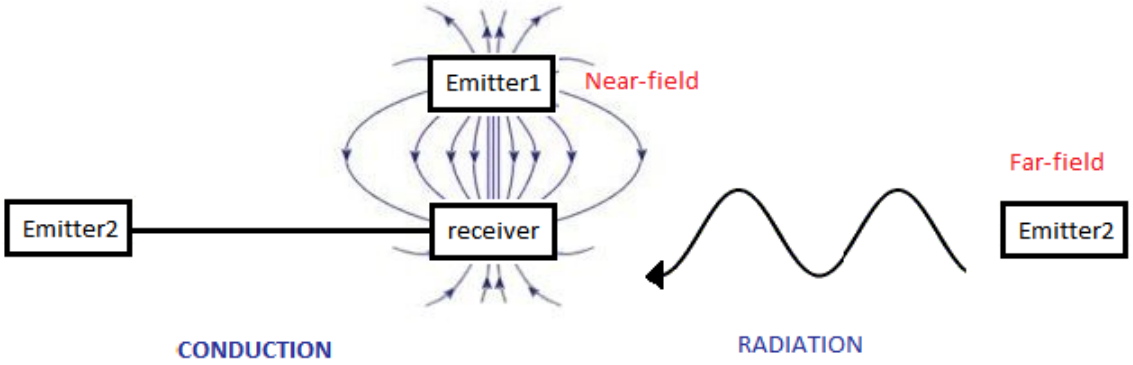

Figure 2.1: Noise coupling path illustration on electronic systems

Internally, the receiver can be subdivided into subsystems, modules and elements. Interconnected elements form a module. A network of modules defines a subsystem. An element is reducible to basic electronic parts, like a resistor, for ordinary instruments. It corresponds to equipment for large-scale design such as the Square Kilometre Array (SKA). Subsystems and modules configuration play also an important role on the interference shaping [9, p. 259-262]. As an example, on the computer's network in figure 2.2, the cabling layout forms an unwanted extra loop-circuit with each computer ground connection from the power cable. The dashed-line depicts a loop creation possibility between Module-1,

Module-2 and Module-3. The unwanted loop increases the coupling via magnetic fields. The overall system becomes vulnerable to an inductive crosstalk if the cables are not arranged properly.

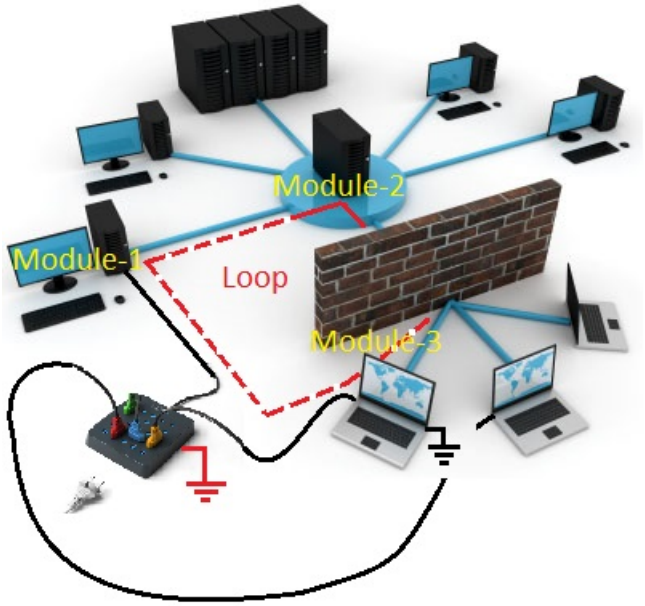

Figure 2.2: Unwanted loop-circuit creation in electronic system due to cables layout and grounding connections. The unwanted loop increases the coupling efficiency to magnetic fields.

2.2 EMI Mitigation Basics

So, EMI can be reduced using the following techniques [9, p. 259-262]:

- A noise source identification and suppression.
- A proper internal system arrangement for ground-loop minimisation
- A system partitioning, with shields, for controlled-interference environment creation.

The first two solutions are not within the scope of the dissertation. As far as the shielding technique is concerned, it is frequently used for emission reduction and for immunity improvement of electronic subsystems.

2.3 Shielding Technique: Analytical Approach

An EM shielding acts as a barrier separating the environment into two smaller domains: the noisy and the interference-controlled regions. SE expresses the ability of the shielding

material to prevent coupling between the two isolated areas. For the infinitely long shield of thickness t shown in figure 2.3, with no seam nor apertures, SE is analytically defined as the ratio of the incident and the transmitted EM fields at the same measurement location (at M) [10, 11]. The shield is removed from the test-fixture for the incident-field evaluation. Using the electric field (E-field) and the magnetic field (H-field) at M, we have:

$$SE_E = \left| 20\, log \left(\frac{\vec{E}_{Trans}(M)}{\vec{E}_{Inc}(M)} \right) \right| \qquad or \qquad SE_H = \left| 20\, log \left(\frac{\vec{H}_{Trans}(M)}{\vec{H}_{Inc}(M)} \right) \right| \tag{2.1}$$

where:

- $E_{Trans}(M)$ is the E-field measured at M when the shield is in place
- $E_{Inc}(M)$ represents the incident noise at M without the shielding.
- Note: SE will always be expressed as a magnitude throughout the dissertation.

2.3.1 Shielding Mechanism

2.3.1.1 Signal Diffusion Contribution

The incident-field from the left-hand side of figure 2.3 penetrates the shielding material after the plane-wave encounters the boundary at x = 0. The transmitted E-field (E_S) proceeds and reduces quickly due to the material skin-depth at the excitation frequency. For a finite thickness wall, multiple reflections can occur within the slab before E_S vanishes. The E-field reaching the protected-area changes with time, according to the E_S reflection progressions. SE takes the form given in (2.2) at steady state [12].

$$SE_{dB} = A_{dB} + IR_{dB} + MR_{dB} \tag{2.2}$$

where A, IR and MR represents the shield's attenuation, the reflections of the boundaries (at x=0 and x=T) and the multipath reflections within the shield.

Generally, the shield is not efficient for low-frequency signals due to the finite nature of the wall. For the wave diffusion process, the thicker the shield the better its performance at low-frequency.

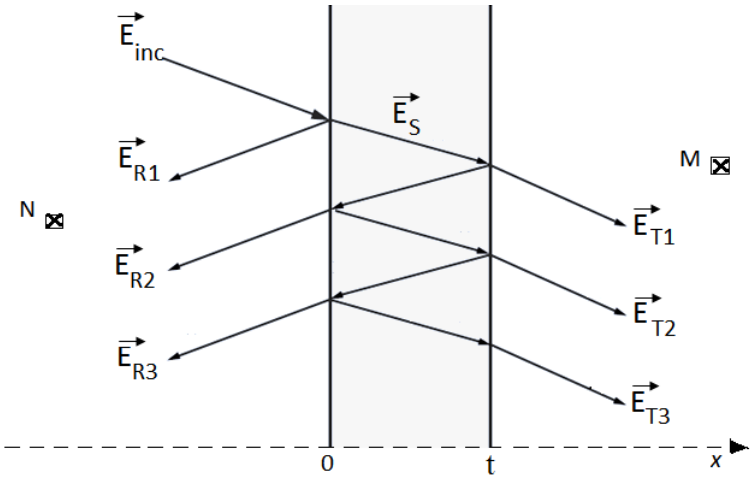

Figure 2.3: E-field multipath reflections inside an infinite length shield of thickness t

2.3.1.2 Aperture Coupling

An interfering signal also penetrates the protected region through imperfections such as apertures and seams. The aperture coupling cannot be avoided due to practical facts from communication and ventilation reasons. Many peer-reviewed articles tackle the issue using different techniques like simulation [13] and analytical models [14, 15]. But, the common ground between these studies is Bethe's theory of diffraction by small holes published in 1944 [16]. The theory is still widely used today in hole coupling problems and Kwon validated the theory experimentally in [17]. In Bethe's theory, the shield has zero thickness and an infinite shield is considered [16]. He modelled the holes diffracted fields with an effective surface magnetic currents, for a small hole case, or by simply using the magnetic and the electric dipoles given in (2.3) [18].

$$M = -\alpha_m H_0 \tag{2.3a}$$

$$N = -\alpha_e E_0 \tag{2.3b}$$

where α_m and α_e are the aperture magnetic and electric polarizabilities. H_0 and E_0 are the fields at the left-hand side of the infinite shield without holes.

The interference coupling through the aperture is analytically modelled by Robinson *et al.* in a different fashion using a transmission line (TL) theory [19, 20]. They considered a rectangular box with aperture (a slot) and which is illuminated by a plane wave in their approach. The whole process can be summarised in two steps:

- The first is the determination of the setup equivalent TL circuit model: the plane

wave is represented by a voltage source V_0 with an internal impedance of 377 Ω, and the box is characterised by an impedance Z_g with a propagation constant k_g. As far as the aperture is concerned, it is depicted by a second impedance given by Gupta *et al.* in [21].

- The electric and the magnetic shielding (SE_E and the SE_H) are afterwards calculated at a position M within the enclosure. Both are respectively analogous to the voltage and a current at the equivalent location on the TL model.

SE_E and SE_H are different and are position-dependent for the perforated rectangular enclosure [11, 22]. This is because of enclosure seams, apertures and modal resonances. This is not however the case for an infinite shield approach where $SE_E = SE_H$ [22].

2.3.2 Enclosure Definition

The concept of the infinite shield discussed above is the standard way for a shielding principle illustration. In practice, the shields are finite in size, and the interference-controlled region is isolated within an external bigger environment. Here, the term enclosure refers to a metallic casing bounding an area. It can have any particular form but in the dissertation, we focus on cylindrical and rectangular shields.

A rectangular shield is used the most for subsystems protection as shown in figure 2.4. A standing wave pattern appears within the box due to boundary conditions. This makes the field's magnitude dependent on the probe position where the field is measured. In general, the shield internal E-field measurement is complex. Additional procedures are necessary for a proper SE evaluation as will be discussed in section 2.5.

A cylindrical enclosure is often seen on coaxial cables for current return-path, and for protection of the signal flowing on the centre conductor. We are particularly interested on coaxial cables SE for two reasons. On the one hand, a coaxial cable SE is easier to measure because of the signal propagation inside the cable, which is dominated by transverse electric modes (TEM) [23]. On the other-hand, a coaxial cable is a well-known device and theoretical models are available. A reference cable is built for the work and is characterised for validation of our TD methodology.

2.3.3 Transfer Impedance for Shielding Evaluation

The transfer impedance Z_t is an alternative way of expressing SE. It is mainly used in the context of studying the shielding of cabling assemblies, especially coaxial cables. The

Figure 2.4: Rectangular enclosure for subsystems protection

external conductor of coaxial cables is commonly made from flexible, braided metallic materials. The braiding creates effective holes which are described by the notion of weave optical coverage. When the field surrounding a cable setup induces a common-mode (CM) current on the cable exterior, interference will reach the centre conductor through the shield imperfections. An electrically-short cable of length l is shown in figure 2.5 with a short-circuit connection at its input. The sketch is used for the cable Z_t per unit length definitional purposes where:

- the equivalent voltage source models the effect of surrounding fields and
- Z_{space} represents the cable external region impedance.

A differential-mode (DM) voltage is created between the cable centre and outer conductors due to I_{CM} using this schematic picture. The cable Z_t per unit length is given in (2.4) [24].

The tri-axial method is regarded as an accurate approach for Z_t determination and can be found in [24]. However, such a configuration does not represent a practical scenario and has little value for the SKA system deployments.

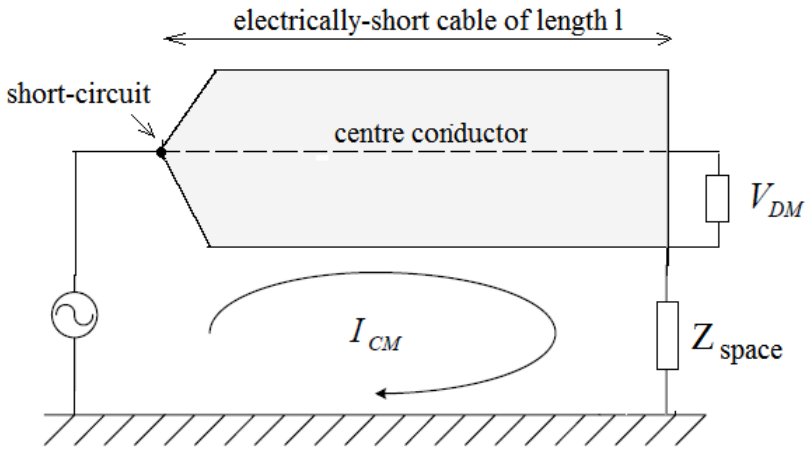

Figure 2.5: Transfer impedance in terms of CM current and DM voltage for cables SE evaluation [25]

$$Z_t\left(\Omega.m^{-1}\right) = \frac{V_{DM}}{I_{CM}}.\frac{1}{l} \tag{2.4}$$

Analytically, Z_t is a complex number (see (2.5)), where the real part (Z_d) represents the wave diffusion and the imaginary part (Z_h) expresses the interference penetration through apertures. In practical terms, we do not calculate the equivalent voltage source of figure 2.5 or Z_{space}, but rather examine the V_{DM} and I_{CM} of (2.4).

$$Z_t = Z_d + jZ_h \tag{2.5}$$

2.3.3.1 Wave Diffusion Term

Z_d is also called the Schelkunoff term and it is inversely proportional to the frequency as given in (2.6) [11, 10, 26].

$$Z_d = R_{dc}\frac{(1+j)t/\delta}{sinh[(1+j)t/\delta]} \tag{2.6}$$

where

- δ represents the cable shield skin-depth
- t is the shield thickness used in figure 2.3
- R_{dc} is defined as follows:

$$R_{dc} = \frac{1}{2\pi\sigma at} \tag{2.7}$$

$Z_t \approx Z_d$ for low-frequency signals and is dependant on the shield thickness. The thicker the cable external conductor, the lower Z_t according to (2.6).

2.3.3.2 Holes Coupling term

Conversely, the imaginary part dominates Z_t at higher frequency due to the apertures electrical size increase with the signal's wavelength. Vance investigated, analytically, the interference penetration through the holes in terms of mutual coupling M_h. For n apertures per cable unit length, M_h is given in (2.8) and $Z_h = j\omega M_h$ [27].

$$M_h = n\frac{\mu_0\alpha_m}{\pi^2 D^2} \tag{2.8}$$

where α_m is the magnetic polarizability of the aperture and D is the diameter of the shield.

Vance's model is valid for a thin-walled shield since it is established from Bethe's theory of diffraction by small holes. For thicker shields, the apertures are volumetric having a height equal to the shield thickness. Additional phenomenon, such as a chimney effect, appear when the signal penetrates the hole. Also, the EMI induces Eddy current on the hole's wall according to [28, 29]. Kley's model accounts for the extra phenomena, the mutual coupling M_h becomes:

$$M_h = \frac{k}{l} j\omega M_{LL} + \frac{k}{l}(1+j)\omega L_{SL} \tag{2.9}$$

where

- k is the number of circular holes on the cable shield
- l is the length of the coupling zone
- M_{LL} and L_{SL} are respectively called hole and skin inductances. M_{LL} accounts for the chimney effect while L_{SL} models the Eddy current contribution. M_{LL} and L_{SL} are as follows:

$$M_{LL} \approx \mu_0 \frac{0.875 r_h^3}{3\pi^2 a^2} \, exp\left(\frac{-1.84t}{r_h}\right) \tag{2.10}$$

$$L_{SL} \approx \frac{t r_h}{2a^2} \, exp\left(\frac{-2.30t}{r_h}\right) \sqrt{\frac{\mu}{2\sigma\omega}} \tag{2.11}$$

where r_h is the hole radius, t represents the shield thickness and a is the shield mean radius.

2.3.3.3 Z_t and SE Relationship

According to the IEC standard 61726 [30], a single hole Z_t can be converted to SE using the expression in (2.12) [30, 31]. The expression was proposed by Eicher and Boilot for a mode-stirred RC cable Z_t investigation and can be found in [32]. For n holes over the cable shield, however, we will make the assumption that the total Z_t is equal to the sum of each hole's contribution. This would not incorporate mutual coupling. It will be seen in 4.10 that the practical RC measurement of SE, converted through (2.12), shows good agreement with the theoretical predictions and CEM models. The derivation of (2.12) is not provided in either the standard or its related reference. A precise derivation incorporating mutual coupling was shown through FEKO simulations not to make a significant difference to the result and further on this subject was not pursued.

$$Z_t^2 + Z_f^2 = 2 Z_{space} Z_{cable} SE / l^2 \tag{2.12}$$

where Z_f is called the capacitive coupling impedance [31]. Z_{cable} and Z_{space} are the cable characteristic impedance and the impedance of the region surrounding the cable. For a cable placed within an RC: $Z_{space} = 377\,\Omega$ and $Z_f = 0$ [31].

2.4 Reverberation Chamber Fundamentals

2.4.1 Description and Characteristics

Inside a rectangular metallic enclosure of length l, width w and height h, only standing waves exist [23, 33]. An excitation signal injected within the cavity creates a well-known internal EM fields pattern for both the transverse magnetic (TM) and the transverse

electric (TE) modes. Each mode corresponds to a discrete frequency given mathematically in (2.13) [10, 23].

$$F_{mnp} = \frac{1}{2\sqrt{\mu\epsilon}}\sqrt{\left(\frac{m}{w}\right)^2 + \left(\frac{n}{h}\right)^2 + \left(\frac{p}{l}\right)^2} \tag{2.13}$$

where m, n and p $\in \mathbb{N}$

A passive reverberation chamber (RC) fits these descriptions. For a normal use, however, the internal fields are disturbed by means of a rotating paddle placed within the chamber. The fields change in time and in space for a finite number of stirrer configurations per revolution. The variation follows a χ^2 statistical distribution [1, 34, 35]. This creates a uniform E-field region contained in a space at $\lambda/4$ away from metallic structures such as the walls and the stirrer (Fig. 2.6) [1, 36]. The fields are also isotropic for an idealised and a well-stirred chamber according to the plane-wave integral approach by Hill in [34, 37, 38]. The isotropy assumption was validated experimentally by Ladbury *et al.* with a three axis E-field probe in [39]. For our RC purposes, this was verified using a log-periodic-dipole-array (LPDA) antenna and a standard radiator placed both at fixed locations within our chamber working volume. The radiator was oriented successively in three orthogonal directions. Similar power was measured per axis as will be summarised in 2.4.4.

2.4.2 Field Stirring

The stirrer is the most important part of an RC philosophy as the more efficient the stirrer, the better the field uniformity and the closer the chamber to Hill's idealised case. RC measurements are always evaluated over a set of stirring configuration per revolution. For mechanical paddles, the data are recorded at some specific stirrer angles θ. In mode-stirred technique, the stirrer rotates continuously and the field are sampled periodically every $\delta\theta$ defined by the user. Conversely, the stirrer is moved to a statistic angle position in mode-tuned operation. Both the mode-stirred and the mode-tuned measurements are performed over one stirrer revolution and are the only stirring techniques exploited in our measurements.

2.4.3 RC Calibration Overview

2.4.3.1 Chamber Loss

An RC must be calibrated for loss and for field uniformity before it is used. It must be recalibrated if a physical change is made internally [1]. According to the IEC 61000-4-21 [1], the RC standard followed in the dissertation, a calibration is a set of eight antenna-to-antenna measurements undertaken within the chamber working volume. Over this investigation, the first antenna is placed at a fixed location while the second is successively moved to eight positions represented by the notation A_1 to B_4 in figure. 2.6. These eight locations correspond to the chamber working volume corners. Two chamber losses are derived from the process which are:

- the antenna validation factor (AVF) and
- the chamber insertion loss (IL)

AVF is computed from the averaged power received per stirrer-revolution while IL is calculated from the maximum power reading.

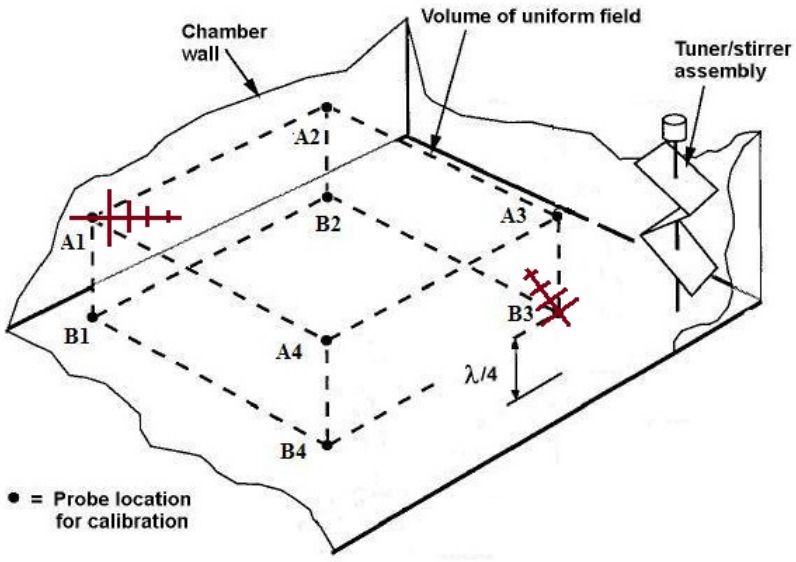

Figure 2.6: Antenna Locations for a RC calibration and the chamber working volume according to the IEC 61000-4-21 [1]

$$AVF = \left\langle \frac{P_{AvgRec}}{P_{In}} \right\rangle_{8\ Positions} \tag{2.14}$$

$$IL = \left\langle \frac{P_{MaxRec}}{P_{In}} \right\rangle_{8\ Positions} \tag{2.15}$$

In our previous work [40], we calibrated our RC using two identical LPDA antennas in mode-stirred operation. Three measurements have been performed for repeatability verification and to observe the chamber loss behaviour between mode-stirred and mode-tuned operations. Both the IL and the AVF are consistent as shown in figure 2.7. The similarity between the curves and the error bars indicates the calibration repeatability. However, AVF and IL behaviour at low-frequency prior to 400 MHz requires particular attention. In the next chapter, a new approach is presented based on an antenna efficiency investigation.

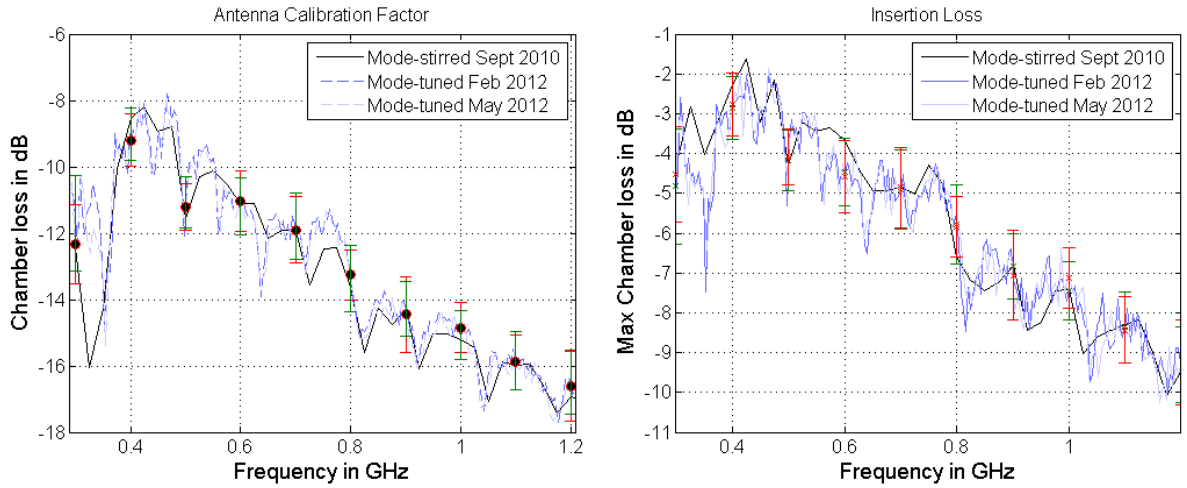

Figure 2.7: Our chamber AVF (left-hand side) and IL (right-hand side) measured with a mode-stirred and a mode-tuned operation.

2.4.3.2 Working Volume Field Uniformity

The calibration also permits the validation of the chamber's field uniformity, within the viable region, using the E-field standard deviation. The standard deviation (σ) of our chamber is shown in 2.8 to illustrate the principle. σ is calculated according to (2.16) and in figure 2.8, it is compared with the IEC uniformity requirement. The RC meets the IEC condition if the deviation is under 3 dB from 300 MHz and less than 4 dB for frequencies less than 200 MHz.

$$\sigma(dB) = 20 \cdot log_{10}\left(\frac{\sigma + E_{max}}{E_{max}}\right) \tag{2.16}$$

where σ is the linear standard deviation of the E-field and E_{max} is the maximum E-field in (2.17) calculated from the maximum received power per stirrer rotation P_{MaxRx} and the receiving antenna efficiency.

$$E_{max} = \left\langle \frac{8\pi}{\lambda} \sqrt{5 \frac{P_{MaxRx}}{\eta_{Rx}}} \right\rangle_{N\ probe-positions} \tag{2.17}$$

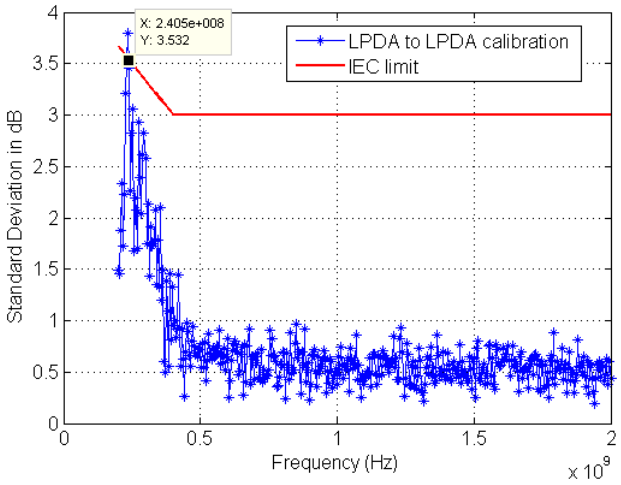

Figure 2.8: Comparison between the calibration standard deviation and the IEC field uniformity requirement. A LUF of 240 MHz is found at the curves' intersection and it is slightly above the theoretical value.

2.4.3.3 Lowest Usable Frequency

The lowest frequency limit of the RC bandwidth constitutes the RC lowest usable frequency (LUF). Theoretically, it is just above three times the chamber first resonance (which is equal to 220 MHz using (2.13). Practically, it corresponds to the value where σ exceeds the IEC limitation. For our chamber, an LUF of 240 MHz is found from the calibration standard deviation in figure 2.8. It is in agreement with the theoretical LUF calculation.

2.4.4 Antenna Significance for RC Applications

A three-axis E-field probe gives the best sampling of the field distribution per direction and is recommended for accurate chamber calibration [1]. For cost reasons, however, available antennas with the required bandwidth are often used. For an idealised RC, conforming to Hill's isotropy property [37], the antenna directivity is irrelevant. So, the same calibration result is expected with any antennas fitting the requisite bandwidth and a three-axis probe. In practice, the latter case implies a well-stirred chamber where each emission reaches the evaluation point in the working volume. However, it is important to note that the chamber isotropic property cannot be known unless measurements are performed. A non-uniform

field distribution can appear due to imperfections from the chamber geometry and the stirrer efficiency. In this context, the antenna radiation pattern begins to play a role and must be considered in the discussion. Aurand *et al.* investigated this issue in [41]. They highlighted the possibility of passing and failing to the IEC uniformity requirement with an omnidirectional and directional antennas such as a dipole and a slot-antenna. The behaviour is simply explained from the fact that an omnidirectional probe masks the chamber weakness due to its 360 degree sensitivity. Conversely, a narrow-beam-width antenna is suitable for signal characterisation in a particular direction and is recommended for accurate RC calibrations.

Two LPDAs were used to obtain the calibration curves shown in figure 2.7 and which are widely known as directional antennas. According the work of Aurand et al *et al.* in [41], we can then argue that the standard deviation presented in figure 2.8 is an acceptable calibration result. As far as the isotropic property is concerned, in [40], we verified the assumption using the setup shown in figure 2.9. An LPDA was placed inside the chamber working area for a radiated-power measurement. A standard radiator, also located within the same volume, was successively oriented in three orthonormal directions for RC excitations.

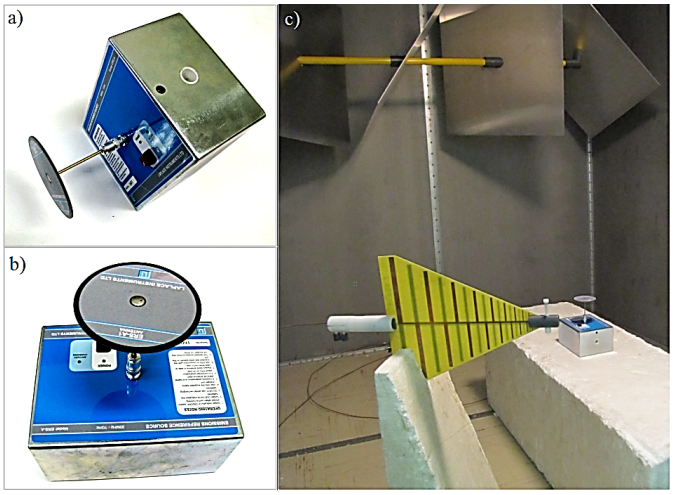

Figure 2.9: Setup for RC isotropic property verification using a standard radiator and an LPDA antenna [40]. (a) shows an horizontally polarised radiator. (b) corresponds to the vertical polarisation. (c) gives an overview ot the RC setup showing the receiving LPDA and the standard radiator above a polystyrene foam.

Similar radiated-powers were measured per standard radiator orientation as shown in figure 2.10.a. The result do not fully qualify the chamber as conforming to Hill's idealised case but, the figure shows that the imperfections are small.

As a consequence of these discussions, the chamber imperfections and the LPDA radiation pattern play a minor role on the chamber attenuation curve behaviour in figure 2.8. The

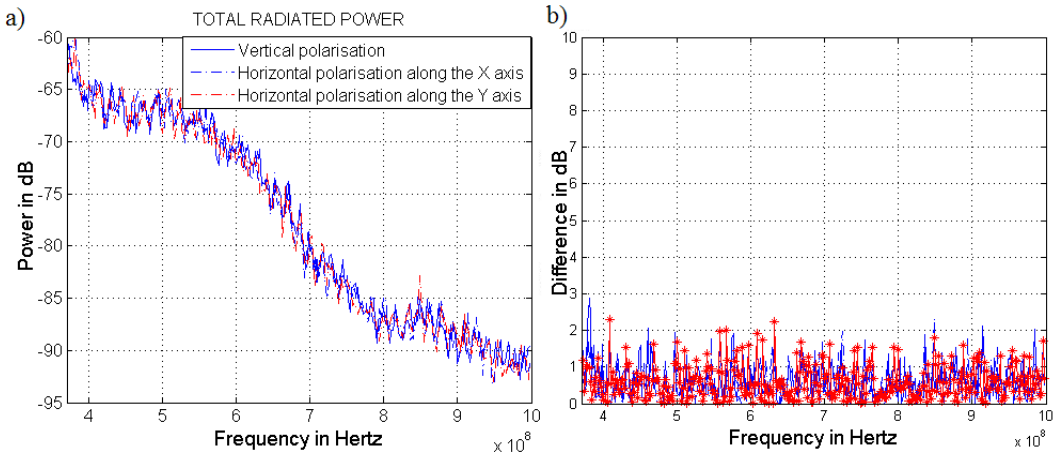

Figure 2.10: Standard radiator total radiated powers comparison for isotropy verification. At the right-hand side of the figure is shown the normalised power variation

IEC recommendation of 0.75 was used for the calibration data processing. This can be considered as a potential source of error in case these antennas are not 0.75 efficient across the frequency band. In the next chapter, an efficiency investigation is presented in an attempt to scrutinize the low-frequency behaviour of AVF and IL curves in figure 2.7.

2.5 SE Definition Interpretation

2.5.1 SE Investigations in Literature

Two measurements are necessary for the evaluation of the SE definition in (2.1). For the first case, the shield is present. The transmission between a source, illuminating the shielding under-test (SUT), and a probe within the protected region is measured. The shield is removed from the setup for the second scenario, and the transmission is re-measured at the same probe location. Literature survey concerning shielded-enclosures (cabling and rectangular boxes) shows a variety of SE measurement principles. Some studies follow the definition in (2.1). For others, the measurement is undertaken differently. For example, in [42] and [43], the unshielded and the shielded procedures are followed. In [42], Wang *et al.* characterised the SE of an RG-58 external conductor. They measured the cable output with and without the braiding for the SE estimation. Similarly, in [43], Herlemann *et al.* determined the SE of a metallic box using two measurement scenarios: the presence and the absence of their enclosure under-test (EUT) inside a GTEM (Gigahertz Transverse Electromagnetic) cell. The EUT is always present inside the working volume for RC-based configuration as found in [44, 45, 46, 47, 48]. SE is determined from the power outside and inside the EUT and it conforms to the IEEE standard methodology

for small enclosures SE in [2]. For some situations, the unshielded configuration is not applicable, the shield has to be present due to measurement constraints. The Karoo Array Telescope (MeerKAT) pedestal SE investigation in [49] is an example of the latter case. Van der Merwe used the pedestal external and internal currents for his study due to the telescope fixture and size.

2.5.2 SE for Reverberated Environment

For RCs, the EUT must be placed within the chamber working volume for SE characterisation. It is exposed to the signal injected within the facility. Thereafter, the EUT internal and external powers (P_{EUT} and P_{Ext}) are estimated from measurements in the presence of the enclosure in the chamber. SE is expressed as follows according to the IEEE standard [2]:

$$SE_{IEEE} = \left| 10\, log \left(\frac{P_{EUT}}{P_{Ext}} \right) \right| \tag{2.18}$$

The EUT external probe location is irrelevant to the SE investigation as a direct consequence of the RCs field isotropy and uniformity.

2.6 Shielding Technique: Practical Approach

2.6.1 The Nested-Enclosure Technique

The RC SE measurement procedure described in [2] is also known as the nested-enclosure technique. It has been used for shielded-box SE characterisations in [50, 51]. The EUT is also stirred for standing wave reason. Both the RC and the EUT stirrers are synchronised for proper EUT transmitted field measurement. For our case in particular, the RC stirrer (ST1) and the enclosure stirrer (ST2) are configured in mode-stirred and mode-tuned operations, respectively. ST1 is moved to the next static position after ST2 completes a full rotation. The EUT internal fields are sampled at specific angles of ST1 and ST2. Due to the synchronisation procedure in general, the nested-enclosure methodology produces more data than the usual RC application (such as a radiation investigation). As a result, the nested-enclosure measurement takes longer. For a frequency-domain (FD) technique, the measurement delay T_m is approximately given by (2.19) for X number of frequencies.

$$T_m = M.N.T_s.X \tag{2.19}$$

where T_s is the receiving instrument sampling time interval. M and N are the number of positions for the internal and the external stirrers.

A faster T_m is one of the objectives of the dissertation. Two solutions are proposed to meet this goal:

- The first is the use of a time-domain (TD) technique for measurement. In this regard, the frequency signal spectrum is simultaneously injected within the system and allows a measurement-time speed-up. X becomes irrelevant and T_m reduces to a constant value ($T_m = MNT_s$).
- ST2 is removed from the setup for the second solution. The same measurement-time as the usual RC application is achieved for both FD and TD.

2.6.2 Time-Domain Methodology for Time Speed-Up

In 1988, Hatfield used an amplified broadband noise signal from 2 to 4 GHz, generated by a solid-state avalanche noise diode, to test the TD nested-enclosure approach. He found agreement between FD and TD and a faster measurement-time. The TD methodology also showed fine extra-features not visible in the FD measurement. In [52, 53], two conference papers we published about the TD and FD similarities, we also reached the same conclusion as Hatfield.

Broadly, a TD methodology needs a sensitive receiver and a special generator for the nested-enclosure measurement. A step recovery diode (SRD) and an avalanche transistor pulse generator have been built for our TD SE investigation. The design is based on the schematic in [54]. As far as the receiver is concerned, our RC TD signals are recorded with the SKA receiver RATTY (Real Time Transient analYser) [55]. Our TD chain characterises the SE at low-frequencies from 200 MHz to 1.4 GHZ while Hatfield's approach is for higher frequencies between 2 and 4 GHz. Details on the pulse generator are given in appendix A.

2.6.3 Field-Cutting-Loop Feeding for Stirrer Cancellation

The smaller the enclosure, more cumbersome the paddle size becomes. Holloway et al. commented on this issue in [56]. They proposed a frequency-stirring technique to replace the EUT paddling system. No physical device is inserted within the EUT to solve the fitting problem. But in terms of the delay T_m, no major change would be seen because synchronisation is still necessary between ST1 and the new stirring technique. In the

dissertation, we propose a field cutting-loop feeding to solve the stirrer-size problem and to achieve a faster measurement delay.

A field-cutting-loop feed is a loop antenna placed inside the EUT, soldered on the enclosure wall, and connected to an external SMA connector for measurement. For a reverberated enclosure, the power inside the EUT is estimated from the maximum transmitted field for a worst case SE consideration. We believe that with the loop feeding measurement it is possible to evaluate the maximum field transmitted within the EUT without using a stirrer. A correction factor is applied to the measured data, it is derived from cavity resonator equations in [23]. In chapter 5, simulations and experimental studies are presented to confirm the loop configuration principle.

ST2 is not efficient unless 60 modes are present within the EUT according to RC principle [1]. The nested-enclosure SE result is valid for a frequency range exceeding the EUT LUF as a consequence of this RC characteristic. As for as our TD measurement is concerned, the higher the LUF, the more our TD methodology characterises the EUT in the non-viable condition. In this regard, the loop feeding forms also a promising configuration for a better SE investigation in low-frequencies before the LUF.

2.6.4 TD Methodology Validation Strategy

Before the nested-enclosure measurements are undertaken, the TD methodology is evaluated with a device that we calibrated. A 50 Ω coaxial airline is built for this reason and the SE of the cable cylindrical shield is investigated. The airline Z_t is analytically modelled, simulated with computational electromagnetic (CEM) codes and measured within the RC in TD and FD. The similarity between the obtained Z_ts is the key for the validation. It is also important to notice that FD measurements are always taken as a reference in the dissertation due to the well-established precisions of vector network analysers (VNAs).

2.7 Summary

SE and Z_t have been reviewed in the chapter. An overview on RCs were addressed to show the significance of the antenna efficiency on RC measurement. The application of the SE definition on practices has been inspected. The unshielded condition of the SE analytical definition is shown as the main physical difference between SE measurement approaches we found in peer-reviewed publications. We studied analytically an infinite static shield case

to account for an incident field measurement in the presence of a SUT. The unshielded configuration condition has been the focus of the RC technique. The IEEE-definition for SE estimation was examined for a deeper understanding of the nested-enclosure technique. A TD measurement investigation is proposed for faster SE measurement-time. A field-cutting-loop enclosure feeding is also introduced for physically small enclosure SE determination and to account for EUT SE in an under-moded condition.

CHAPTER 3

Reverberation Chamber Antenna Efficiency for Improved Low Frequency Performance

The non-weather dependent nature of an RC technique is an obvious advantage that makes the device an essential tool for pre-compliance testing and for low-cost methodology. A great interest has been shown in the RC field distribution and the stirrer efficiency for accurate RC applications [38, 57, 58, 59]. However, because of the tightly-coupled nature of RCs, more attention should be given to basic properties such as the antenna efficiency.

LPDA antennas are widely used in RCs for data recording. Many non-commercial LPDA designs are available and have been used by engineers for reasons of low-cost and for personal requirements. The antenna we use for our RC applications is shown in figure 3.1. It works for a frequency band of around 430 MHz to 6 GHz and it is built with an FR-4 printed circuit board (PCB) medium. Without any reference to LPDA material properties, the IEC standard 61000-4-21 (for RC) recommends an LPDA efficiency of 0.75 for an unknown LPDA characteristic. In this chapter, an antenna efficiency study is presented for accurate low-frequency response of our RC. The efficiency of our PCB-LPDA is investigated using an RC measurement approach similar to that presented in [60, 61]. Our reference antenna efficiency is determined directly from a CEM code which is then validated using a simulated Wheeler-cap methodology. The cable feed is included in the modelling of the dipole to explicitly account for the unbalanced reference antenna. Our RC

is thereafter recalibrated. The chamber loss factor is calculated using both the standardised 0.75 and the measured value to show the significance of the incorrect efficiency on RC applications. In the last section of the chapter, the impact of the efficiency study on a real RC application is checked.

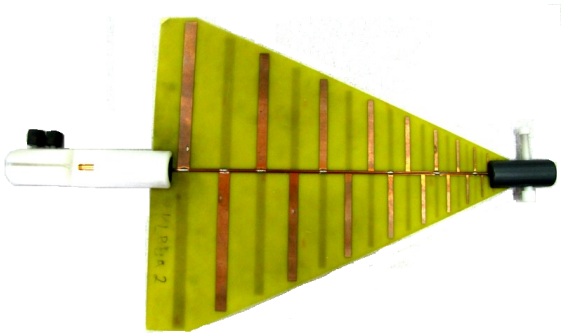

Figure 3.1: The PCB-based LPDA antenna designed for our RC application

3.1 Antenna Efficiency Definition

The radiation efficiency (η_r) of an antenna relates the power injected within the device (P_{In}), corrected from a port mismatch, to the power transferred in the environment (P_{Rad}) [62]. It is expressed analytically in (3.1), where P_{Loss} represents the antenna power dissipation.

$$\eta_r = \frac{P_{Rad}}{P_{In}} = \frac{P_{Rad}}{P_{Rad} + P_{Loss}} \tag{3.1}$$

3.2 Antenna Efficiency Significance for RCs

3.2.1 RC Measurement Modelling

An RC measurement can be visualised in the sketch presented in Fig. 3.2. Port impedance mismatch and antenna efficiency are incorporated in the following expression:

$$P_{Out} = P_{In}\,(1- < |S_{11}|^2 >_n)(1- < |S_{22}|^2 >_n)\mathrm{AVF}\;\eta_{Rx}\;\eta_{Tx} \tag{3.2}$$

where:

- P_{Out} is the averaged power per stirrer-revolution in Port2

- P_{In} is the power delivered by Port1
- AVF is the chamber antenna validation factor [1]
- η_{Rx} and η_{Tx} are the antenna radiation efficiencies
- $< |S_{ij}|^2 >_n$ represents the average of the square of the magnitude of S_{ij} over the number of stirrer positions n. Throughout the dissertation, 72 stirrer positions are used for measurements (n = 72).

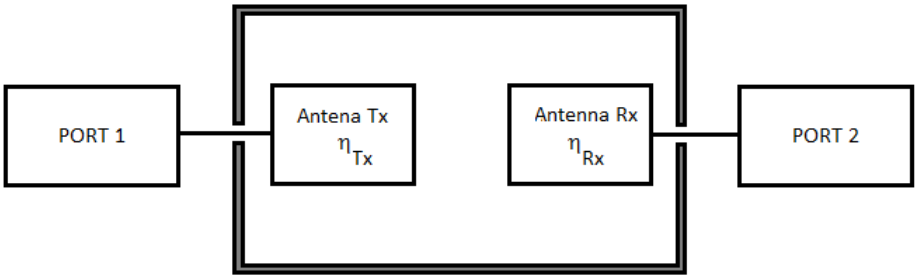

Figure 3.2: RC simplified measurement diagram for each stirrer position.

The RC attenuation characteristic (AVF) is determined from the IEC calibration procedures [1] described in section 2.4.3. The calibration investigation produces eight S-parameter sets, which give the expression in (3.3) by substituting (2.14) in (3.2).

$$\text{AVF} = \left\langle \frac{< |S_{21}|.^2 >_n}{(1- < |S_{11}|.^2 >_n)(1- < |S_{22}|.^2 >_n)\eta_{Rx}\,\eta_{Tx}} \right\rangle_k \tag{3.3}$$

where k = 8. It represents the number of antenna positions used for the investigation.

Remark

It is important to note that the S-parameter data collected over one stirrer rotation correspond to different RC configurations. Thus, the averaged S-parameter per stirrer-revolution is always calculated from the S-parameters magnitudes.

Similar to AVF, the variable called chamber validation factor (CVF) also represents an RC attenuation factor. AVF represents the loss of an empty RC while CVF corresponds to the chamber attenuation when it is loaded. CVF is investigated in the presence of the device-under-test in the RC working volume and it is calculated using the same expression in (2.14). For simplicity reason, we use AVF throughout the chapter but the comments that we will address are also valid for CVF.

3.2.2 Effect of Incorrect Antenna Efficiency

In (3.3), the efficiencies η_{Rx} and η_{Tx} compensate for the antenna effects. The reflection coefficients correct for the port mismatches. If either η_{Rx} or η_{Tx} are incorrect, AVF is inaccurate. The AVF variation in dB is presented in Table 3.1 for few arbitrary LPDA efficiencies. The IEC recommendation of 0.75 is taken as a reference, and the two LPDAs, T_x and R_x, are assumed to be identical in the calculation. ΔAVF is computed as follows:

$$\Delta\text{AVF}(dB) = |AVF_{\eta}(dB) - AVF_{0.75}(dB)| \tag{3.4}$$

which simplifies to

$$\Delta\text{AVF}(dB) = \left|10\,log(\eta^2) - 10\,log(0.75^2)\right| \tag{3.5a}$$

$$= |20\,log(\eta) - 2.4988| \tag{3.5b}$$

Table 3.1: AVF variation for antenna efficiencies where η is not 0.75

Efficiency	0.1	0.3	0.5	0.7	0.9	1
ΔAVF(dB)	17.5	7.96	3.52	0.6	1.58	2.5

The finding from the test is simply that when the actual antenna efficiency is going to be outside of a range yielding an acceptable AVF error, then a procedure to determine the accurate value is necessary.

3.2.3 Discussion on Antenna Efficiency Variation

Two sources are identified as the potential causes for the LPDA efficiency variation in our measurement. The first reason is attributed to the chamber loading effect on the antenna while the second is related to the LPDA working-bandwidth.

P_{Rad} changes with the environment according to (3.1). So, the chamber is expected to load the LPDA at low-frequencies due to the chamber boundary conditions. This can be checked from the LPDA S_{11} curves in free-space and outside the RC shown in figure 3.3. Here, the white and the black curves represent respectively the antenna S_{11} inside and outside the chamber. 72 RC stirrer positions are considered for the S_{11} averaged response. It can be seen from figure 3.3 that the LPDA works well from 430 MHz in a

free-space environment if -10 dB is taken as the reference. This operational point is shifted to a frequency higher than 650 MHz (from to the white-curve) once the LPDA is moved into the RC. This shift in frequency indicates a change of the antenna P_{Rad} and thus in efficiency for low-frequency signals.

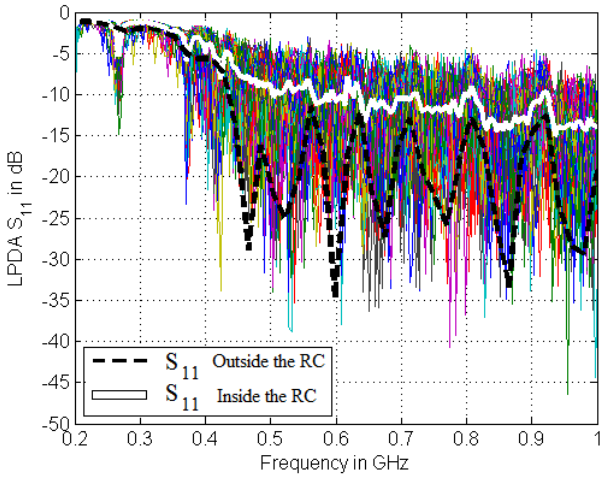

Figure 3.3: Comparison of the LPDA S_{11} inside and outside the RC. The white-curve represents the averaged S_{11} over a stirrer-revolution whereas the LPDA S_{11} per stirrer-position is shown by the background curves. The black plot represents the LPDA S_{11} outside the RC.

The antenna cannot be regarded as efficient lower than 430 MHz because it is below its working bandwidth. A broader bandwidth LPDA antenna covering the region down to 200 MHz is obviously better for the RC measurement. However, such an antenna is bigger and this will increase the direct-coupling path between antenna and EUT within the RC. It will also influence the working volume. The LPDA shown in figure 3.1 is small enough for reasonable data sampling and at a distance which does not emphasize direct coupling. Furthermore, we wish to maximise the working range of the RC and the LPDA can be operated down to lower frequencies than the -10 dB cut-in. The antenna efficiency characterisation is then crucial to de-embed the LPDA effect within the data. The research will then demonstrate the viability of this approach.

3.3 Methodology and Measurement Description

Our efficiency methodology is similar to the approach presented in [61, 63], where an RC and a well-known antenna are used. In our case, a FEKO simulation of a small dipole in free-space provides the reference efficiency that we wish to trust. Also, the measurement is undertaken at the eight positions (k = 8) of the IEC calibration, in figure 2.6, for an accurate efficiency estimation.

Briefly, two measurement setups (S1 and S2) are used, where the radiation from a third antenna placed within the RC working-volume is measured. The data are recorded through the reference dipole for S1 while the unknown LPDA antenna is utilised for S2. The S-parameter sets obtained form both scenarios yield the expressions in (3.6) using (3.2) for each k position.

$$S_{21\,S1} = (1- < |S_{11}|^2 >_{n\,(S1)})(1- < |S_{22}|^2 >_{n\,(S1)})\ \text{AVF}\ \eta_{Ref}\ \eta_s \tag{3.6a}$$

$$S_{21\,S2} = (1- < |S_{11}|^2 >_{n\,(S2)})(1- < |S_{22}|^2 >_{n\,(S2)})\ \text{AVF}\ \eta_{LPDA}\ \eta_s \tag{3.6b}$$

where η_s is the third antenna efficiency and η_{ref} is the simulated dipole efficiency.

Both S_{11} terms are identical for S1 and S2 and by eliminating AVF in (3.6) equations, we derive the LPDA efficiency as follows:

$$\eta_{LPDA_k} = \eta_{Ref} \frac{< |S_{21}|^2 >_{n\,(S2)}}{< |S_{21}|^2 >_{n\,(S1)}} \left(\frac{1- < |S_{11}|^2 >_{n\,(S1)}}{1- < |S_{11}|^2 >_{n\,(S2)}} \right) \tag{3.7}$$

3.4 Computational Electromagnetic Modelling

3.4.1 Reference Dipole Antenna FEKO model

The physical reference dipole is built from a brass-rod of 10 cm long and 1 mm radius. It is modelled in FEKO using a wire and a wire-port as depicted in figure 3.5.a. The reference efficiency is computed from 200 MHz to 4 GHz. The result is validated through a simulated Wheeler-Cap technique as will be discussed in section 3.5.

We decided on a small dipole for the task because the smaller the antenna, the weaker the RC loading effect. This then provides a more consistent efficiency between free-space and the chamber environment. To demonstrate this, the dipole reflection inside and outside our RC has been measured. The two measurement results are shown in figure 3.4 along with the free-space simulated S_{11}. Here, the simulation represents the perfect free-space environment without feed-cable complication and without nearby reflector objects, such as the surrounding buildings or the appliances within our laboratory. As clearly seen on the figure, the difference between the measured reflections is insignificant. The measurement outside the RC also matches the free-space simulation in terms of pattern trend and resonance frequencies.

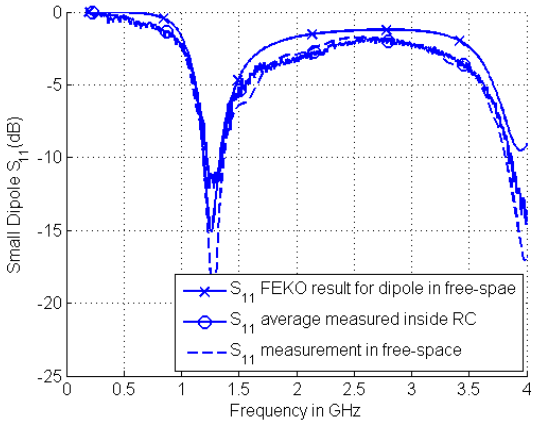

Figure 3.4: Comparison between the reference dipole measured S_{11} in free-space and in the chamber, along with the simulated S_{11}.

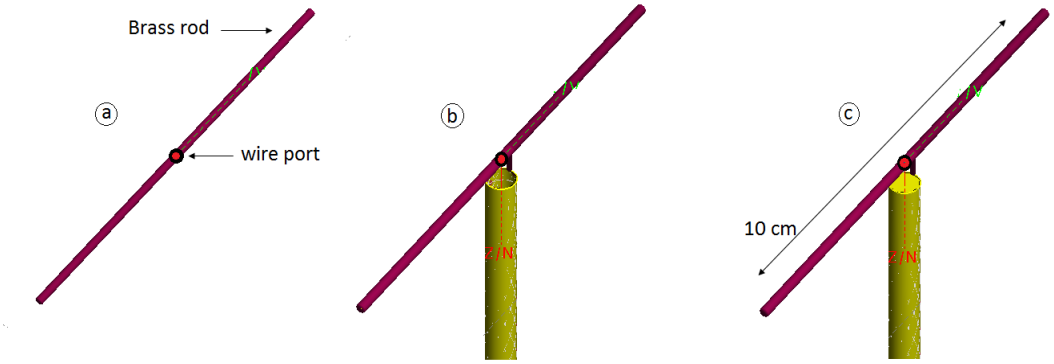

Figure 3.5: The FEKO models we used for the reference dipole characterisation. (a) shows the dipole model, in free-space, made of 10 cm brass rod. (b) and (c) account for the cabling effect on the simulated efficiency.

3.4.2 Feed-Cable Effect on the Dipole

The dipole is connected to a vector network analyser (VNA) through a semi-rigid cable for the real setup. The unbalanced nature of the connection cable-antenna makes the cable shield a part of the dipole action. We chose not to use a balun to avoid frequency limitations. So, we were also concerned about the effect of a feed cabling on the dipole efficiency.

The FEKO models shown in figure 3.5.b and figure 3.5.c account for the cabling connection. A full cylinder and a hollow pipe are considered to determine the proper cable external conductor representation. The VNA is calibrated at the cable connector for the measurement. So, the dipole feeding is positioned just outside the cable geometry to replicate the VNA calibration plane. The computational outcomes are shown in figure 3.6.a, where the crossed and the circled curves represent the dipole efficiencies with the cylindrical pipe and the full cylinder. Both geometries constitute a good cabling model since similar

efficiency is seen over the frequency range.

An equivalent 10 cm and 20 cm cable lengths are also simulated with the results shown in figure 3.6.b. The dashed curve represents the dipole efficiency without a feed cable; the curves with crosses and squares present the differences due to the 10 cm and 20 cm feeds, respectively. As can be seen, the highest variation happens in the lower-frequency region. The cable plays a minor role at frequencies beyond 1 GHz. A maximum difference of 0.018 is observed at 200 MHz. Figure 3.6.b also shows that the longer the cable, the more efficient the overall dipole arrangement at low-frequency. With a highest theoretical efficiency of one, the largest drop at 200 MHz is 0.035. From the earlier findings, the cabling effect on the dipole efficiency can be ignored.

3.4.3 LPDA CST-Studio modelling

A CST simulation of the LPDA is undertaken for comparison with our final measured LPDA efficiency. Some important modelling detail is highlighted in figure 3.7.a and figure 3.7.b. The PCB FR-4 material is included, structure meshing was refined and the excitation is provided by the discrete port connected to the LPDA centre conductor as shown. The findings are discussed in section 3.6.

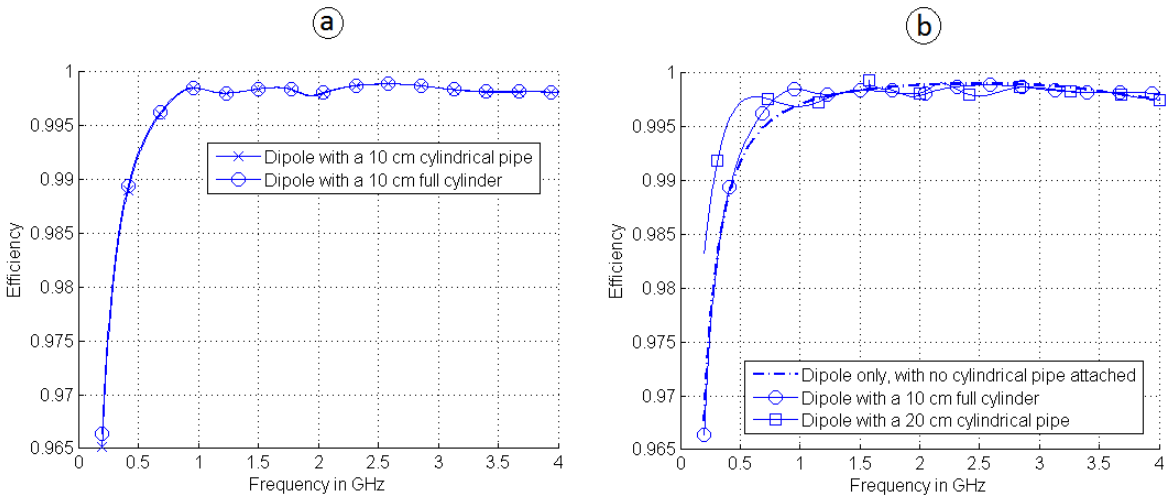

Figure 3.6: Identification of the proper model for the cable shield. At the left-hand side (a), the efficiency for a 10 cm pipe and a 10 cm cylinder are plotted. At the right-hand side, in b, are shown the efficiency variation due to cable lengths of 10 cm and 20 cm.

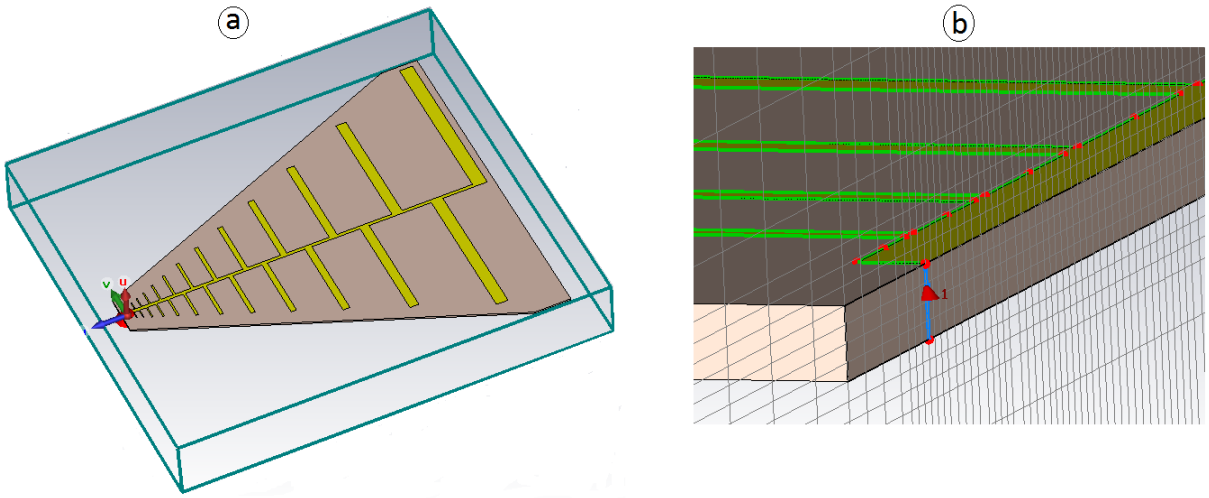

Figure 3.7: The LPDA CST model showing the antenna parts and the FR-4 PCB medium (in a). In b, the model meshing and excitation are presented.

3.5 Dipole Modelling Validation

3.5.1 The Wheeler-cap Method Overview

The Wheeler-cap method is a well-known technique for a short antenna efficiency characterisation. The antenna under-test (AUT) is enclosed inside a radian-sphere cap for the study. The setup configuration cancels the radiation for an estimation of the power lost within the antenna material as heat. Briefly, a radian-sphere is a boundary between the near-field and the far-field region of short antennas and the cap radius varies proportionally with the signal wavelength, called the radian-length [64]. A static cap of constant size (spherical and non-spherical) also works for the study as mentioned in [65] and as we will demonstrate further in the text. The AUT input impedance in free-space (Z_{fs}) and inside the cap (Z_{wc}) are both used for the Wheeler-cap efficiency calculation, as follows [66]:

$$\eta = \frac{re(Z_{In\,fs}) - re(Z_{In\,wc})}{re(Z_{In\,fs})} \tag{3.8}$$

3.5.2 Dipole Simulation Validation

Dipole Only Configuration

The Wheeler-cap models shown in figure 3.8 are used for the dipole efficiency validation. The dipole is placed inside each enclosure, made of a perfect electric conductor (PEC)

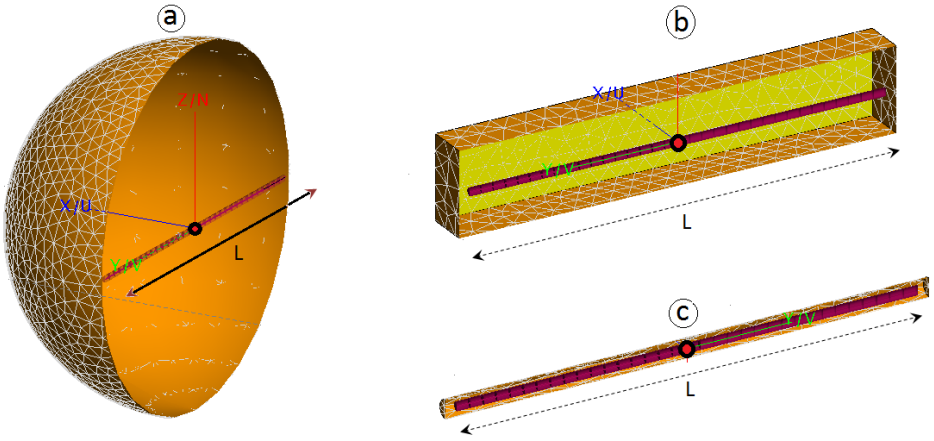

Figure 3.8: The Wheeler-cap configurations used for the dipole efficiency validation. The sphere diameter, the rectangular and the cylinder lengths are equal and both made of a PEC material.

material to prevent an extra power dissipation, without touching the cap. Each structure input impedance is calculated from the simulation S_{11} with the computed efficiency shown in figure 3.9. Spikes are noticed on the Wheeler-cap results due to cap resonances. Despite that, a common trend is noticeable between the curves; and it agrees well with the dipole efficiency simulation in free-space depicted by the dashed-curve.

A short dipole of length l input impedance is equal to the sum of the dipole skin resistance (R_s) and the radiation resistance (R_{rad}) according to [23, p. 564, 567]. R_s is given in (2.7) while R_{rad} is expressed in (3.9) from the same literature

$$R_{rad} = \frac{2\pi}{12}\eta_0 \left(\frac{l}{\lambda}\right)^2 \tag{3.9}$$

The theoretical efficiency of the dipole is also plotted in figure 3.9. Firstly, a relatively similar curve tendency is seen between the FEKO simulations and the analytical result. Secondly, a maximum difference of 0.05 is observed at the lowest frequency value while the agreement is very good at higher frequencies. Three meshing parameters were used for the simulation, which are: the standard ($\lambda/12$), the fine ($\lambda/25$) and an adaptive meshing. But, the same result is obtained for both cases. This indicates that the low-frequency difference comes probably from theoretical simplification assumptions.

Dipole with Feed Cable Configuration

In a second set of simulations, a cylindrical cap is used to validate the efficiencies for the 10 cm and 20 cm dipole-cable models in figure 3.5.b and figure 3.5.c. The cap follows the antenna geometry, in a T-shape fashion (see figure 3.10), to shift the cap resonances at

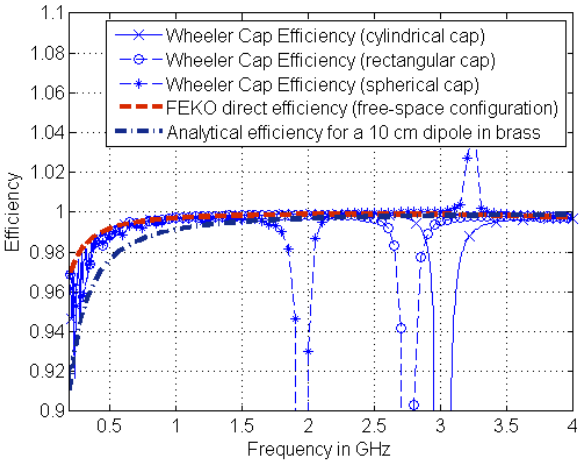

Figure 3.9: Dipole efficiencies comparison between free-space and the three Wheeler-cap configurations.

higher frequencies. A common pattern is also visible between the Wheeler-cap simulation and the FEKO direct efficiency without accounting for the curve resonances in figure 3.11.

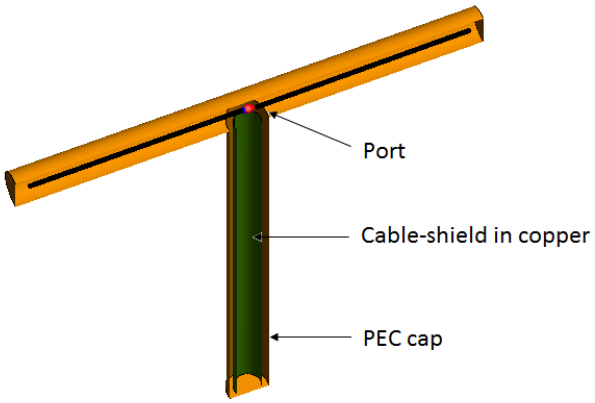

Figure 3.10: Wheeler-cap model for the feed-cable effect validation. The dipole and the cable geometry are both enclosed in a PEC cylindrical cap forming a T-shape.

So far, the agreement between the Wheeler-cap simulations, the analytical model and the FEKO direct efficiency result partially confirms the efficiency validity. A physical Wheeler-cap measurement is preferred for a complete validation. However, it is not undertaken due to constraints related to the cap realisation. Moreover, a correct LPDA efficiency outcome also confirms the dipole efficiency.

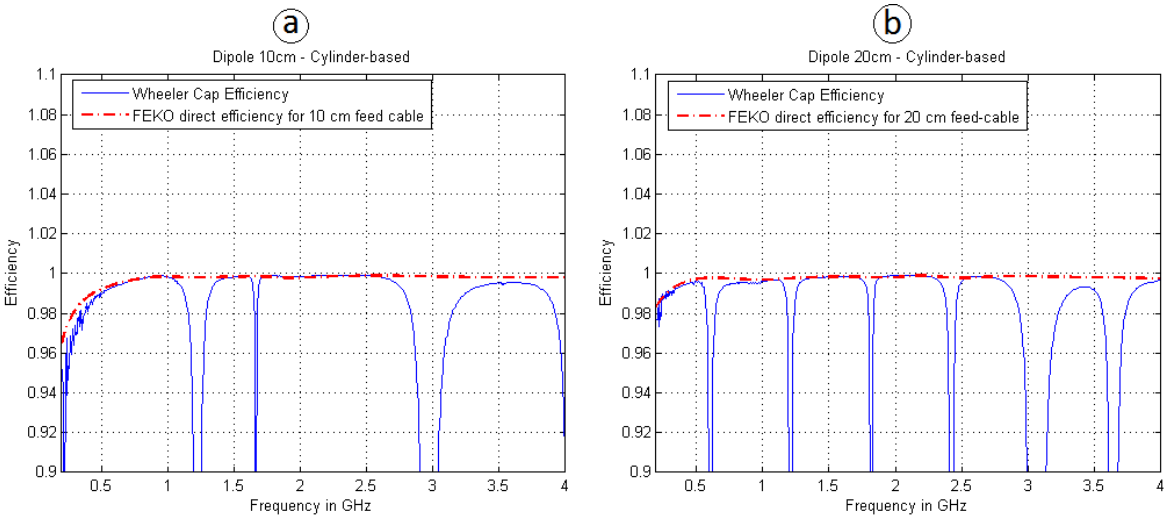

Figure 3.11: Dipole with feed cable efficiency validation using a Wheeler-cap configuration. In a and b are shown, respectively, the Wheeler-cap efficiency result for the 10 cm and the 20 cm cable geometry.

3.6 LPDA Efficiency Result and Discussion

The Wheeler-cap method was not utilised for the LPDA efficiency measurement because a special, bigger enclosure is then necessary. We consider this to be impractical and also find that the lower frequency cap resonances interfere with the investigation. An RC is available to us and it has been shown as a good alternative methodology for antenna efficiency characterisation in [60, 63, 67].

The measured and CST-simulated efficiences are plotted in Fig. 3.12, along with the IEC default value of 0.75. The background traces are the actual measured efficiencies at the eight positions shown in figure 2.6. It should be noted that the measurement recorded 801 frequency points while only 41 are used for the LPDA modelling.

Figure 3.12 shows that the LPDA efficiency is not constant over the band. Here, three regions are identifiable:

- the LPDA measured efficiency is low from 200 MHz to 400 MHz
- it is varying around 0.75 between 400 MHz to 1 GHz
- it settles to approximately 0.55 for frequencies higher than 1 GHz

With reference to Table 3.1, significant errors can then be expected for our chamber AVF particularly in the lower band of operation if the IEC recommendation of 0.75 is used.

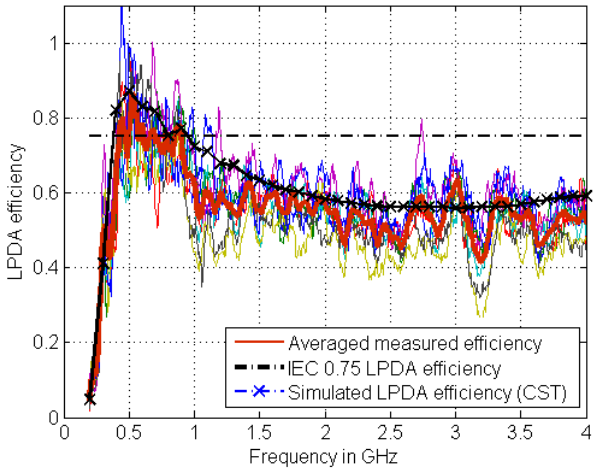

Figure 3.12: Comparison between the simulated, RC average measured LPDA and IEC-default efficiencies. The background curves are the measured efficiencies at the eight RC positions to illustrate the measured range.

3.7 Impact of the Study on RC Calibration

The RC was recalibrated using the reference dipole and the characterised LPDA antenna. The dipole was placed at a fixed position within the RC working volume while the LPDA was moved to the eight locations. The short dipole and the measured LPDA efficiencies are now used in (3.3) for the characterisation of the chamber attenuation. This yields a revised chamber AVF, shown in figure 3.13 where the crossed-curve on the plot depicts an LPDA-to-LPDA calibration result, using the IEC proposed efficiency of 0.75.

The difference between the two curves is small between 400 MHz and 1 GHz for efficiency values approaching 0.75. The major effects are at low-frequencies due to the significant LPDA efficiency difference below 400 MHz as seen in figure 3.12. The corrected LPDA efficiency gives an RC-measured AVF of 0 dB at 240 MHz which coincides with the chamber LUF shown in figure 2.8. A more expected monotonically-decreasing AVF with frequency is now also apparent. Analytically, the power dissipated in the chamber is the sum of the power absorbed by the walls, the stirrer and the power escaping outside the RC through aperture leakage [68]. The wall contribution is proportional to the square root of the frequency [23] and the aperture leakage is proportional to the signal frequency [68]. The nearly-linear decrease now seen for AVF variation on the log-log scale is therefore expected over the range.

In summary, a fraction of the power consumed within the LPDA is intentionally assigned to the chamber by using an incorrect efficiency value. The newly acquired LPDA efficiency corrected for this issue. Yet, the impact of the finding on a real RC application, such as a

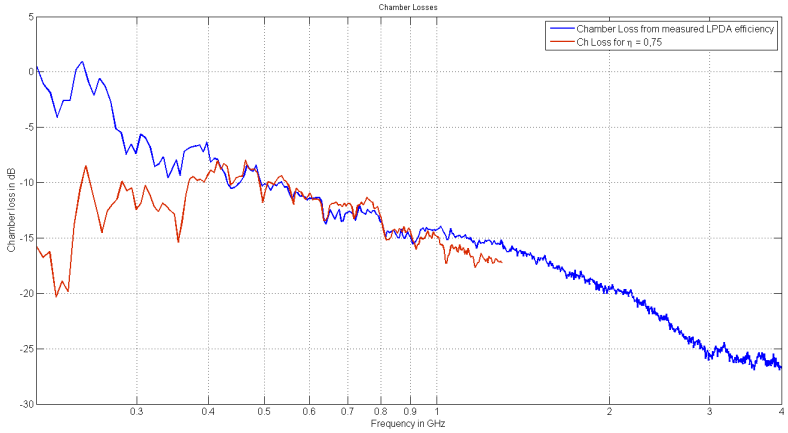

Figure 3.13: Revised chamber AVF showing low-frequency changes with our measured LPDA efficiency. The corrected value will allow better measurements from 200 to 400 MHz which is considered a useful extension to any RC operational range.

radiation or an immunity investigations, remains a part of the discussion.

3.8 Impact of the Study on Radiated Power Investigation

For both the radiation and the immunity measurements, a unique instrument (the device under-test (DUT)) replaces the transmit chain (the T_x antenna and Port1) shown in figure 3.2. Equation (3.2) reduces to the following:

$$P_{DUT} = P_{In}\,(1 - < |S_{11}|^2 >)\text{AVF}\,\eta_{Rx} \tag{3.10}$$

Here, only the half of the variation seen in ΔAVF is expected due to the presence of only one antenna within the setup.

In the next section, the impact of the newly acquired LPDA efficiency and the chamber AVF on a real RC application is determined. A certified standard radiator and a well-characterised built-in reference coaxial cable are used for the investigation.

3.8.1 Standard Radiator Examination

The standard radiator used for the experiment is placed within the chamber working volume over the measurement. The radiation is recorded on a spectrum analyser (SA) through the characterised LPDA antenna. 72 samples are taken per stirrer revolution.

The stirrer was configured in mode-tuned operation for a proper scan of the measurement frequency range (from 200 MHz to 1 GHz). Afterwards, the E-field in an open area test site (OATS) is estimated from the data, using (3.11) [p. 64][1]. Lastly, the calculation outcome is compared with the manufacturer calibration data for evaluation.

$$E_{OATS} = gmax\sqrt{\frac{D\ P_{RC}\ 377}{4\pi\ R^2}} \tag{3.11}$$

where D is the DUT maximum directivity, R is the distance between the DUT and the receive antenna and P_{RC} represents the RC measurement.

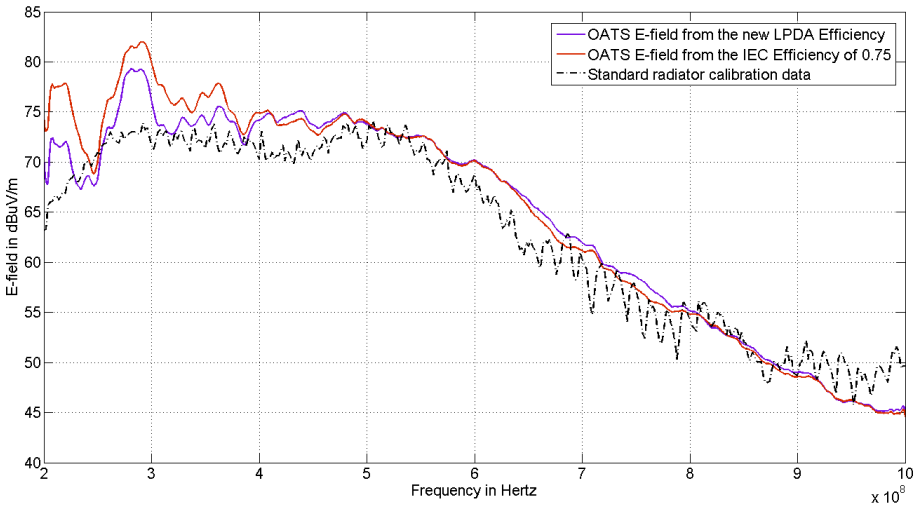

Figure 3.14: OATS E-field measurement of a standard radiator placed within the RC. Both the IEC default efficiency and the newly measured LPDA efficiency are used in the computation.

The results of the investigation are shown on figure 3.14. The red curve depicts the OATS E-field calculation using the new LPDA efficiency and the corrected AVF. The blue plot represents the E-field computation from the IEC default efficiency value and the previous AVF. The figure shows a general pattern agreement between the measurement and the calibration data. Both measurements give a similar E-field trend from 400 MHz while higher differences are noticed between 200 MHz and 400 MHz. It is also visible within this low-frequency region that the correct LPDA efficiency value yields a curve (the one in blue) closer to the radiator calibration data. The difference between the red curve and the blue curve can be explained from the inclusion of the transmit antenna effect in the old AVF parameter but which is no longer part of the setup. This indicates once again the importance of the LPDA efficiency characterisation for RCs.

3.8.2 Reference Coaxial Airline Examination

Having made the correction for the LPDA efficiency, it is natural to ask about the features below 500 MHz in figure 3.14 that are not fully aligned with the calibration data. To examine this more carefully, a reference coaxial airline is introduced.

The coaxial airline is shown on figure 3.15. The cable is also placed within the RC working volume for the measurement, and the data are recorded in mode-tuned fashion with 72 positions per revolution. The Z_T corresponding to the characterised efficiency value and the IEC value are shown in figure 3.16 with the cable theoretical model according to Kley (2.9).

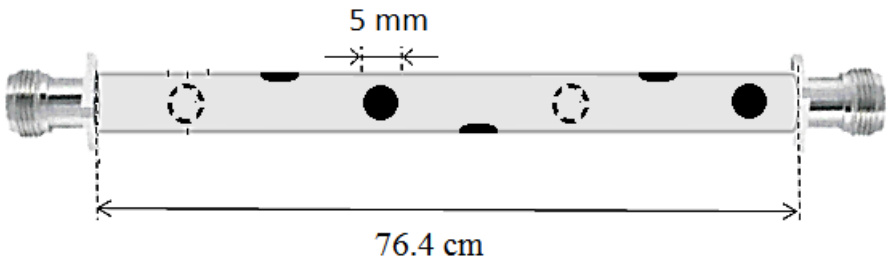

Figure 3.15: Preview on the coaxial airline. The cable has 20 holes of 5 mm diameter distributed in a helical fashion around an external copper tube of 76.4 cm long. The copper tube is 15 mm in diameter with a thickness of 0.65 mm. As far as the cable centre conductor is concerned, it is made of a brass rod of 6 mm diameter.

The measured Z_t are generally identical at higher frequency. The difference occurs for frequency less than 400 MHz. Over the frequency range, both curves are oscillating around the analytical prediction but the blue-line matches Kley's model better. This substantiates the LPDA efficiency findings in figure 3.12.

The next chapter focuses on the airline coupling in great detail, the origin of the oscillations will be given further.

3.9 Summary

A PCB-based LPDA antenna efficiency was investigated using the simulated efficiency of a small-dipole antenna and an RC. The dipole FEKO simulation was validated with simulated Wheeler-cap method. Agreement was seen between the LPDA measured efficiency and the CST prediction. The study highlighted the effect of the IEC recommended value of 0.75 on RC measurements if the actual LPDA efficiency is different. We found that the efficiency

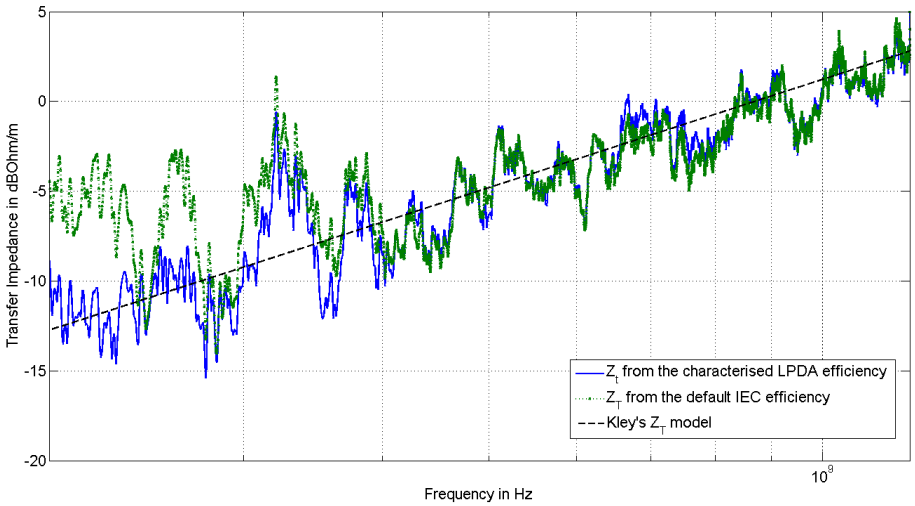

Figure 3.16: Coaxial airline Z_t from the characterised and the default IEC LPDA efficiency values.

of 0.75 has little bearing at frequencies well above our RC LUF. The main problems shown to appear at lower frequencies. A lowest LPDA RC-loaded efficiency value of around 0.1 was found at 200 MHz, causing errors of more than 10 dB in our chamber calibration data.

The investigation reveals that the RC antenna shapes the measurement data. A characterisation of the antenna efficiency is recommended for an accurate interpretation of the results. A methodology was presented here in this regard. Other techniques are also available in [67, 61, 63].

CHAPTER 4

Cable Z_t Characterisation for Time Domain Metrology Validation

The TD analysis and metrology has been used in high frequency technique since the mid-1960's. Nicolson, Bennet and Ross are some of the earlier names associated with this work [69]. Broadly, a TD metrology requires a proper generator, able to deliver a reasonable bandwidth, and a very sensitive receiver for wideband investigation. Often, the measurement dynamic-range constitutes the main difficulty associated with a TD measurement system. In most of the cases, cutting-edge technology components are central for the success of high frequency applications. Our TD metrology consists of a built-in pulse generator and a ROACH (Reconfigurable Open Architecture Computing Hardware) board based receiver, which have been designed in collaboration with colleagues from the University of Stellenbosch and the MeerKAT office in Pinelands. In this chapter, the first applications of our RC TD approach for validation are discussed.

The validation process consists of a gradual analysis of the coaxial cable presented in section 3.8.2. Through simulations and theoretical modelling, the cable coupling process is carefully examined. The chapter starts with an overview of the TD metrology components, the TD RC setup and the measurement control we used for the data capturing. Then, we switch to FD investigations for a better understanding of the cable response within an RC. Particular focus is given to feed-cables effect on Z_t. Once the cable coupling is understood and clearly explained, the TD approach is validated using comparative study between TD and FD results.

4.1 TD metrology Description

Generally, the TD metrology allows a signal characterisation up to 1.4 GHz using two major blocks: a pulse generator able to deliver such a spectrum and the SKA receiver called Real Time Transient analYser (RATTY).

4.1.1 RATTY Overview

The TD receiver used for the measurement corresponds to the second version of RATTY and is designed with three principal subsystems, as shown in figure 4.1, which are:

- the analogue front-end where the input signal is attenuated and filtered,
- the digital processing unit,
- the control-unit where measured data are stored.

The digital processing unit constitutes the core of the device. It combines a second generation ROACH and a 10 bit analog-to-digital converter (ADC) sampling at 1.8 GHz for signal characterisation up to 900 MHz. Within the analog front-end, the signal is subdivided into two channels which will be referred to as CH1 and CH2 within the dissertation. In our case, RATTY is used for broadband measurement up to 1.4 GHz. At the input of each channel, the signal level is adjusted through an interconnection of amplifiers and attenuators. Then, it is filtered for frequency conditioning and to prevent aliased signals from entering the chain. The CH1 filter works from 50 to 828 MHz while for CH2 it goes from 800 to 1400 MHz. CH1 is set to match the ADC sampled baseband and is directly routed to the digital processing unit. However, CH2 is down-converted to the baseband first, using an active mixer and a local oscillator of 1.5 GHz. RATTY is manually configured through the computer connected to the device (see figure 4.1). Maximum gains of 68 dB and 60 dB are achievable for both CH1 and CH2 respectively [55, 70].

4.1.2 Pulse Generator Basic Descriptions

Two pulse generators (PG1 and PG2) are used for the TD airline characterisation. Both were built in collaboration with Matthysen using avalanche transistors and step recovery diodes (SRD) [4]. The pulse generator schematic is given in figure 4.2.a and it is derived from the blueprint circuit presented in [54]. The actual pulse generator PG1 is shown in figure 4.2.b.

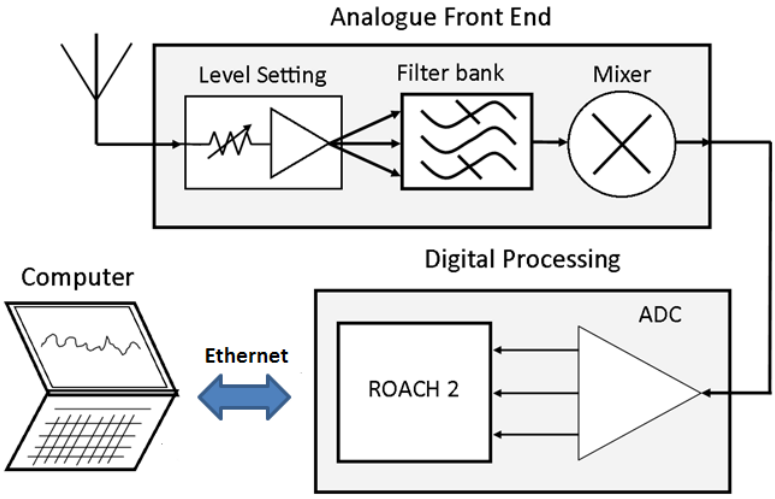

Figure 4.1: Ratty-2 schematic diagram. [55]

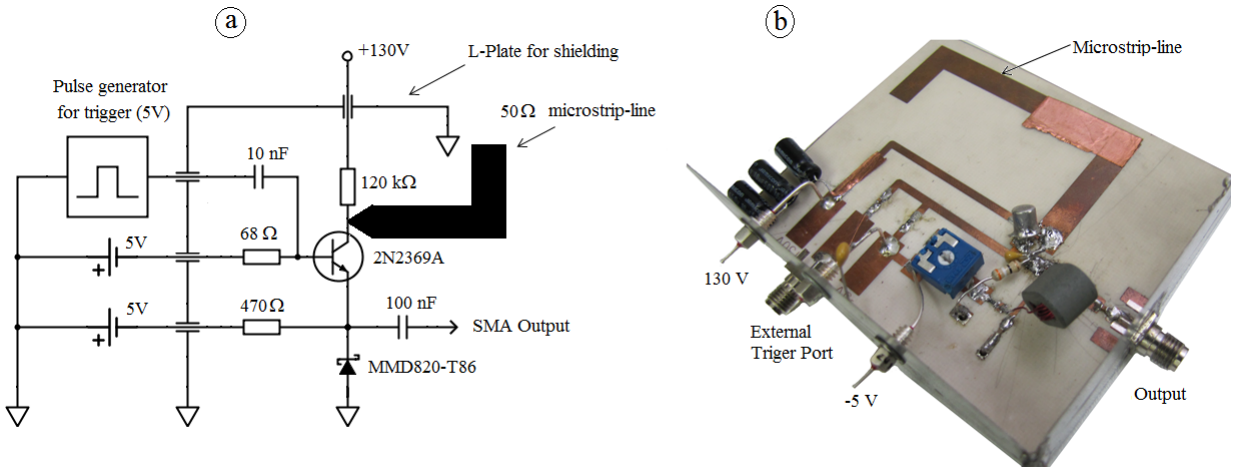

Figure 4.2: Overview of the pulse generator. (a) shows the pulse generator circuit diagram. (b) displays the actual pulse generator (PG1)

Internally, the main difference between the two pulse generators is the SRD used for the design. PG2 is also filtered to match the pulse spectrum with the RC bandwidth. The pulses were measured with the HP54750A sampling oscilloscope and are plotted in figure 4.3.

As can be seen from the figure, the pulses are not identical in terms of shape and spectrum. The filtered-pulse (PG2) has a flatter frequency response with a reduction of 5 dB over the range, in contrast to a 20 dB decrease for the dashed-curve. This behaviour originates from transition-time difference between the two circuits' SRD. PG2 uses a faster SRD and is able to generate a pulse with a smaller rise-time.

We acknowledge that the airline SE or Z_t should be independent of the generator char-

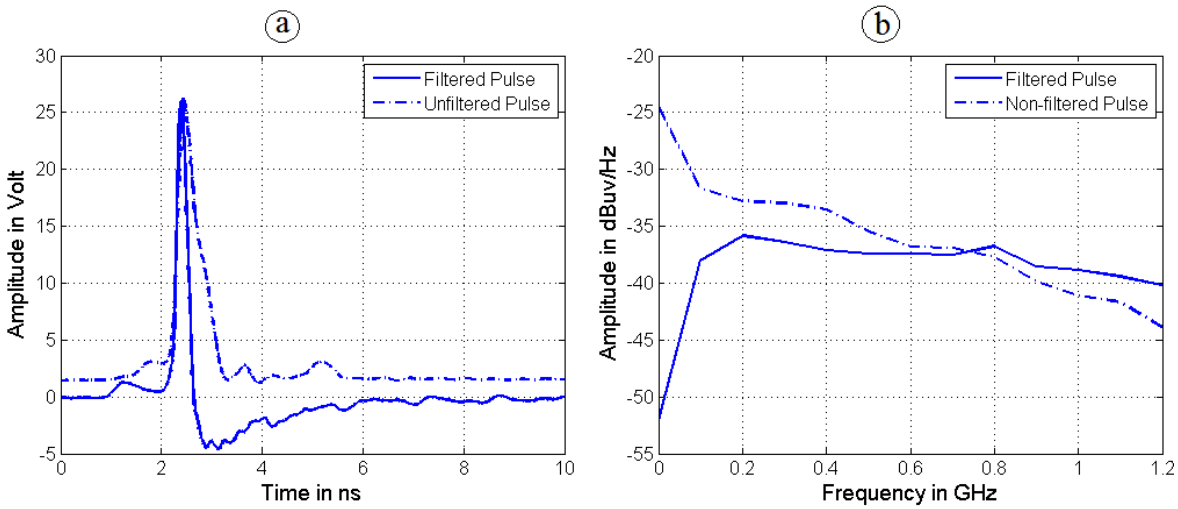

Figure 4.3: Pulse characterisation results using the HP54750A sampling oscilloscope. (a) shows PG1 and PG2 TD output signals. (b) displays the spectrum density for both generators

acteristics. Both the FD and the TD approaches are expected to give similar Z_t results. However, two generators are better for repeatability checking and for identification of features present on the Z_t curve which are not generator-related.

4.1.3 Setup Description

The measurement setup is presented in figure 4.4, where the cable under-test is placed above a polystyrene block within the chamber working-volume. It is matched with a 50 Ω load at the cable far-end to prevent the signal reflecting back into the airline. The other end is connected to the pulse generator, through a semi-rigid cable, for excitation. The pulse travels down the semi-rigid feed-cable, propagates inside the airline, and escapes outside the test-fixture through the holes located on the airline external conductor. The signal radiated within the chamber is thereafter measured with two receivers, through an LPDA antenna also sitting within the working area. These receivers are: a 50 GHz bandwidth sampling oscilloscope and RATTY. The oscilloscope is used in here as a reference for verification of the RATTY data.

The measurement is performed in mode-tuned operation where the stirrer is set in a static position. This has been chosen for the following practical reasons:

- First of all, because the pulse goes through multiple reflections within the RC, it is imperative that the RC configuration remains constant during the data capturing. Figure 4.5.b gives an overview of the pulse within the RC for a static stirrer position. Figure 4.5.a shows a train of pulses of 140 μs recorded with RATTY.

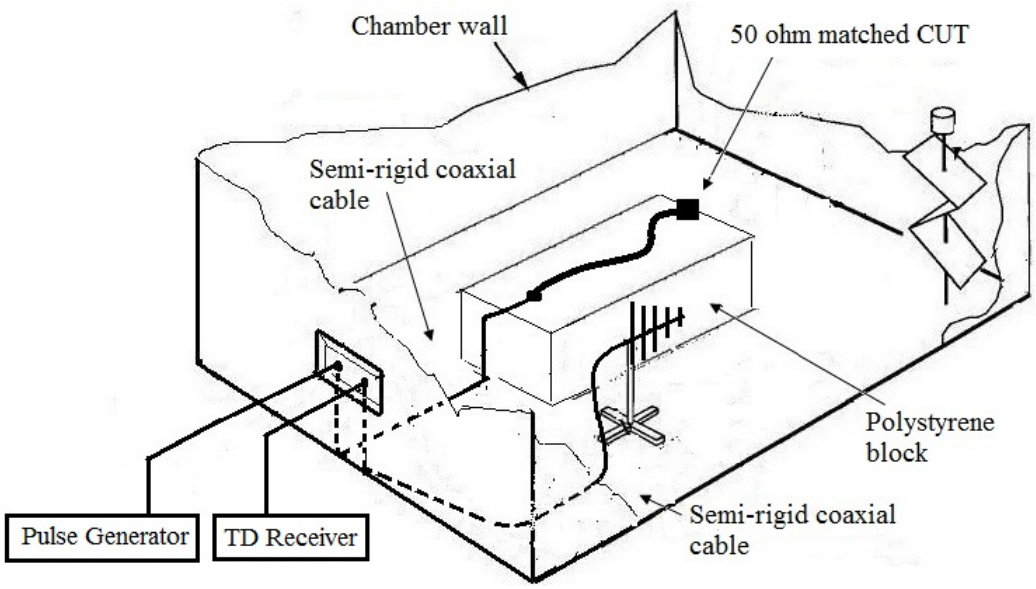

Figure 4.4: RC setup for the cable Z_t investigation. The sketch is modified from a picture in [1] and the cable-under-test is not required to be straight in the measurement

- Secondly, we wanted to collect as large a number of pulses per stirrer position as possible for a signal-to-noise ratio improvement by averaging.

The pulse radiation decays exponentially within the chamber as can be seen in figure 4.5.b. The chamber response lasts for around $6\mu s$. Because of this, a minimum pulse repetition-rate of 10 μs is used to prevent interference between two successive pulses. The record shown in figure 4.5.a corresponds to a pulse injection-period of 20 μs. The major thing we notice on the figure, and which is always seen with other records, is the maximum amplitude variation over the 140 μs capture. Matthysen studied this behaviour more deeply in his Master thesis [4]. He showed with measurement evidence that the jitter comes from a mismatch between the pulse-period and the receiver sampling-time. *i.e*, if the pulse maximum value occurs in-between two consecutive capturing events, RATTY will miss the data and will return a pulse with a lower amplitude.

4.1.4 Measurement Control Strategy

The success of the investigation depends closely on the measurement automation and control. For this reason, the stirrer controller has been updated to allow a mode-tuned operation. A MATLAB interface was designed to synchronise the stirrer movement, the data capturing and the storage. The whole process is controlled by a single computer where RATTY's laptop and the stirrer controller-board are connected as depicted in figure 4.6.

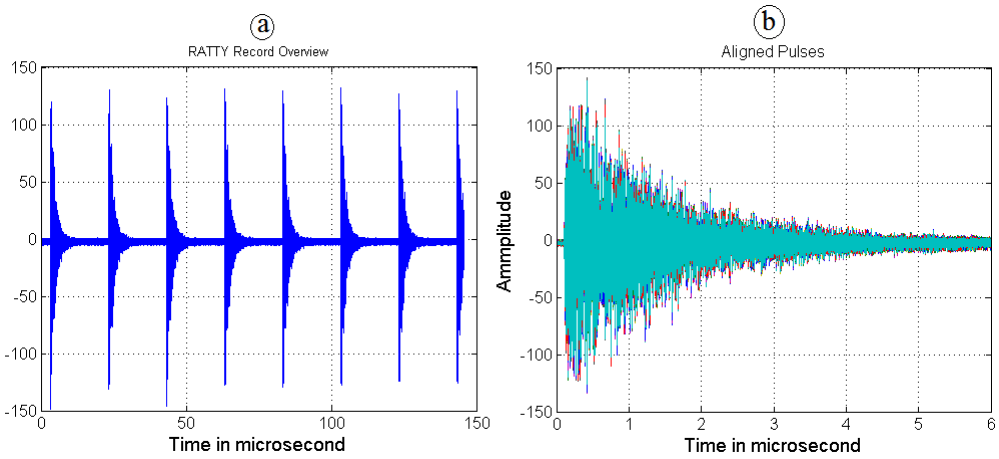

Figure 4.5: Overview on RC pulses recorded with RATTY. (a) shows a RATTY record length of 140 μs containing 8 pulses. (b) represents a single 6 μs reverberated pulse, extracted from the data shown on the left hand side of the picture.

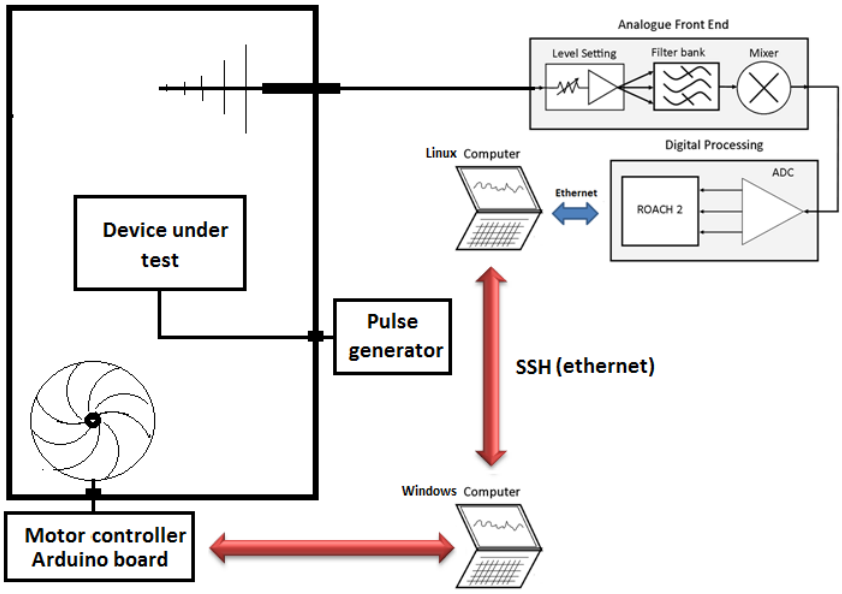

Figure 4.6: Synchronisation between RATTY and the chamber control for measurement automation.

4.1.5 Comments on the Setup Layout

The airline and the LPDA reflection coefficients were measured with a VNA and the results are shown in figure 4.7. The averaged reflections are represented by the bold-line in both figures. The background plots represent the individual S_{11} at each stirrer position.

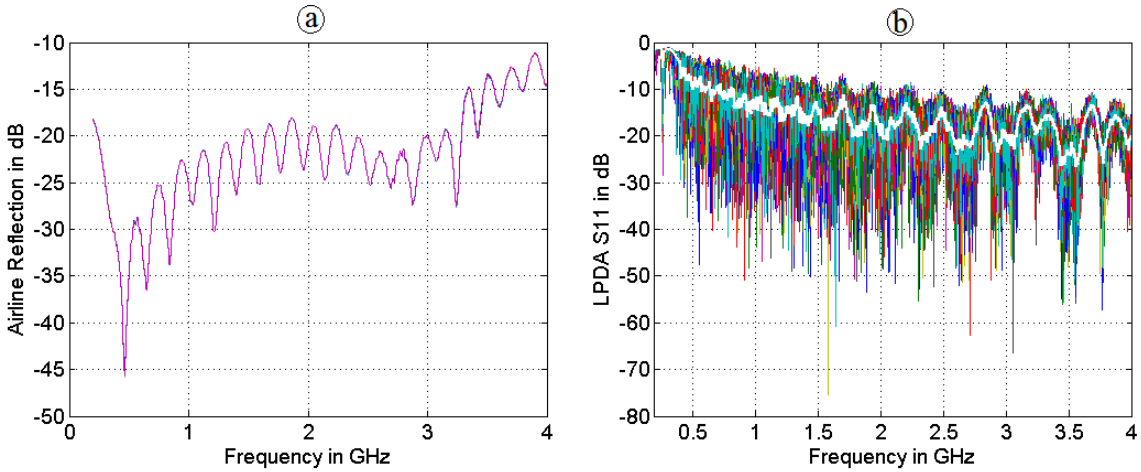

Figure 4.7: Airline and LPDA reflection coefficients characterisation inside the RC using the Rohde&Schwarz ZVB-8 VNA. The LPDA S_{11} is shown on the left-hand side of the figure

The chamber has an insignificant effect on the airline because no major difference is observed between the averaged curve and the individual S_{11} in figure 4.7.a. The airline is also well-matched over the frequency band in contrast to the LPDA S_{11} level. Due to these findings, we connected the pulse generator with the airline for a maximum power transfer within the RC-system.

4.2 Airline Computational Modelling

A finite-difference TD and a method of moment (MoM) simulation of the perforated airline are also performed. The upper-part of figure 4.8 shows the physical airline that we used for the measurement along with the computational model.

Figure 4.8: The actual airline and the FEKO model. The coupling zone measures 76.4 cm and 20 holes of 5 mm diameter are spread in a helical fashion around the cable external conductor.

Both the CST and the FEKO models are placed in a free-space environment and the Z_t investigation procedure is summarised as follows:

- The total-power radiated by the model in the surrounding space is first computed.
- The results are afterwards compared with the input power for an SE calculation
- Then, Z_t is derived from (2.12).

Respectively, near-field and far-field scans are requested around the FEKO and the CST models for the airline total radiated-power evaluation as shown in figure 4.9) in cyan and in yellow.

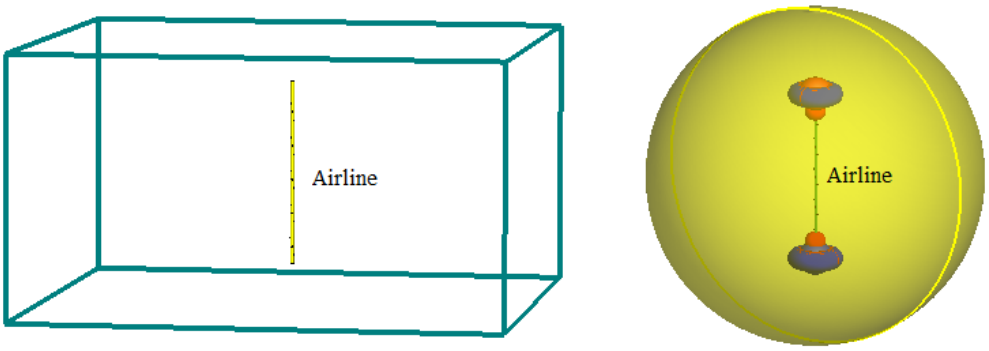

Figure 4.9: Far-field and Near-field surfaces used for the airline SE computation.

Physically, the simulation does not replicate entirely the RC measurement setup because the chamber and the stirrer are not taken into account in the modelling. However, both approaches are based on the same technique, which is the approximation of the airline total radiated-power, for the cable SE calculation. This is accomplished through the stirrer rotation for the RC measurement and through the near-field and far-field scans for the simulations.

4.3 FD Airline Z_t Discussion

Before we discuss the TD metrology results, an FD analysis of the airline Z_t is presented for a better understanding of the cable coupling behaviour. The FD measurements are undertaken within the chamber, using the same setup as shown in figure 4.4, with a VNA configured for a wider spectrum bandwidth up to 4 GHz. Two semi-rigid cables of 3 m and 50 cm are successively used for the airline excitation to identify the feed-cable contribution on Z_t. The results are shown in figure 4.10. Theoretical predictions according to Vance and Kley (see (2.8) and (2.9)) and the simulation outputs are also displayed for comparison.

It should be noted that both the measurements and the simulations are based on an

SE characterisation and that the SE data are converted to Z_t using the relationship in (2.12). Also, the newly acquired LPDA-efficiency and the chamber attenuation, presented in figure 3.12 and in figure 3.13, are utilised for all the calculations. For the CST and the FEKO modelling perspective, we limited the simulation to 1 GHz due to meshing and simulation-time considerations.

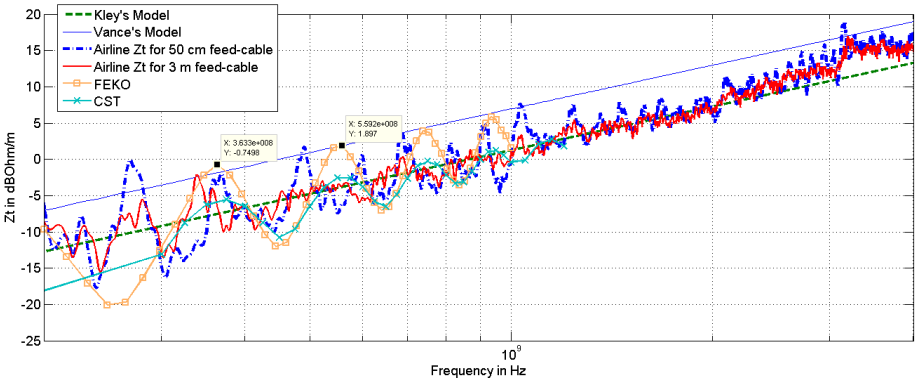

Figure 4.10: FD Z_t response for the perforated airline with 20 holes over the shield.

On one hand, the figure shows good agreement between Kley's model, the simulations and the measurements. But the measured Z_t deviates slightly from the analytical line from 3 GHz. One the other hand, Vance's model is 5 dB above all the other curves. This means that the apertures are not big enough in comparison with the airline external conductor thickness. As a result, Eddy currents and chimney effects take place in the coupling process as mentioned in [28, 29].

However, the agreement between Kley's model and the measurement is not always good if the number of holes per metre is changed. The finding is noticed from a Z_t survey for 2, 4, 8 and 16 holes using few pieces of copper tape to cover the unnecessary apertures. The results are shown in figure 4.11 and figure 4.12. The curves of the same colour depict the theoretical and the measured Z_t for the same number of holes. Figure 4.10 and figure 4.11 indicate that the higher the number of apertures, the closer the measurement to Kley's prediction. In contrast to that, in figure 4.12, the smaller the number of apertures, the better the agreement with Vance's model.

The masking tape could play a role on Z_T if the contact with the airline, around an aperture, is not good enough. To verify the tape contribution, we built a second airline with only 2 holes over the surface. The new airline is similar to the previous one in terms of the material used, the geometrical characteristics and the holes placement. The Z_t of the new airline is depicted by the back dashed-curve in figure 4.11 and figure 4.12. And as can be seen, there is a difference between the blue and black curve but it is less than 3 dB across the band.

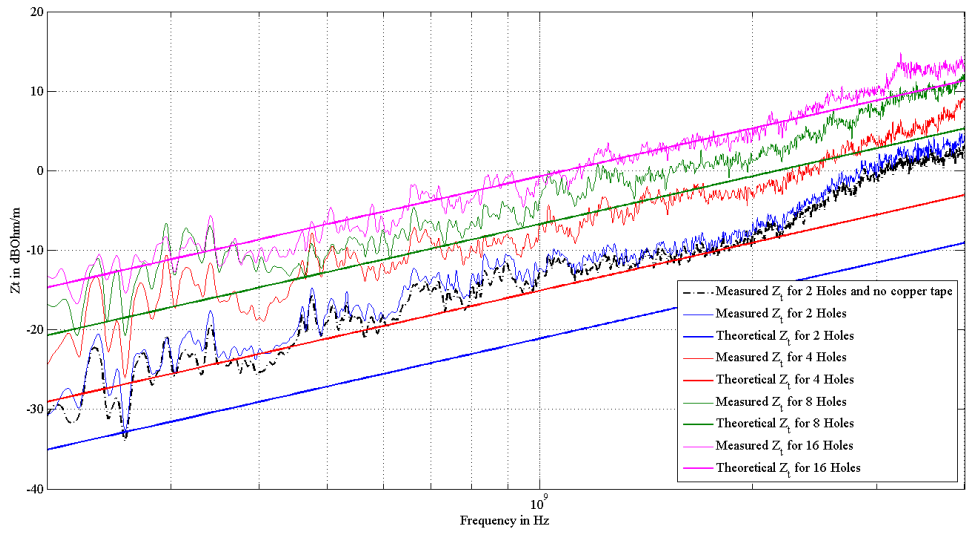

Figure 4.11: Variation of the airline Z_t according to specific number of holes and comparison with Kley's model.

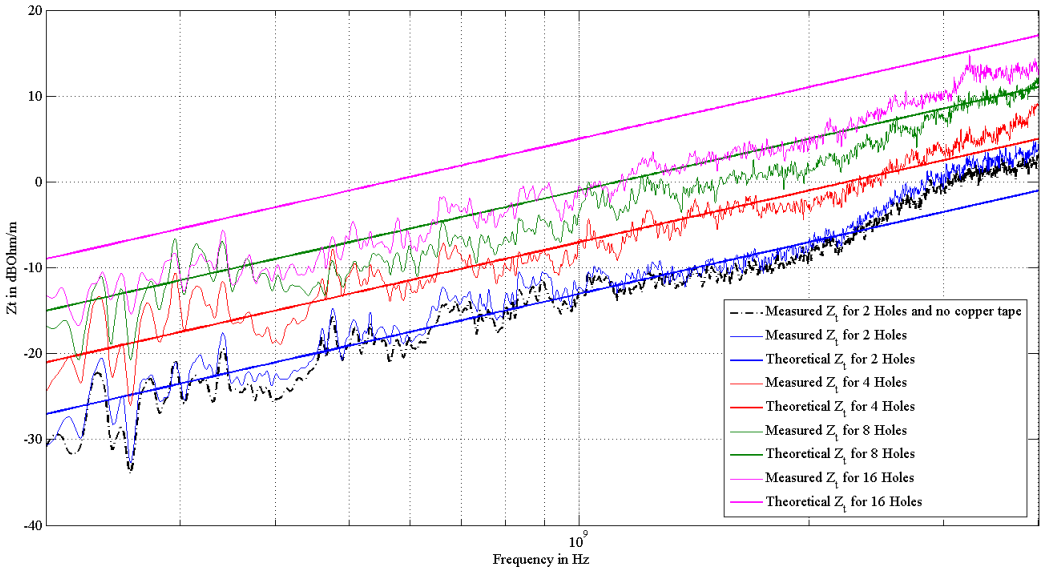

Figure 4.12: Variation of the airline Z_t according to specific number of holes and comparison with Vance's model.

4.3.1 Feed-Cable Contribution

The Z_t for the 20-hole airline in figure 4.10 is repeatable because a similar Z_t level is achieved for the 3 m and 50 cm semi-rigid cables. However, the curves oscillate differently around the theoretical prediction by Kley. The oscillation is commonly high at low-frequency and a gradual amplitude reduction is seen when the frequency increases. A clean sinusoidal pattern is observed for the configurations with no feed-cable, which corresponds

to the CST and the FEKO models, and the oscillation wavelength is approximately equal to twice the cable dimension. Therefore, it is clear that the airline resonates with the input signal and the resonance shapes Z_t. Figure 4.13 shows the simulated surface-current distribution at 1 GHz and for five phases. The figure confirms the presence of standing waves over the cable outer conductor. As a consequence, the feed-cable connection changes the airline surface-current distribution over the measurement. The setup resonance varies according to the feed-cable cable length and this explains the curves pattern difference in figure 4.10.

A comparison between the measured Z_t also shows that the longer the feed-cable, the lower the oscillation. Likewise, the longer the region covered by the standing wave, the higher the cable surface resistance. Thus, a plausible explanation of this behaviour is the increase of the outer conductor resistance which is attenuating the standing wave current more.

We also checked the simulated Z_t behaviour if metallic lines of different length and path are connected to the airline model to simulate a feed-cable excitation effect. The CST models that we used are shown in figure 4.14 and the results are given in figure 4.15. The computation clearly shows that the feed-cables shape Z_t. According to the black and the blue curves in figure 4.15, the curve pattern does not only change with the cable length; it also varies with the cable layout.

If we refer back to the results in figure 4.11 and figure 4.12, where the same semi-rigid cable was used for the investigation, we see that a common Z_t pattern is noticed between the Z_t curves. The trend is quasi-constant up to 2 GHz, for all the curves, and only the level changes when the number of apertures increases. This suggests that the holes mutual-coupling plays a minor role on the airline radiation. The feed-cable appears to be the main factor responsible for the oscillations.

4.3.2 Hole Mutual-Coupling Contribution

It is important to notice that the analytical formulations by Vance and Kley do not account for the apertures mutual-coupling. Thus, the agreement between Kley's model and the measurement in figure 4.10 can be considered as an a priori indication of the hole mutual-coupling having negligible effect. To affirm that this is the case, let us consider the model shown in figure 4.16 which is a portion of the previous airline FEKO model but where only two holes are selected.

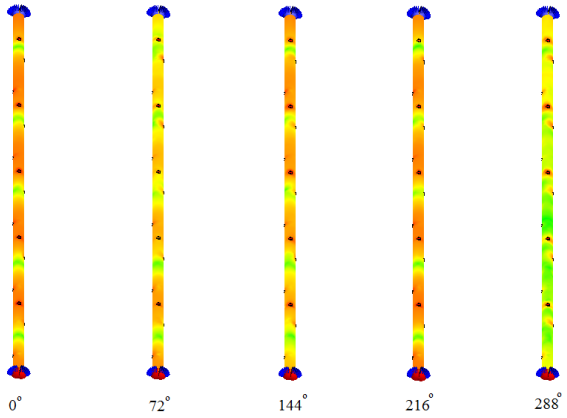

Figure 4.13: Simulated surface current distributions at 1 GHz and for a 72° phase variation to demonstrate the presence of a standing wave across the airline external shield.

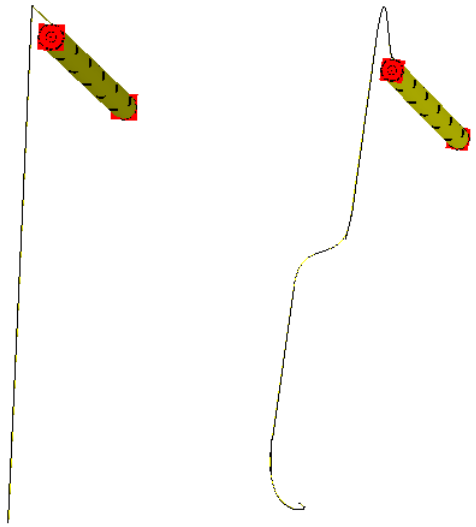

Figure 4.14: CST Modelling of feed-cables length and layout effects on Z_t

Model Description and Principle

If the hole mutual-coupling is too small, the law of conservation of energy permits us to say that the incident power at W_1 (P_{W1}) is equal to the sum of the power received at W_4 (P_{W4}), the power escaping through H_1 and H_2 (P_{H1} and P_{H2}) and the power consumed by the cable (P_{Loss}). Analytically, this can be generalised for a multi-hole case as follows:

$$P_{W1} \approx P_{W4} + \sum_{k=1}^{n} P_{Hk} + P_{Loss} \tag{4.1}$$

Conversely, if the hole-coupling contribution is high enough and the coupled-power re-radiation is negligible, the injected power for the two-hole airline satisfies the following

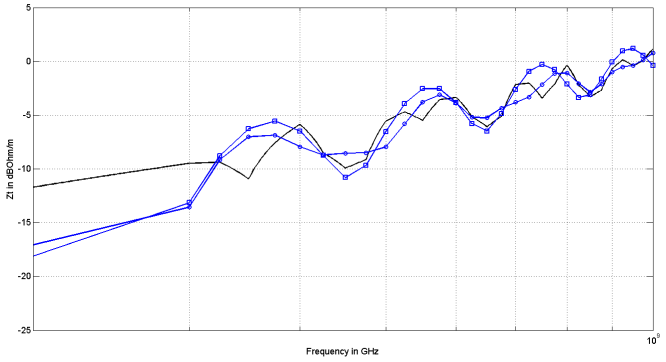

Figure 4.15: CST simulated Z_t pattern variation due to feed-cable connection for excitation.

expression:

$$\begin{aligned} P_{W1} &\approx P_{W4} + P_{H1} + P_{H2} + P_{Loss} + P_{H1H2} + P_{H2H1} \\ &\approx P_{W4} + P_{H1} + P_{H2} + P_{Loss} + 2.P_M \end{aligned}$$

where P_{H1H2} and P_{H2H1} are the coupled-powers from H_1 to H_2 and from H_2 to H_1.

The model is internally changed for the approximation of P_{H1H2} at W_4. The centre conductor between W_2 and W_3 is removed to cancel the direct path between A1 and A2 as shown in figure 4.16.b. Geometrically, the model can be visualised as a combination of two pieces of airline called A1 and A2. Both parts share the same external conductor to allow a continuous current flow over the outer conductor surface, which was the case for the 76.4 cm model.

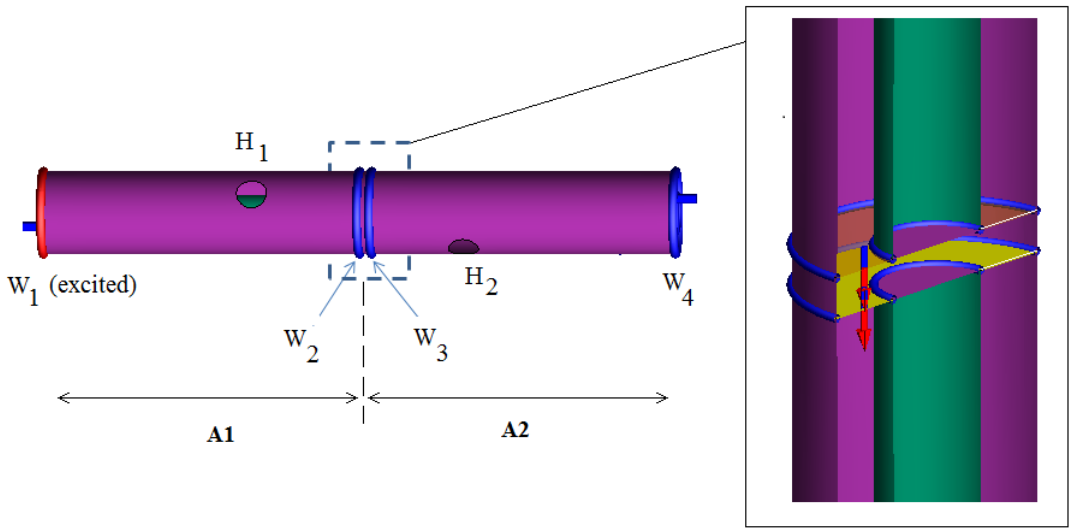

Figure 4.16: FEKO model for holes mutual coupling study. The cable model has two portions called A_1 and A_2. Four waveguide ports, W_1 to W_4, are used for excitations and measurements

Figure 4.17 and Figure 4.18 show the total E-field magnitude and the poynting vector pattern around the model. On the left hand-side of both figures we can see the model near-field scans when H_2 is absent.

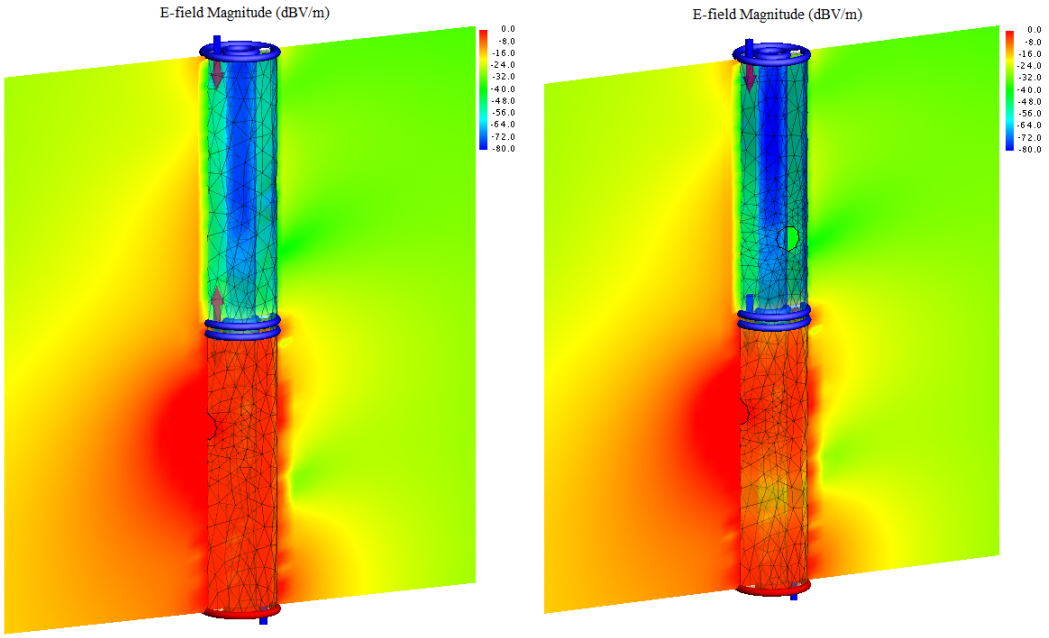

Figure 4.17: E-field pattern from a planar near-field scan defined around the model. H_2 is removed for the picture on the left-hand side. A_1 refers to the lower portion of the airline and A_2 the upper portion

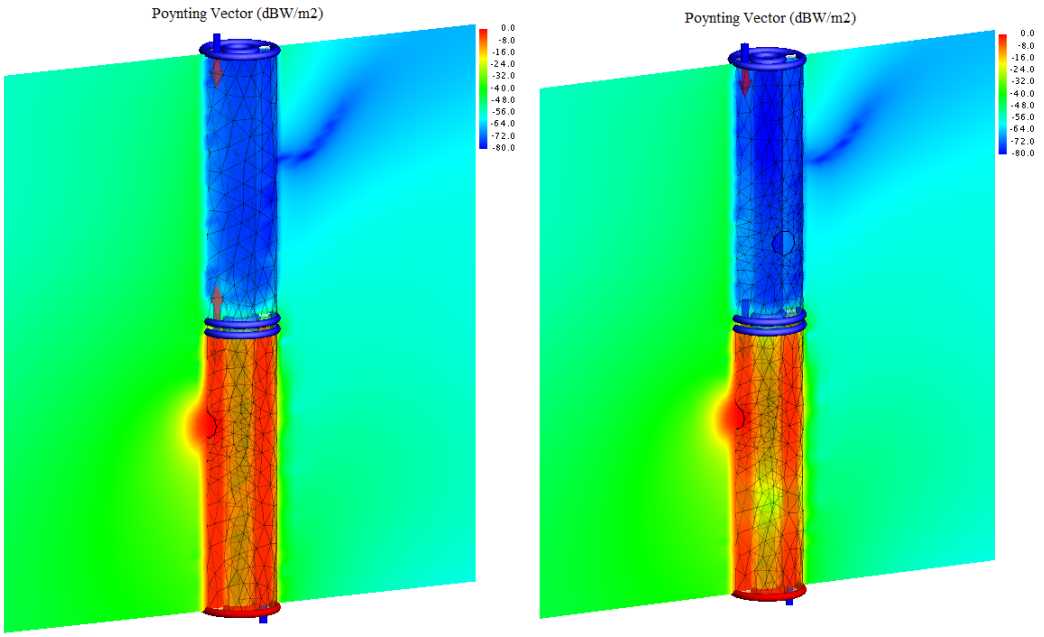

Figure 4.18: Poynting vector pattern from a planar near-field scan defined around the model. H_2 is removed for the picture on the left-hand side. A_1 refers to the lower portion of the airline and A_2 the upper portion

Discussion for the Model Placed in Free-Space

The colour transition around W_2 and W_3 indicates graphically the isolation of A1 and A2, and both figures clearly show the energy radiation from the hole (H_1). According to the S-parameter curves in 4.19.a and in figure 4.19.b, the signal propagates inside A1 from W_1 to W_2 and the excitation port is matched to the model. As far as the coupling between A1 and A2 is concerned, the signal transferred at W_4 is 95 dB lower than the input when H_2 is absent. Then, it becomes -89 dB in the presence of H_2 (see figure 4.20.b). This particular airline configuration gives a maximum coupled-power (P_{H1H2}) of -178 dB as depicted in figure 4.20.b. 2.P_{H1H2} is expected at W_4 when both holes, H_1 and H_2, radiate. These results show that the 5 mm diameter holes couple between each other but -174 dB is not strong enough to make an impact on the radiation behaviour.

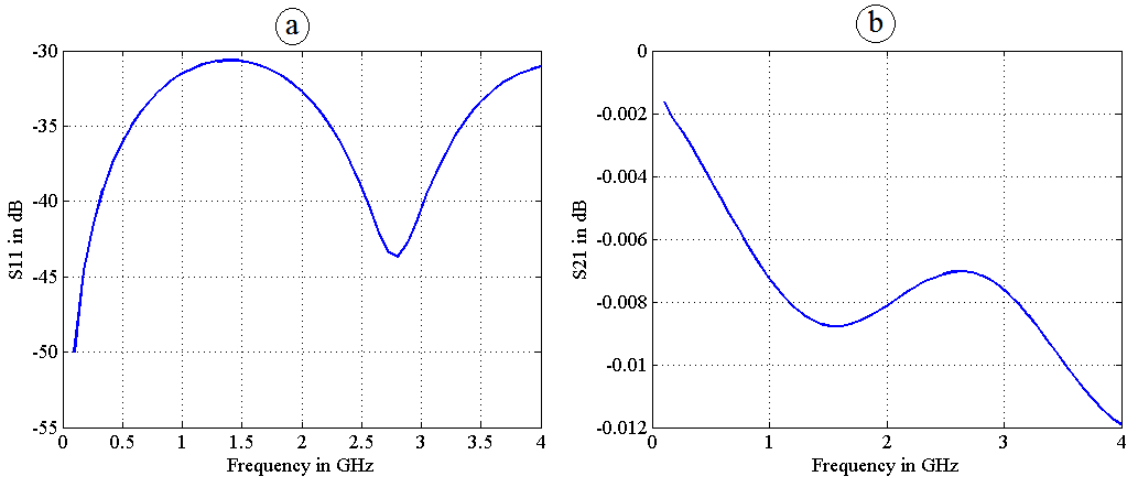

Figure 4.19: Reflection and transmission coefficients for A1, between W_1 and W_2.

Discussion for the Model Placed in RC

However, if we consider a thought experiment where the model in figure 4.16 is placed within an RC, we notice that the main difference between the previous FEKO simulation and the RC investigation is the amount of energy illuminating H_2. Within an RC, all the radiated signal can re-penetrate inside the airline in time (due to reflections and the stirrer rotation) while for the simulation, the signal going outward and moving away from H_2 would never couple back to the model centre conductor. Therefore, the power transmitted at W_4, through H_2, is expected to be higher for the RC case.

We know that the power radiated by an aperture (H_1) in the chamber is proportional to the hole SE. The chamber consumes an amount of that energy. The remaining power

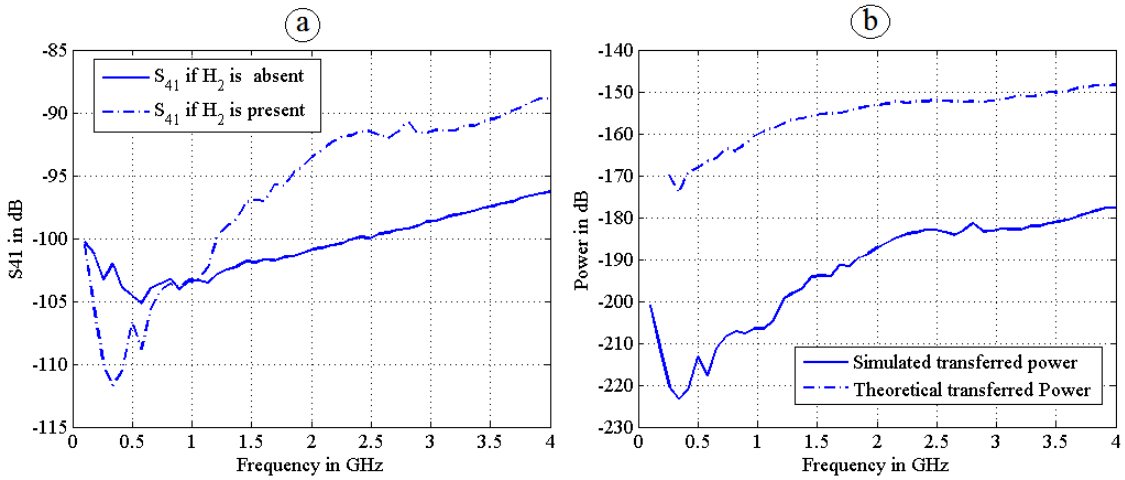

Figure 4.20: Coupling parameters between A1 and A2. (a) displays the variation of the simulated S_{41} according to the presence and the absence of H_2. (b) compares the FEKO simulated power reaching W_4 and the theoretical coupled power if the model is placed within an RC

couples through H_2 and generates a power also proportional with the hole Z_t at W_4. For a perfect port mismatch, the transmission between W_1 and W_4 is given by the expression in (4.2) using (3.2).

$$S_{41}^2 = \text{AVF}.SE_{1H}^2 \tag{4.2}$$

We evaluated S_{41}^2 theoretically using Kley's Z_t expression for a single aperture. The analytical Z_t is converted to SE using (2.12) and the result is shown in figure 4.20.b with the dashed-curve. Unfortunately, we do not have RC measurement data to support the finding due to technical difficulties associated with the model realisation. But the approach can give us an approximate idea about the amount of power transferred in A2 from H_1. As explained before and also seen in figure 4.20, the hole mutual-coupling is higher within the chamber. This tells us that the CST and FEKO Z_t results presented in figure 4.10 incorporate less hole mutual-coupling effect than the RC measured Z_t. Because both are oscillating around almost the same level over the range, we can interpret this as an ineffective hole mutual-coupling.

Hole Mutual-Coupling Estimation for the 20-Hole Airline

If we expand the analysis with a multi-hole airline, using the same principal as before, we find that the RC total power from n-hole is n times higher than the power radiated by a single hole configuration. Both apertures are subjected to the same RC fields. A total

transmission coefficient satisfying the expression in (4.3) is expected.

$$S_{41}^2 = \text{AVF}.(n.SE_{1H})^2 \tag{4.3}$$

The airline with 20-hole case gives:

$$S_{41}^2(dB) = 26.02 + 10.log[\text{AVF}.(SE_{1H})^2] \tag{4.4}$$

which is less than -100 dB if we substitute the value presented in figure 4.20.b in (4.4). As a consequence, the power injected within the 20 holes airline fits the expression in (4.1), where the coupled-powers are neglected.

4.4 TD Airline Z_t Discussion

The TD measurement technique is undertaken according to the setup in figure 4.4 using the filtered and the non-filtered pulses in figure 4.3. The data are collected with both the HP50750A and RATTY and the results are shown in figure 4.21.

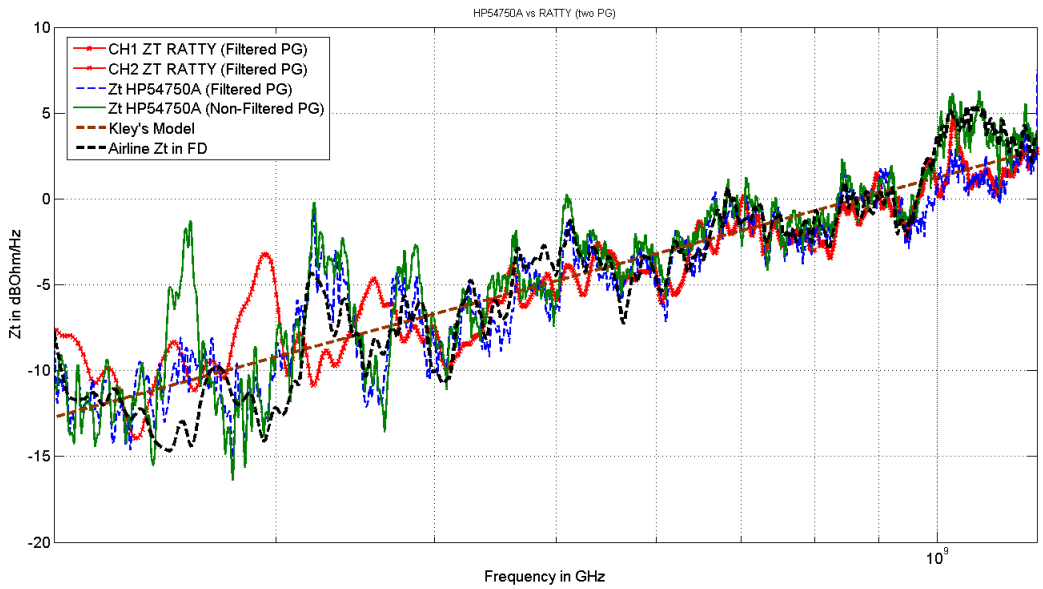

Figure 4.21: TD Z_t results for the airline with 20 holes across the shield. The investigation uses RATTY and the HP54750A sampling oscilloscope as TD receivers.

For the HP50750A receiver, a 36 dB amplifier was used to increase the LPDA output signal due to a measurement dynamic-range issue. This was not however the case for RATTY. For both receivers, Z_t results up to 1.2 GHz are achieved and are shown in figure

4.21. The green and the blue curves are measured with the sampling oscilloscope while the red-line represents RATTY's output. The Kley's analytical curve for 20 holes and a FD Z_t result are also plotted for comparison. It is clear from the figure that the airline Z_t is repeatable and it is independent of the pulse generator. Similar to the FD domain Z_t result, the TD curves also oscillate around the theoretical line of 20 dB per decade variation. However, the curves pattern are different between RATTY and the sampling oscilloscope results for frequency less than 400 MHz. The reason for this behaviour was not investigated further since the mismatches between the pulse generator and the TD receivers are not taken into account in the computation. Nevertheless, the TD and the FD Z_ts are in agreement and this can be interpreted as a validation of the TD approach.

4.5 Airline Z_t Error Estimation

4.5.1 Stirrer Efficiency Evaluation

For an RC technique, the measurement uncertainty depends on the stirrer efficiency. The error is derived from the existing number of independent samples, N_{Ind}, that the tuner can provide among the N_S stirrer positions used for the recording. The standard methodology used for the calculation of N_{Ind} is described in [1, p. 22]. For a short description, N_{Ind} is approximated from the data autocorrelation coefficient ρ which is expressed as follows [1, 58, 59]:

$$\rho_i = \frac{Cov(X, Y_i)}{\sqrt{Var(X).Var(Y_i)}} \tag{4.5}$$

where X represents the sequence of data over a stirrer revolution and Y_i contains the same value as X but shifted by i position. Analytically,

$$if \quad X = [D_1, D_1, ..., D_{N_S}] \tag{4.6}$$

$$Y_1 = [D_{N_S}, D_1, ..., D_{N_S-1}] \tag{4.7}$$

$$Y_2 = [D_{N_S-1}, D_{N_S}, ..., D_{N_S-2}] \tag{4.8}$$

The data in X are considered as uncorrelated if $|\rho| \leq 0.37$ [1]. The position, Δ, where the condition is violated is identified on the autocorrelation curve for the N_{Ind} calculation, according to the expression in (4.9). Figure 4.22 shows the autocorrelation curves we obtained for the 72 stirrer positions which permitted the Z_t investigation. Each line depicts

the individual ρ for each frequency and the dashed-curve represents the correlation limit of 0.37. In general, among the 72 data recorded over the tuner revolution, around 45 are independent for frequency more than 1 GHz as shown in figure 4.23.

The methodology for the estimation of N_{Ind} is a matter of ongoing research in the EMC community and on this depends the quality of the error attributed to RCs measurement. The chapter presents no major feedback on the issue. So, the study is limited to the application of the IEC 61000-4-21 uncertainty calculation procedure. Recent publications on the matter is given in [71, 72, 73].

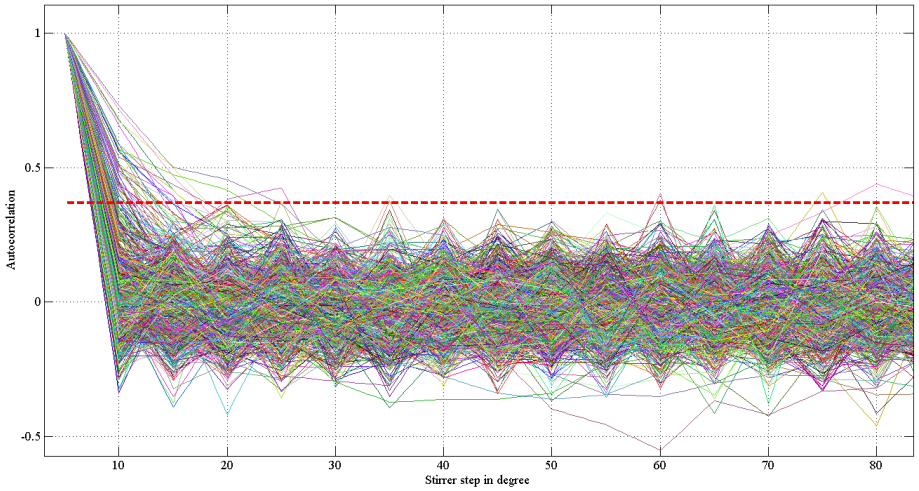

Figure 4.22: Autocorrelation curves for 72 stirrer positions and for each frequency.

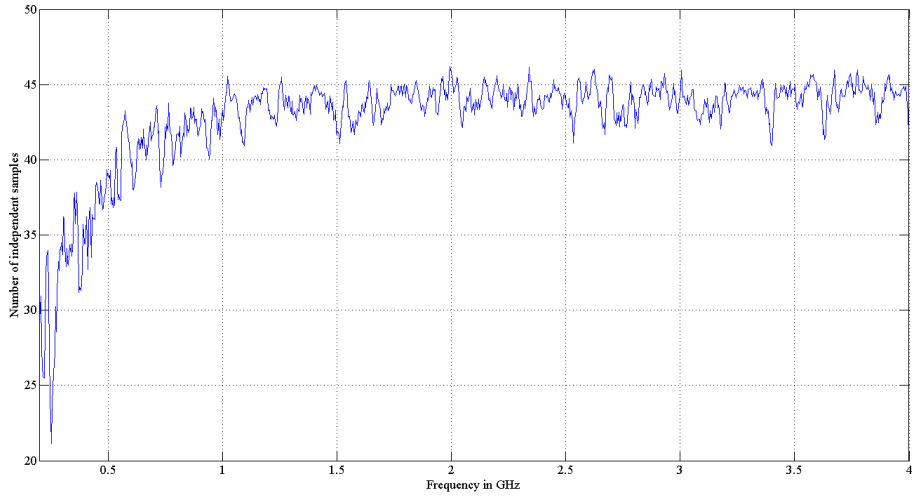

Figure 4.23: Our RC independent samples according to the IEC 61000-4-21 autocorrelation function technique [1].

$$N_{ind_i} = \frac{N_S}{\Delta_i} \tag{4.9}$$

4.5.2 Z_t Confidence Intervals

The measurement confidence interval (d) in dB is derived from the N_{Ind} values found in the previous section. It is expressed as follows [74, 75]:

$$d = 10.log\frac{1 + k/\sqrt{z.N_{Ind}}}{1 - k/\sqrt{z.N_{Ind}}} \tag{4.10}$$

where k denotes the level of confidence and z is the data dimension (z = 1 for our case because for each frequency, the LPDA is oriented in one direction only).

A confidence interval of 90% and 60%, for k = 1.64 and k = 0.841, are represented in figure 4.24 with the shaded area around the Z_t curve in purple and in green. The curve standard deviation is also shown for an overview of the Z_t possible range of variation.

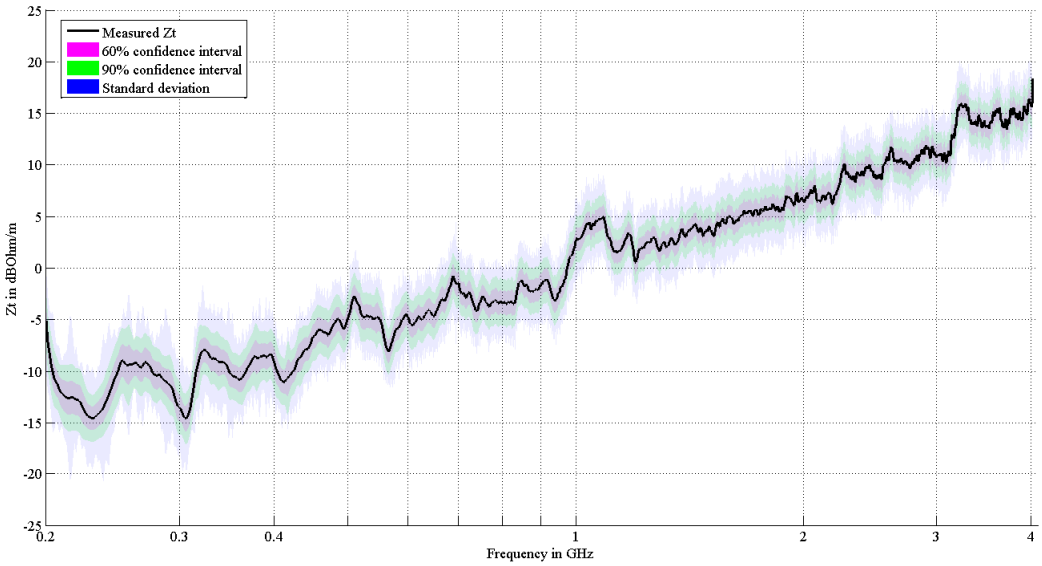

Figure 4.24: Confidence interval for the measured Zt.

4.6 Summary

A built-in coaxial airline has been examined for the validation of our TD metrology. The task was based on a rigorous examination of the cable SE in FD using theoretical and computational models. The test-fixture effect on the measurement was a particular focus. We found that the RC feed-cable shaped the airline Z_t and the airline inserted an unavoidable oscillating pattern within Z_t. However, the resonance was reduced for a longer feed-cable. In this regards, a longer cable-fixture is recommended for cable characterisation. The study also showed that the Z_t of a multi-hole cable is equal to the sum of the Z_t of

each apertures. The more hole we have over the airline the better the agreement with Kley's model. For the TD investigation perspective, an agreement was seen with the FD investigation.

CHAPTER 5

Modified Nested-Enclosure Technique for Enclosure SE Evaluation

Electromagnetic fields are distributed differently in space within an interference-controlled environment such as a metallic enclosure. In this context, the measurement location always poses a problem for a SE characterisation due to shield resonances. Various methods are summarised in the IEEE standard [2] to tackle the issue according to the EUT size. For small enclosures in particular, a reverberated environment principle is proposed. The methodology is known as the nested-enclosure technique, where both the EUT external and internal regions are stirred by mechanical paddles or with a different kind of stirring procedure. However, the method is not always efficient and depends on other factors such as the enclosure dimension or the measurement strategy adopted for the investigation. For instance, the smaller the enclosure, the higher the constraint for a mechanical stirrer inclusion. For such a case, a frequency stirring can be used as an alternative methodology as described in [2, 45, 57, 76]. Issues concerning the measurement bandwidth also arise for a TD investigation for small shields.

A FD version of the nested-enclosure-method is often a time-consuming investigation due to high number of samples required by the technique. A TD approach to the problem is applied for time speed-up using the metrology presented in the previous chapter. The nested-enclosure technique setup is slightly changed to consider the EUT under-moded region.

5.1 Nested-Enclosure Technique Description

5.1.1 Setup Overview

Conventional nested-enclosure Technique Setup

The setup for the conventional nested-enclosure technique is presented in figure 5.1. In principle it is similar to the configuration we used for the coaxial airline Z_T investigation, with a small exception where the enclosure internal region is stirred by a mechanical tuner. Internally, the signal injected in the EUT does not propagate but forms a standing wave pattern, due to boundary conditions. The EUT stirrer permits an approximation of the maximum or the average-field produced inside the enclosure. To meet this requirement, a battery-driven, programmable and portable-stirrer was made. It was built in collaboration with a mechanical engineer from the University of Stellenbosch using a micro-controller and a stepper-motor as roughly shown in figure 5.2. The tuner is placed inside a mild-steel enclosure of 60 cm by 50 cm by 40 cm, where the blade consists of a twisted copper-sheet 40 cm long.

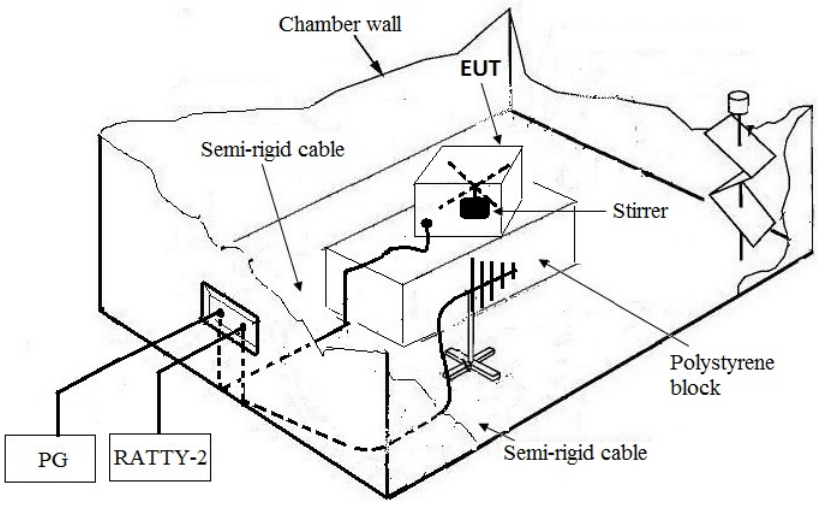

Figure 5.1: TD setup for the nested-enclosure technique

Four probes are positioned inside the EUT, as will be presented later, and the S_{21} parameter between the chamber LPDA antenna and the probes are recorded per tuner-step. Both the RC and the enclosure stirrers, respectively called ST1 and ST2, are synchronised for the collection of the field distribution within the system. For our case, ST1 is configured in mode-tuned operation while ST2 is set for a continuous rotation at 3 RPM. An accessibility issue occurs once the enclosure lid is in place so this particular ST2 mode of operation is chosen for the SE investigation. ST1 remains static during the time ST2 goes for one

revolution. Afterwards, the RC controller moves ST1 to the next position and the whole procedure is repeated until it completes a full turn.

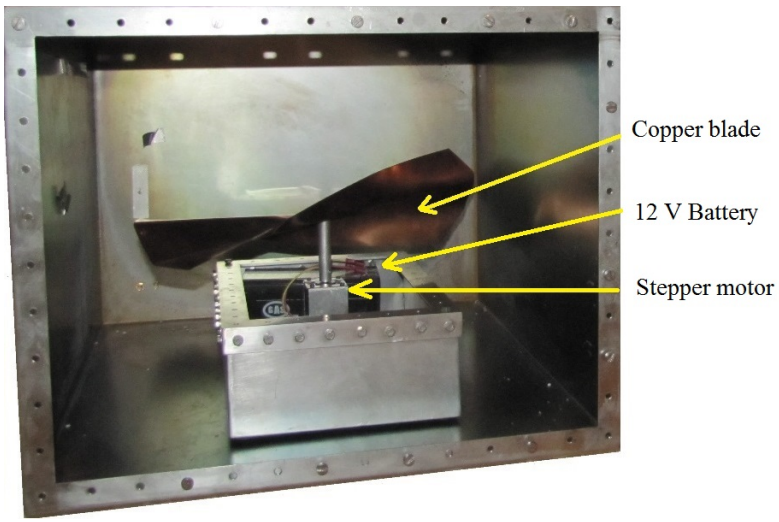

Figure 5.2: The portable and battery-driven stirrer

The Modified Nested-Enclosure Technique Setup

For the modified nested-enclosure technique setup however, the EUT stirrer is removed. The EUT behaves as a normal cavity resonator and only the RC region is stirred. The new system is similar to the coaxial airline investigation configuration in figure 4.4.

5.1.2 SE Calculation Principle

The IEEE definition for SE, in [2], is used for the shielding characterisation as given in (5.1). Briefly, SE is derived from the ratio of the power transmitted into the box (P_{EUT}) and the power radiated into the RC, P_{RC}, and is as follows:

$$SE = \left| 10\, log \left(\frac{P_{RC}}{P_{EUT}} \right) \right| \tag{5.1}$$

For an FD investigation, the configuration shown in figure 5.3 is used. The input signal from Port1 divides into three parts: the first portion is reflected by the excitation probe, the second is stored in the enclosure and the last part is consumed within the metallic boundaries due to ohmic loss. In the above equation, P_{EUT} incorporates both the stored power and the enclosure attenuation contribution because both characterise the EUT. With the input power from Port1, P_{In}, P_{EUT} is as follows for each mode:

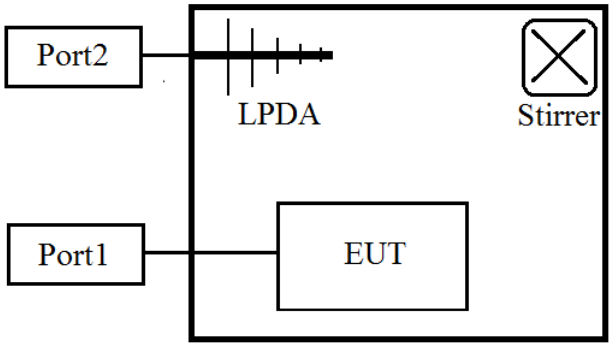

Figure 5.3: Schematic representation for the FD setup of the nested-enclosure technique

$$P_{EUT} = P_{In}.(1 - |S_{11}|) \tag{5.2}$$

This P_{EUT} expression is valid for the non-stirred EUT. However, it is calculated from the average or the maximum reflected power for the normal nested-enclosure technique setup.

The enclosure stored-energy escapes through apertures located on the wall and radiates a total power P_{RC} into the chamber. By treating the EUT as a normal radiator, the emission is given by the expression in (5.2) using the IEC standard equation for DUT radiated power investigation [1].

$$P_{RC} = \frac{P_{Out}}{(1 - < |S_{22}|^2 >_n)\, \eta_{LPDA}\, \text{CVF}} \tag{5.3}$$

where

- η_{LPDA} is the LPDA antenna efficiency.
- P_{Out} is the power transferred at Port2.
- CVF represents the RC loss parameter in the presence of the enclosure.
- $< |S_{22}|^2 >_n$ represents the LPDA averaged reflections over 72 RC-stirrer positions.

Knowing that $S_{21}^2 = \frac{P_{Out}}{P_{Inj}}$, both (5.2) and (5.3) give:

$$SE = 10\, log \left(\frac{S_{21}^2}{(1 - |S_{11}|^2).(1 - < |S_{22}|^2 >_n)\, \eta_{LPDA}\, \text{CVF}} \right) \tag{5.4}$$

5.2 Constraint and Peculiarity of the Study

5.2.1 TD metrology Issue

According to an RC technique principle and if we assume that the EUT and its internal stirrer forms a smaller RC, the SE values we get from the investigation are accurate from three times the enclosure lowest resonant frequency [1]. This limitation corresponds to the EUT LUF where ST2 becomes efficient and the field uniformity is established. The enclosure lowest cut-off frequency is equal to 390 MHz for the dimension given in section 5.1.1, and this corresponds to a theoretical LUF of about 1.17 GHz. By accounting for the TD metrology frequency spectrum, which goes up to 1.4 GHz, we see that the TD investigation yields an SE for the EUT mostly in its under-moded condition. Therefore, ST2 potentially has no value for a frequency less than 1.17 GHz. The setup satisfies the conventional nested-enclosure technique condition for frequencies above 1.17 GHz.

5.2.2 Special Case

Literature does not report any cases of SE investigation in the under-moded condition of an enclosure. Also, the IEEE standard makes no mention of the subject, so we believe the study contributes to this issue. For this inefficient stirrer configuration, the problem goes back to a modal analysis. The modes distribution inside the EUT and the probe location are carefully investigated to derive an accurate SE evaluation.

Most of the work concerning the nested-enclosure technique, and also stated in the IEEE standard [2], illuminates the EUT from a source placed in the RC. In this study, the source is placed inside the box and we treat the system as an ordinary radiator. We believe the approach can be used to speed-up the measurement by obviating the need for the EUT stirrer.

5.3 EUT Excitation Examination

5.3.1 Excitation Placement for Efficient Modes Coupling

The enclosure excitation is of major importance because of dynamic range issues for the TD metrology if the system is poorly excited. For this reason, a CST eigen-solver simulation

of the box was undertaken to visualize the field distribution. The figures support the explanation for our choice of probe configuration.

For an E-field excitation, such as a dipole or a monopole antenna, we have the highest coupling if the probe is placed at a mode's maximum E-field spot, which is indicated by the red colouration in figure 5.4. The E-field probe placement is rather a difficult task for a multi-frequency analysis because one must place the probe at a common maximum node location to be able to excite all the modes efficiently. Figure 5.4 clearly shows that such a position does not exist. However, we can identify a location where several modes couple perfectly with the dipole. For instance, if the probe is placed at the centre of the model, it will excite the mode 390 MHz in the left corner of figure 5.4, and, any odd modes of the form (2m+1,2n+1,2p+1), such as (1,1,1), (3,3,3) and so on.

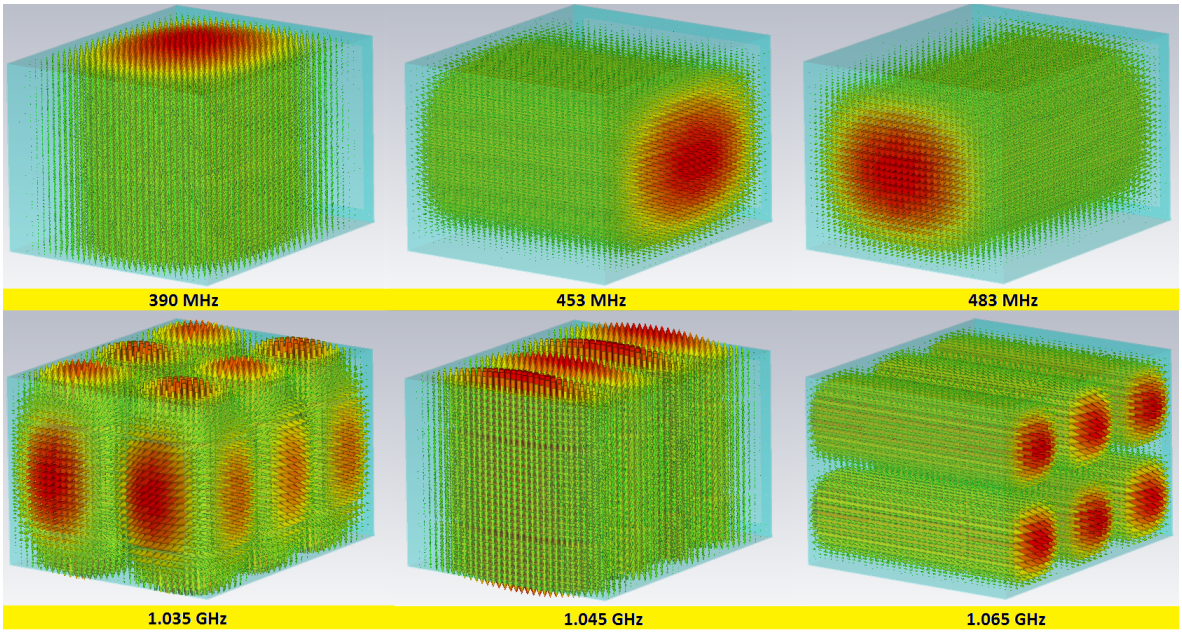

Figure 5.4: E-field pattern within in the enclosure for six modes. The first row corresponds to the three lowest modes. Three other upper modes, in the gigahertz band, are shown in the second row.

For an H-field probe however, which is generally a loop antenna, the maximum coupling occurs if the probe cuts the highest H-field line within the enclosure. Similar to the E-field case, the loop must be also located in a place where all the H-field lines transit in order to excite maximum number of enclosure modes. Figure 5.5 shows such a location. The H-field lines for the six selected frequencies are all passing at the enclosure corners as shown by the arrows. However, one loop is not enough for the task. If we refer to the probe shown in figure 5.6, it is clear that the H-field parallel with the loop cannot be excited. Two rectangular loops are sufficient to couple with all the H-field directions but three are better if such a configuration is possible. For the measurement, four 5 cm loops

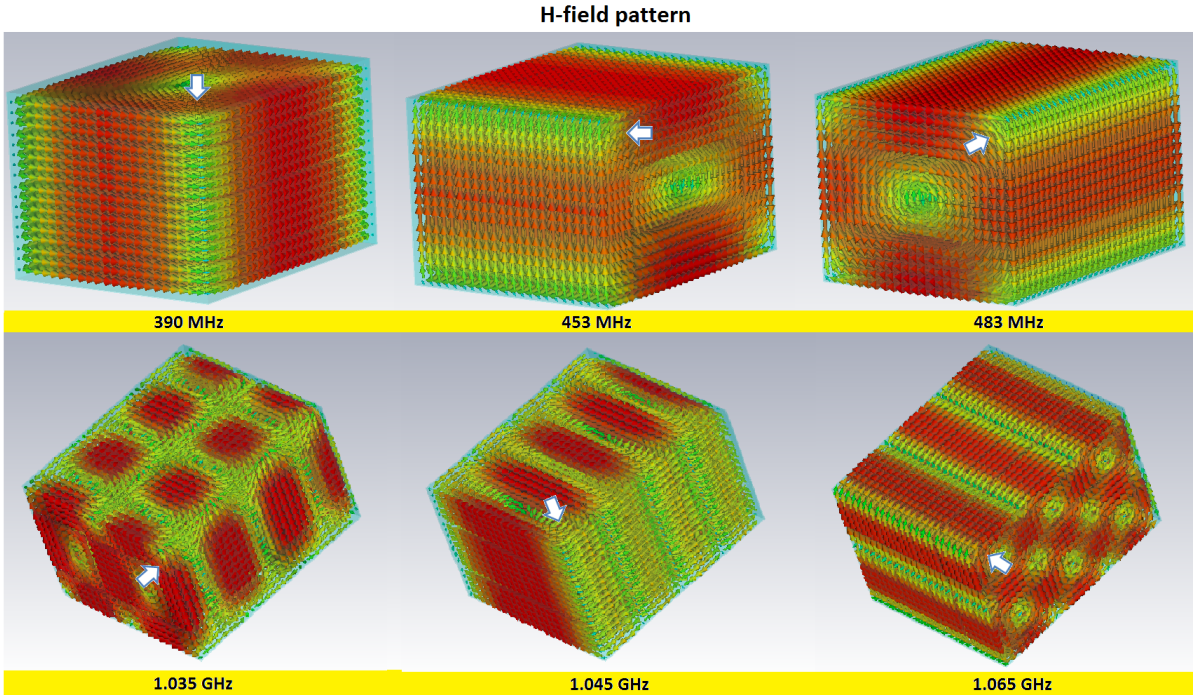

Figure 5.5: H-field pattern within in the enclosure for six modes. The first row corresponds to the three lowest modes. Three other upper modes, in the gigahertz band, are shown in the second row.

are placed within the enclosure as shown in figure 5.7.a. For the SE investigation, only two of the four loops are excited using a commercial two way in-phase splitter depicted by the diagram in figure 5.7.b.

Figure 5.6: One of the vertical square-loop used for the EUT feeding, placed at the enclosure's right corner. The loop measures 5 cm by 5 cm and it is placed 5 cm away from the corner

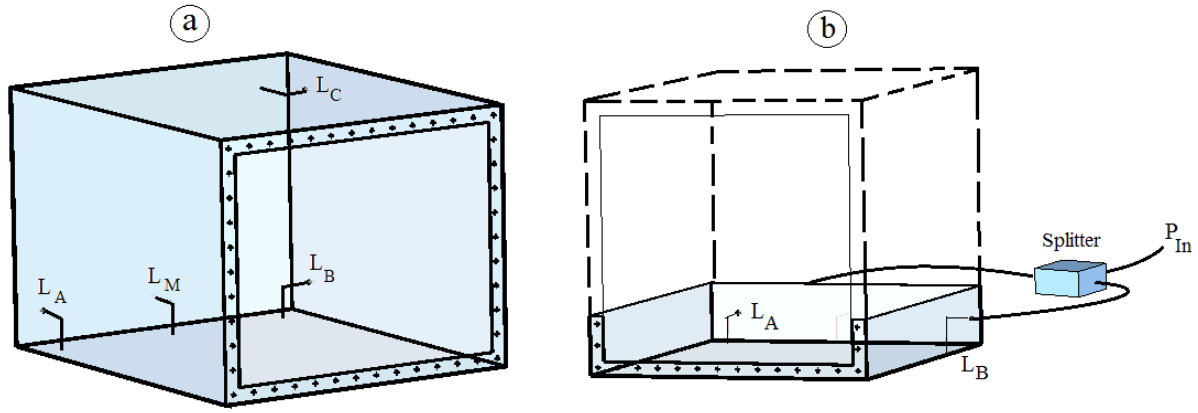

Figure 5.7: The four rectangular loops locations within the enclosure and the split-probe configuration. (a) shows the four loops while (b) depicts a split-probe connection between L_A and L_B

5.3.2 Remark on the Configuration

The total power transferred into the EUT for the dipole and the split-probe are different because the coupling changes according to the excitation quality. However, a similar SE should be always measured for the modes since SE is a ratio of the EUT internal and external powers. We believe the split-probe allows a better coupling with the modes and is chosen for the investigation. It is examined in more detail in the next section before the actual EUT SE is presented.

5.3.3 Split-Probe Excitation Validation

The feeding constitutes the key of the investigation. If nothing is injected into the enclosure, the VNA measures the RC noise through the LPDA. This will be interpreted as a low SE value. The split-probe excitation in figure 5.7.a has been simulated in CST using the TD solver to ensure that modes are created inside the enclosure. The model is simultaneously fed from L_A and L_C using the option "selection" of the TD-solver interface. Thereafter, the enclosure internal radiation is collected through L_B and the simulated S_{21} is shown in figure 5.8 in red. The blue curve represents a measurement with VNA. The exact conductivity value of the enclosure is unknown so the CST steel-1008 material is used for the modelling.

The measurement and the simulation generally agree in terms of the pattern trend and the spikes. However, different magnitude levels are seen for some frequencies. The conductivity difference between the CST-model material (steel-1008) and the physical enclosure (mild-steel), may be partly responsible for this behaviour. The spikes on the figure correspond

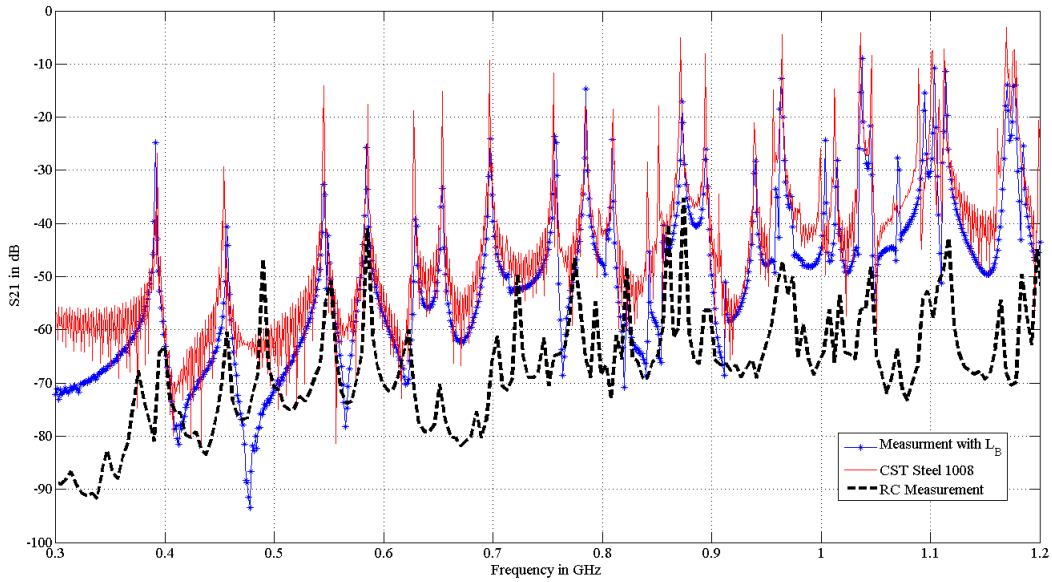

Figure 5.8: Simulated and measured enclosure modes comparison. The steel 1008 material is used for the CST model

to the enclosure modes, which produce standing waves. The level in-between the spikes represents a direct signal transfer between the split-probe configuration ($L_A L_C$) and L_B, which are evanescent signals in nature and do not lead to standing waves formation.

From the enclosure resonances perspective, it is also important to note that L_A and L_B see different cut-off frequencies due to their orientation. Because the signal always propagates within the loop surface direction [77], L_A creates a transverse magnetic (TM) and a transverse electric (TE) mode in the z axis ($\mathrm{TM}^{(z)}$ and $\mathrm{TE}^{(z)}$) while we have $\mathrm{TM}^{(x)}$ and $\mathrm{TE}^{(x)}$ for L_B. Figure 5.9 illustrates the enclosure orientation used for the above explanation. The cut-off frequencies for both propagations are expressed in (5.5) and (5.6) and the value for each frequency is calculated according to the enclosure dimension w, h and l.

$$L_A \begin{cases} F_{110} = \frac{1}{2\sqrt{\mu\epsilon}}\sqrt{\left(\frac{1}{w}\right)^2 + \left(\frac{1}{h}\right)^2} & \text{TM mode 480.23 MHz} \\ F_{101} = \frac{1}{2\sqrt{\mu\epsilon}}\sqrt{\left(\frac{1}{w}\right)^2 + \left(\frac{1}{l}\right)^2} & \text{TE mode 390.51 MHz} \end{cases} \tag{5.5}$$

$$L_C \begin{cases} F_{110} = \frac{1}{2\sqrt{\mu\epsilon}}\sqrt{\left(\frac{1}{l}\right)^2 + \left(\frac{1}{h}\right)^2} & \text{TM mode 450.69 MHz} \\ F_{101} = \frac{1}{2\sqrt{\mu\epsilon}}\sqrt{\left(\frac{1}{l}\right)^2 + \left(\frac{1}{w}\right)^2} & \text{TE mode 390.51 MHz} \end{cases} \tag{5.6}$$

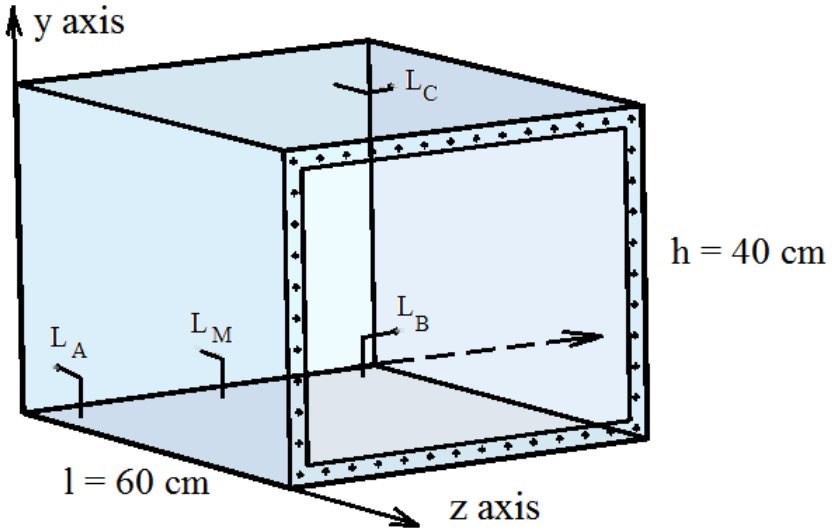

Figure 5.9: Enclosure orientation for a propagation in the z direction

The reason why the mode at 450.69 MHz, which is L_B second cut-off frequency, does not appear on the blue and the red curves is because L_B misses all the H-field lines parallel to its plane. The enclosure radiated signal measurement through the RC LPDA clearly shows that these modes are excited.

5.3.4 Best Loop Combination for Lowest Mode Coupling Improvement

Figure 5.8 also shows that the coupling increases with frequency. So, the TD metrology will certainly have a dynamic range issue at lower frequency since SE is also high for these frequencies. To enhance the lowest modes coupling, a fourth loop (called L_M) is placed at the bottom-centre of the face containing L_A (see figure 5.7.a). The new loop always picks the maximum H-field lines at this location for modes index m equal to one. It is however sitting on a null for all even m.

Analytically, the H-field expressions for propagation along the z direction is given by (5.7) and (5.8) for both TM and TE modes. If a fictitious field is generated within the enclosure, the ratio of the signals coupled through L_M and L_A is proportional to the ratio of the H-field at the loops location. By substituting the loops coordinates within the equations, which are: $L_M(\frac{w}{2},0,0)$ and $L_A(0.05,0,0)$, the expression in (5.9) gives a signal of 10.2 dB

higher at L_M for any m = 1.

$$\text{TM mode} \begin{cases} \tilde{H}_x = \dfrac{j2\omega\epsilon N}{M^2+N^2}\hat{E}_{zm}\, sin(Mx)cos(Ny)cos(Pz) & (5.7a) \\ \tilde{H}_y = -\dfrac{j2\omega\epsilon M}{M^2+N^2}\hat{E}_{zm}\, cos(Mx)sin(Ny)cos(Pz) & (5.7b) \\ \tilde{H}_z = 0 & (5.7c) \end{cases}$$

$$\text{TE mode} \begin{cases} \tilde{H}_x = j\dfrac{2MP}{M^2+N^2}\hat{H}_{zm}\, sin(Mx)cos(Ny)cos(Pz) & (5.8a) \\ \tilde{H}_y = j\dfrac{2NP}{M^2+N^2}\hat{H}_{zm}\, cos(Mx)sin(Ny)cos(Pz) & (5.8b) \\ \tilde{H}_z = -2\hat{H}_{zm}cos(Mx)cos(Ny)sin(Pz) & (5.8c) \end{cases}$$

where $M = \dfrac{m\pi}{w}$, $N = \dfrac{n\pi}{h}$ and $P = \dfrac{p\pi}{l}$ with m,n and p $\in \mathbb{N}$

$$d = 20\, log\left(\frac{|\vec{H}_{L_M}|}{|\vec{H}_{L_A}|}\right) \tag{5.9}$$

The 10 dB improvement is experimentally and computationally verified by exciting the enclosure through L_B. The S_{21} parameters between the loops $L_A - L_B$ and $L_M - L_B$ are shown in figure 5.10 for visual comparison. Here, the simulated curves in green and black match the measurements. The spike variation of 10 dB is observed and is indicated on the figure with the red circles. We can also identify a few modes which are present on the signal measured with L_A but are missing with L_M. These modes are marked with the white circle on top of the figure. These findings shows that L_M should be part of the split-probe configuration to boost the lowest mode.

For a second set of measurements, the enclosure is successively connected to six split-probe combinations and the signal radiated within the chamber is measured through the LPDA. The result of the investigation is given in figure 5.11. It shows that the three excitation configurations involving L_M give higher S_{21} curves, which are depicted by the plots with markers. This is especially the case at low frequencies. Almost the same level is however seen for all the modes at higher frequency for both split-probe excitation. These findings shows that L_M must be included in the split-probe configuration and the second loop can be either L_A or L_B.

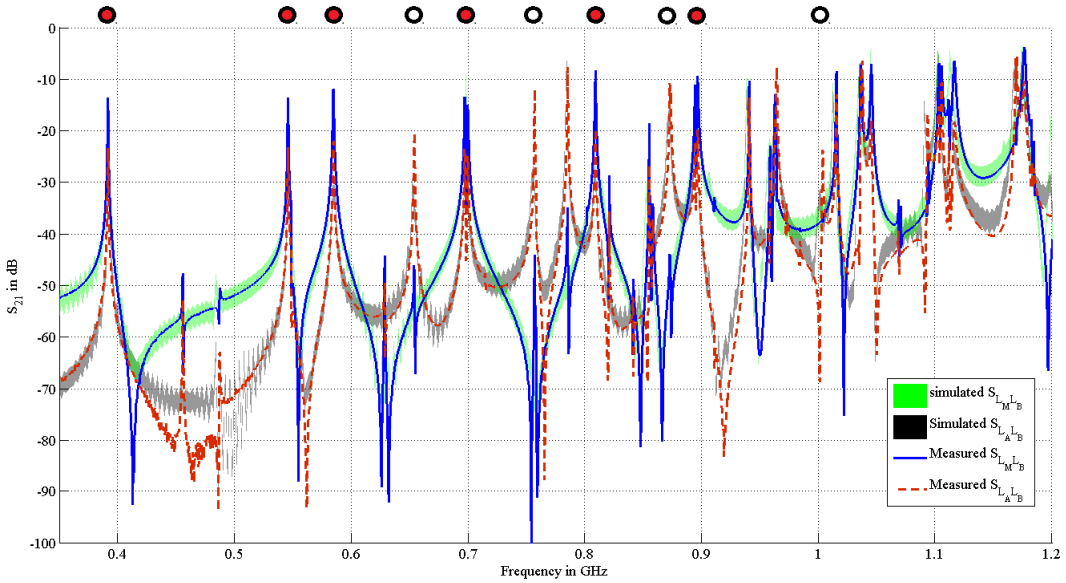

Figure 5.10: Measured S_{21} parameters for Loop C - Loop M and Loop C- L_A. Loop M and L_A are located on the enclosure face along x, L_A is located at 5 cm from the bottom-corner while Loop M is at the bottom-centre of the face

5.4 FD SE Investigation

5.4.1 SE Expression for the Split-Probe Arrangement

The enclosure transmitted power is slightly different from (5.3) for the split-probe configuration. The splitter adds an extra attenuation in the measurement chain and the loops mutual-coupling also shapes the signal. These effects must be corrected for a proper SE evaluation, and the split-probe-enclosure connection sketched in figure 5.12 is used to examine all the signals occurring in the split-probe system.

Generally, the signals collected at the splitter outputs (called P_a and P_b) are lower than the input. So, a reasonable way of compensating the splitter effect is the integration of its attenuation factor in the calculation. The split-probe diagram also shows that the total reflected signal at the splitter input-port comes from:

- the splitter port mismatch
- the loops connection mismatches
- the loops mutual-coupling path (represented by M_{BA} and M_{AB} in 5.12)
- the feed-back effect due to the loops coupling (depicted by F_b on the same figure).

In steady-state, the S_{11} data incorporates all of the split-probe internal interactions, the

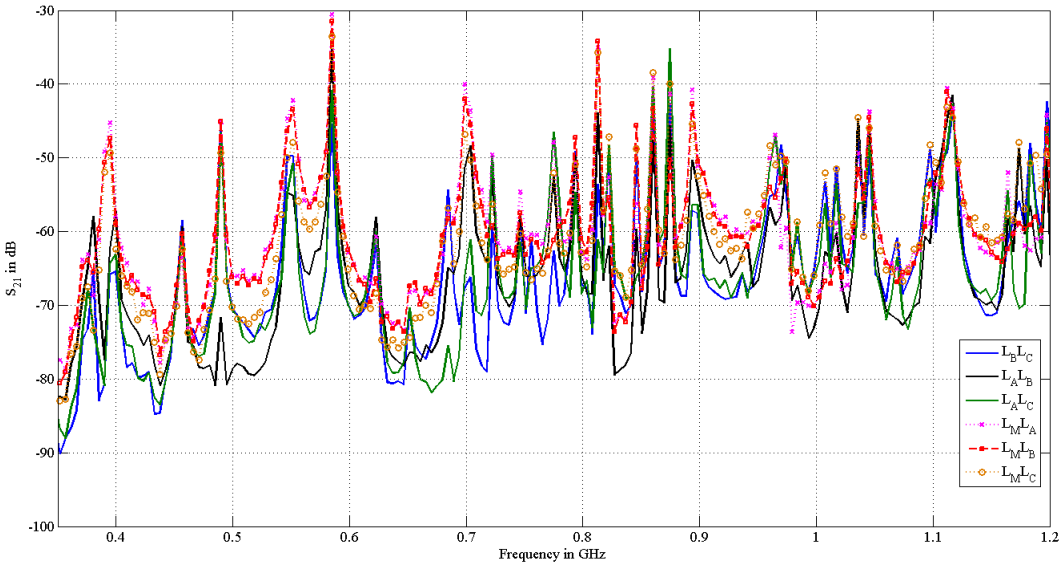

Figure 5.11: S_{21} parameters between the chamber LPDA and six split-probe configurations

term $1 - |S_{11\,Splitter}|^2$ is sufficient for the correction. Noting P_1 and P_2 the individual net powers transferred by the loops within the enclosure, we have:

$$P_{EUT} = P_1 + P_2 \tag{5.10a}$$

$$= P_{In}(L_{S1} + L_{S2})(1 - |S_{11\,Splitter}|^2) \tag{5.10b}$$

where P_a and P_b are the non-attenuated powers from the splitter. L_{S1} and L_{S2} represent the splitter loss factors for the two output channels.

By substituting both (5.10b) and (5.2) in (5.1), we get the SE expression for the split-probe configuration as follows:

$$SE = \frac{|S_{21}|^2}{(L_{S1} + L_{S2})(1 - |S_{11\,Splitter}|^2)(1 - |S_{11\,LPDA}|^2)\ \mathrm{CVF}\ \eta_{LPDa}} \tag{5.11}$$

5.4.2 SE Results for Few Split-Probe Configurations

Six SE measurements are performed using six split-probe combinations. The investigation permits the observation of the SE variation when the enclosure is excited in different ways. The EUT lid is properly tightened for the study and the device is left empty (not stirred) during the investigation. Figure 5.13 shows the computed SE results using the expression given in (5.11) where the blue and the red lines regroup respectively the result for split-probe arrangements with and without the centre loop L_M.

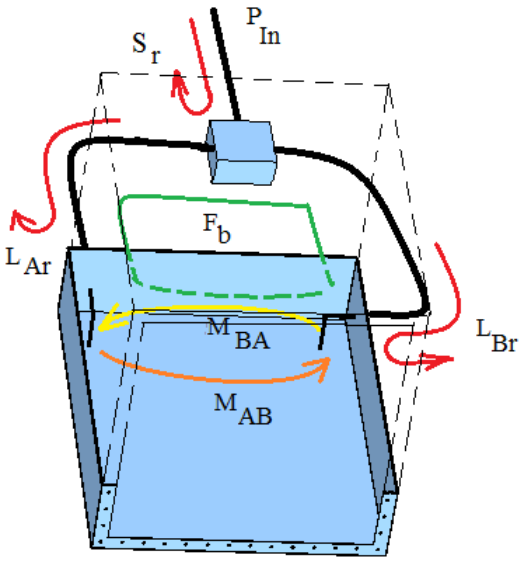

P_{In}	Input power
S_r	Splitter Input reflection
L_{Br}	Loop L_B reflection
L_{Ar}	Loop L_A reflection
F_b	Feedback path
M_{AB}	$L_A L_B$ mutual coupling
M_{BA}	$L_B L_A$ mutual coupling

Figure 5.12: Splitter-loop connection diagram for P_{EUT} characterisation

A similar pattern trend is observed between the curves and a difference of about 10 dB appears at low frequencies between the blue and the red plots. The variations generally happen for the evanescent signals in-between the spikes. The modes' responses are almost at the same SE level for most of the split-probe excitations. At higher frequency, however, the deviation between the blue and the red curves is less. Regarding the nature of the field within an RC and the way the RC fields are measured, a variation within ± 2.5 dB is expected for each mode, for a 90% confidence interval, as seen with the airline Z_t results in figure 4.24.

The curve variation for the evanescent signals is probably caused by the split-probe locations. The SE corresponding to these signal depends generally on the length of the direct-path between the enclosure excitation and the RC region. This distance is clearly different for one excitation to another because the EUT apertures are static. Figure 5.14 illustrates the principle more accurately where L_1 is expected to radiate more power through the hole H than L_2. However, similar P_{EUT} should be present inside the enclosure since L_1 and L_2 are symmetric. This leads to different SE values depending on the distance d.

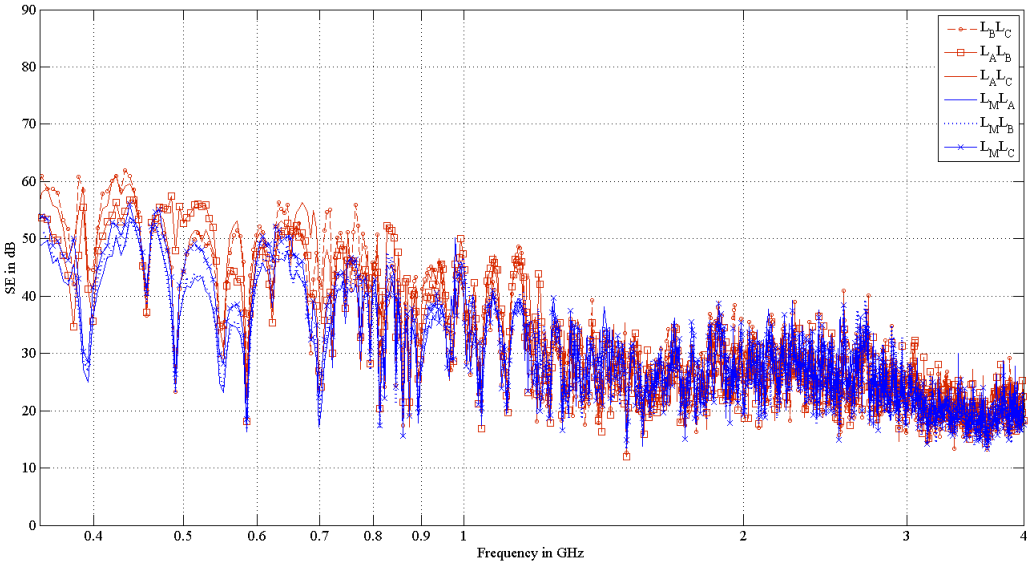

Figure 5.13: SE results for six split-configurations.

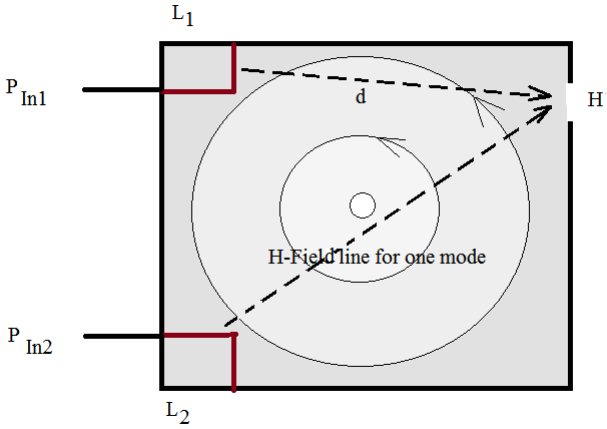

Figure 5.14: Direct path coupling variation regarding the probe location

5.4.3 SE Variation According to the Lid Configurations

For the next measurements set, the split probe L_ML_B is chosen for the EUT excitation. The two measurement scenarios are as follows:

- copper-tape is wrapped around the lid-enclosure contact area to minimize the radiation coming from the gasket connection,
- for the second, the lid is removed from the setup and a 10 cm dipole antenna is also used for feeding. The dipole is placed approximately at 20 cm away from the centre of the face containing L_M and L_A.

The SE corresponding to these lid configurations is presented in figure 5.15 where the green curve is taken from figure 5.13 for the purpose of comparison.

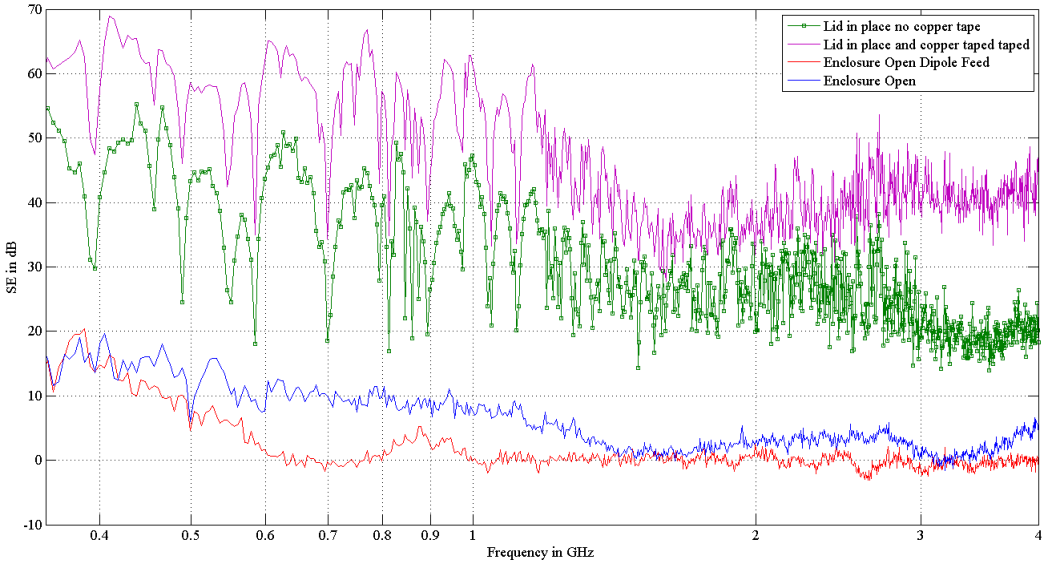

Figure 5.15: SE variation according to the lid configuration. EUT is excited by the $L_M L_C$ split-probe configuration

Figure 5.15 shows that the copper-tape improved SE by about 10 to 18 dB according to the difference between the green and the purple curves. The improvement is uniform for frequencies less than 1.2 GHz. It decreases slightly between 1.2 to 2.2 GHz. Then it re-increases up to approximately 18 dB for frequency more than 2.2 GHz. The EUT has no more shielding at the dipole location when the lid is absent. However, the region within 5 cm from the wall still provides an SE up to 1.5 GHz according to the blue curve. The level difference between the red and the blue plots over the frequency range shows the gradual variation of SE inside the EUT with position.

5.4.4 SE for a Stirred Enclosure

With the copper-tape in place and using the same excitation sources as before (the $L_M L_B$ split-probe and the dipole), the enclosure SE is re-characterised in the presence of the EUT stirrer ST2. The measurement is undertaken according to the setup given in figure 5.1 where ST2 rotates in continuous mode of 3 RPM. The synchronisation between the RC and the EUT stirrers has been described in section 5.1.1 but for simplicity and for finer frequency resolution, we set the VNA to a maximum-hold status during the time ST2 finishes two rotations. Two SE responses emerge from the investigation with the excitation used. Figure 5.16 depicts the dipole and the split-probe SE results in red and in green. Here, both curves are particularly smooth for frequencies higher than 1.3 GHz

and are very similar in terms of shape and level. This indicates the presence of a field uniformity region within the EUT, where ST2 is efficient and where the setup behaves as for a normal nested-enclosure measurement technique.

The SE for the non-stirred configuration (the curve in blue) also has the same pattern trend as the red and the green at this higher frequency region but, with more fluctuations due to the modes. Additionally, the SE for the stirred configuration coincides with the bottom peaks of the SE curve given by the unstirred enclosure. This particular behaviour is expected since the data for the red and the green curves were recorded with a maximum-hold setting during the measurement. So, almost the highest power transferred to the EUT is used in the SE calculation for the stirred enclosure. This result shows that the unstirred SE can be used to approximate the SE given by a normal nested-enclosure technique. Here, the agreement between the stirred and the non-stirred enclosure partially validates the split-probe methodology.

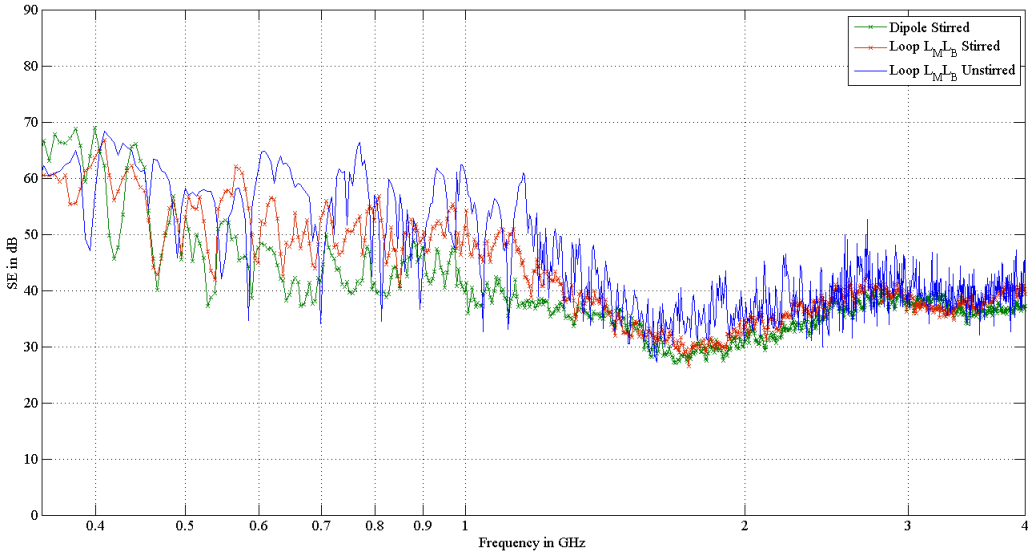

Figure 5.16: SE comparison between a stirred and a non-stirred enclosure

The dipole and the split-probe responses for the stirred environment are different between 600 MHz and 1,2 GHz and this is mainly caused by the stirrer inefficiency in the low frequency region. However, it should be noted that the stirrer gradually loses its efficiency when the frequency decreases. Thus, ST2 still has an effect on the dipole and the split-loop within this particular frequency range. As a result, the mode fluctuations are different at the dipole and the loops location. This introduces a variation between the maximum power obtained from the dipole and the split-loop configuration during the maximum-hold scanning period. From 600 MHz to 1,2 GHz, we believe the dipole gives the best SE approximation because it is closer to the tuner paddle and so it is exposed to a higher mode variation. Moreover, the green plot level and the blue curve spikes, the unstirred SE

signature, almost match over the all frequency range.

For a very low frequency, however, (less than 600 MHz) both curves converge towards an SE of 60 dB again. This means the stirrer rotation has no effect on the fields. Then, the system tends to a normal cavity resonator where the modes are static.

In a summary, we believe the similarity between the green curve level and the blue curve spikes validates the assumption given in (5.3) and raised in section 5.3.2. The agreement between the SE spikes corresponding to the six split-probe configuration in 5.12 also confirms that the empty cavity SE can be estimated within a non-stirred environment using a different excitation configuration. One must be sure though that the modes are excited.

5.4.5 Effect of the Splitter on SE

The internal schematic of a Mini-Circuits in-phase splitter [78] is given in figure 5.17. An analysis of the circuit shows that the internal resistance R_{Int} can influence the enclosure P_{EUT} by inserting an extra power-loss in the system if conditions are imbalanced. This variation is not considered in the SE calculation in (5.11). So, the SE results could overlook the splitter-loss due to R_{Int} under such circumstances.

From the figure, it can be demonstrated that no current appears in R_{Int} when the split-signals at PortA and PortB travel along equal path lengths and see near-identical excitation loop impedances. For the present work, two semi-rigid cables of approximately 48 cm fed the loops to minimise the contribution of R_{Int}.

As a recommendation, this situation can be avoided if the splitter is omitted and the two loops are individually fed. For this purpose, the same pulse generator can be used. A superposition principle can be applied for the SE calculation. The investigation will be longer than the slit-probe measurement, but splitter losses will be removed. Another approach could be the use of separate pulse generators triggered by the same source. Neither of these approaches have been implemented in this work.

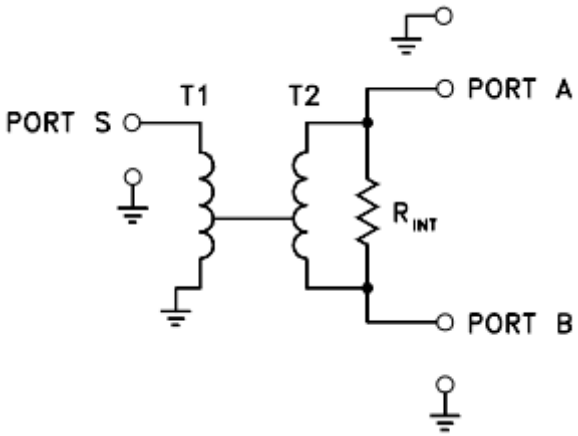

Figure 5.17: Internal schematic of an in-phase splitter according to Mini-Circuits [78]

5.5 TD SE Investigation

A TD version of the investigation is also examined using the split-probe $L_A L_B$. The obtained SE is compared with the previous FD approach using the probe $L_M L_B$ in figure 5.18. The work has been presented to the ICEAA conference in 2013 [53]. A summary is addressed in the following sections with recent updates concerning the topic.

5.5.1 Measurement Overview

The TD measurement setup conforms to the description given in section 5.1 where 72 ST1 steps were taken per revolution. For the enclosure P_{EUT} evaluation, however, only 40 samples are considered due to the ST2 lowest speed limitation of 3 RPM. RATTY and the pulse generator allow a TD SE investigation using a triggering signal with a 20 μs period. With six pulses per RATTY-record, 17280 reverberated pulses are obtained in total and averaged for the SE calculation.

5.5.2 TD and FD SE Results Comparison

The FD-curve in figure 5.18 is taken from figure 5.16 and is plotted in red. On the one hand, both SE patterns show good level correlation over the frequency range. On the other hand, there are specific differences indicated by the markers. The modal amplitude variations and the loading of the respective TD and FD generators for this splitter-loop configuration will be provide the explanation. Further work is required to isolate the

loop-loading effect on the generators (a 6 dB pad would held in this regard). Superposition or two generators would also contribute to resolving these specific differences.

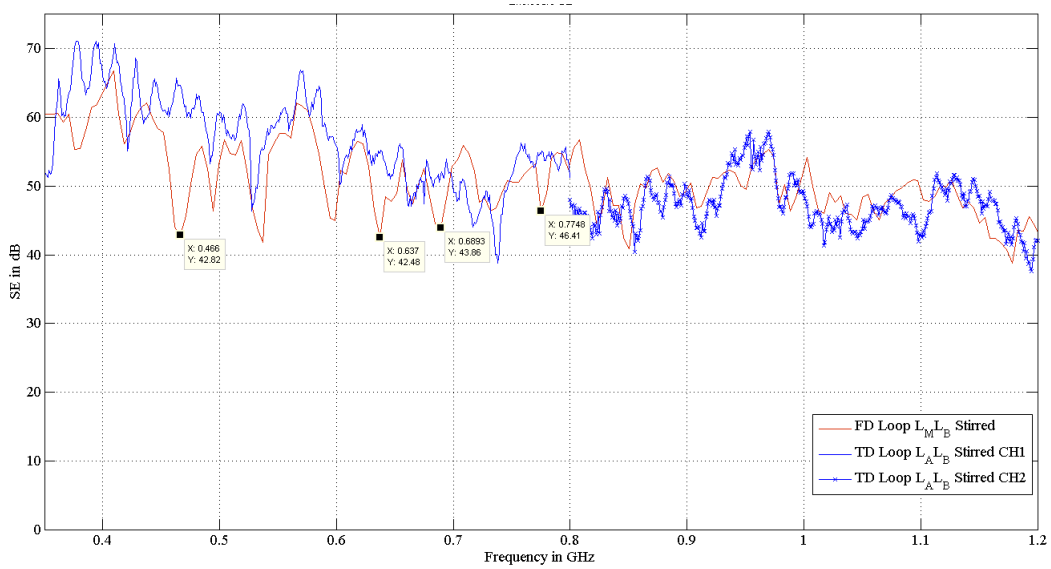

Figure 5.18: The EUT SE in TD and FD. The conventional nested-enclosure technique is used for both investigations. The split-loops $L_M L_B$ and $L_A L_B$ are respectively used to excite the EUT.

5.5.3 Comments on Measurement Time Speed-Up

The conventional FD shielding investigation takes 1.5 hours for 401 frequency points while the TD technique, which can yield 32768 frequency samples, reduces the measurement-time down to an hour. The TD investigation takes a third less time, but has a substantial resolution advantage. In equivalent terms, 122 hours are approximately necessary to observe the same details in the FD.

5.6 Summary

In summary, a static cavity modal analysis has been reviewed for a non-stirred metallic enclosure SE investigation. A split-probe setup based on a two-loop combination, located at the EUT corner, was used for feeding. As opposed to the conventional nested-enclosure technique, we injected the signal inside the enclosure under-test with the split-probe configuration. Afterwards, the radiation was measured through an LPDA antenna placed in the RC working volume. The EUT transferred power was computed according to the EUT input-port reflection for the SE calculation. The SE we obtained for the non-stirred EUT goes up to 4 GHz for the FD investigation and up to 1.2 GHZ for the TD

result. An SE agreement was seen between the FD SE results for six selected split-probe arrangements. The conventional nested-enclosure technique and the non-stirred enclosure setup particularly showed correlation in the region where the EUT stirrer is efficient. The present status of the work is that the non-stirred enclosure SE outcome is not validated with different methods. Further study would be valuable to check our findings. The split probe configuration is promising, but an SE investigation using the superposition of each loop excitation response is also recommended to avoid the splitter internal losses. The TD SE technique showed trend agreement with the FD approach as was seen for the coaxial airline SE investigation in chapter 4.

CHAPTER 6

Conclusion, Recommendations and Further Work

6.1 Conclusion and Recommendations

Unwanted EM coupling represents a major threat in high frequency application, especially for sensitive system such as the MeerKAT telescopes. It reduces the performance of equipment and often a shielding technique is necessary to keep the signal integrity. In general, we cannot cancel the EM noise coming from the surroundings. The creation of an interference-controlled environment by means of enclosures constitutes the most used approach for equipment protection. The recently built underground structure (KAPB), at the MeerKAT site, is an example of this technique, where the building controls the coupling between the on-ground telescopes and the devices within the building. Within KAPB, enclosures will be also used for internal interference mitigation. In this regard, the dissertation focusses on a small metallic enclosure SE characterisation.

For many reasons, such as the accuracy of modern VNAs and the dynamic range these devices can achieve, the FD investigation is an engineer's preferred methodology for high frequency system characterisation. However, it is a time-consuming procedure for a reverberated environment setup, such as the nested-enclosure technique. The nested-enclosure technique is particularly applied for small enclosure's SE. A TD version of the approach was considered in the dissertation for measurement speed-up and for SE characterisation of an under-moded enclosure. The work started with the review of

fundamental literature on SE in general. This included Bethe's theory of small hole coupling and Vance and Kley analytical models of coaxial cables. Apart from the background reviews, the dissertation was structured around the following three main parts:

- In the first part, chapter 3, our RC was re-analysed and was optimised for a better low-frequency response.
- The second part, chapter 4, presented the TD metrology, its characteristics and its validation though Z_t examination of an in-house rigid coaxial airline.
- Chapter 5 examined the small EUT SE. A non-stirred enclosure configuration was chosen for the SE measurement. It allowed an SE investigation of an under-moded enclosure related to our TD frequency band.

The chamber calibration parameters CVF and AVF represent the RC attenuation for both the empty and the loaded RC. Both parameters are investigated in a similar fashion to that as specified in the IEC 61000-4-21 [1] and are dependent on the antenna characteristic. Our RC calibration data was checked in chapter 3 before the TD application and the enclosure investigation were carried out. Within this work, we examined the impact of an incorrect antenna efficiency on AVF and CVF, where the IEC LPDA efficiency of 0.75 was taken as the reference. Our LPDA has been simulated with the computational code CST and the PCB FR-4 material was accounted for in the modelling. The physical LPDA efficiency was measured within the RC using a reference antenna, a 10 cm dipole, that we characterised with FEKO. Both the simulation and the measurement were in agreement and the efficiency value was different from 0.75. This study emphasised the importance of a correct antenna efficiency value for RC measurements. The low frequency region of AVF was the most affected by the findings.

The TD metrology incorporated a built-in pulse generator and the SKA receiver RATTY, which is a ROACH board-based instrument. Chapter 4 discussed the TD chain and its validation using an in-house coaxial airline as the reference tool. CST and FEKO simulations and theoretical models were used to predict the cable Z_t. These results were later compared with our RC measurements, in TD and FD, for validation. Good agreement has been particularly seen between TD and FD Z_t. Moreover, the measurements agree with both the computational and the theoretical prediction. The investigation also demonstrated the effect of the cable under-test length with Z_t where an oscillation was created within the Z_t curve over the range. The resonance was decreased in amplitude with frequency and was seen in both the simulations and the measurements. The resonance is an inevitable signature of the cable and it is not accounted for by the theoretical models.

From the enclosure SE perspective, a modified nested-enclosure technique was proposed

for the investigation and the SE definition from the IEEE standard in [2] was used. The proposed methodology deviated from the original nested-enclosure setup in the following ways:

- the enclosure is unstirred throughout the measurement
- the source is contained within the EUT rather than inside the RC
- the EUT total transmitted power, P_{EUT}, is evaluated from the input port reflection data for the SE computation.

The enclosure was considered as a normal radiator placed within an RC working volume. The EUT stirrer led to a measurement speed-up equal to the time for a normal RC application. The nested-enclosure setup modification accounted for the enclosure under-moded condition and gave an SE spectrum covering the EUT lowest cut-off mode up to 4 GHz. The enclosure excitation was particularly examined to make sure that the modes were created. A TD simulation, a theoretical field distribution and measurement were combined to find the suitable feeding configuration. A split-probe of two rectangular loops was chosen for the study using a commercial splitter. The comparison between the stirred and the non-stirred EUT were in agreement over the frequency range in terms of curve trend and level. However, the modified setup generated an SE which fluctuated due to static modes. For the normal nested-enclosure setup, the current TD metrology reduced the measurement time from 1.5 hours down to an hour with a substantially better SE resolution. The study shows that without the EUT stirrer, it is possible to estimate a small enclosure SE using the values relating to the modes and the total power radiated by the EUT.

The dissertation emphasises the importance of a correct antenna efficiency value for RC applications. It also shows the possibility of estimating an enclosure SE without the need for a stirrer. This approach leads to a measurement speed-up and also an SE value in the under-moded region of the EUT.

6.2 Further Work

The SE between the modified and the standard nested-enclosure technique gave similar SE results, as stated earlier, but the finding was not validated with simulations or other methodology. Thus, a further investigation would be valuable. The split-loop configuration is able to couple with the maximum modes within the enclosure. It does not, however, guarantee that an aperture is exposed to the highest radiation within the EUT. For the

present status of the work, the enclosure holes were located around the corners and this led to an agreement between the standard and the modified nested-enclosure setup. The holes should be spread in different areas, such as the centre of a face, to check if we still have similarities.

In comparison with the LPDA S_{11} within an RC, the coaxial airline was well-matched across the band and was not affected by the stirrer rotation. We believe an RC calibration based on coaxial airline will give a more accurate chamber response since it is independent of the chamber loading effect. However, the coaxial airline length should be shortened to shift the resonant frequency effect outside the RC range.

References

[1] IEC, "Electromagnetic compatibility (EMC) part 4-21: Testing and measurement-techniques reverberation chamber test methods," *IEC Std. 61000-4-21*, 2009. Draft version.

[2] IEEE, "IEEE standard method for measuring the shielding effectiveness of enclosures and boxes having all dimensions between 0.1 m and 2 m," *IEEE Std 299.1-2013*, pp. 1–96, Jan 2014.

[3] "An open invitation to the astronomical community to propose key project science with the south african square kilometre array precursor." http://www.ska.ac.za/temp/rfp_meerkat.pdf.

[4] N. Matthysen, "Time domain metrology for meerkat system," Master's thesis, University of Stellenbosch, December 2014. Thesis under review but will be available at https://scholar.sun.ac.za/.

[5] H. Pienaar, "Karoo array telescope site shielding: Laboratory, computational and multi-copter studies," Master's thesis, University of Stellenbosch, December 2014. Thesis under review but will be available at https://scholar.sun.ac.za/.

[6] J. C. Maxwell, "A dynamical theory of the electromagnetic field," *Philosophical Transactions of the Royal Society of London*, vol. 155, pp. 459–512, 1865.

[7] X. Tong, *Advanced Materials and Design for Electromagnetic Interference Shielding*. Taylor & Francis, 2008.

[8] D. Weston, *Electromagnetic Compatibility: Principles and Applications, Second Edition, Revised and Expanded*. Electrical and Computer Engineering, Taylor & Francis, 2001.

[9] T. Williams, *EMC for Product Designers*. EMC for Product Designers Series, Elsevier Science, 2011.

[10] F. M. Tesche, M. V. Ianozov, and T. Karlsson, *EMC Analysis Methods and Computational Models*. Wiley Interscience, 1997.

[11] C. Christopoulos, *Principles and Techniques of Electromagnetic Compatibility*. CRC Press, 1995.

[12] M. Badic and M.-J. Marinescu, "Reflection loss in the case of plane waves impact on infinite absorbing slab," in *IEEE International Symposium on Electromagnetic Compatibility*, vol. 2, pp. 626–629 vol.2, Aug 2003.

[13] B.-Z. Wang, "Small-hole formalism for the FDTD simulation of small-hole coupling," *Microwave and Guided Wave Letters, IEEE*, vol. 5, pp. 15–17, Jan 1995.

[14] H. Mendez, "Shielding theory of enclosures with apertures," *IEEE Transactions on Electromagnetic Compatibility*, vol. EMC-20, pp. 296–305, May 1978.

[15] S. de Santis, "Analysis of coupling impedance bench measurements using bethe's diffraction theory," in *Particle Accelerator Conference, 2001. PAC 2001. Proceedings of the 2001*, vol. 3, pp. 1844–1846 vol.3, 2001.

[16] H. A. Bethe, "Theory of diffraction by small holes," *Phys. Rev.*, vol. 66, pp. 163–182, Oct 1944.

[17] O. Kwon, S. H. Pak, J. K. So, I. Baik, S. H. Min, and G. Park, "Experimental confirmation of bethe's diffraction theory," in *36th International Conference on Infrared, Millimeter and Terahertz Waves (IRMMW-THz)*, pp. 1–2, Oct 2011.

[18] S. S. Kurennoy, "On the coupling impedance of a hole or a slot," 1991. CERN SL 91/29 (AP) Rev.

[19] M. Robinson, J. D. Turner, D. Thomas, J. Dawson, M. D. Ganley, A. Marvin, S. Porter, T. Benson, and C. Christopoulos, "Shielding effectiveness of a rectangular enclosure with a rectangular aperture," *Electronics Letters*, vol. 32, pp. 1559–1560, Aug 1996.

[20] G. Chunhong and L. Shufang, "Shielding effectiveness of an enclosure with apertures," in *IEEE International Symposium on Microwave, Antenna, Propagation and EMC Technologies for Wireless Communications*, vol. 1, pp. 614–618 Vol. 1, Aug 2005.

[21] K. Gupta, *Microstrip Lines and Slotlines 2nd Ed.* Artech House Antennas and Propagation Library, Artech House, Incorporated, 1996. Ch 7.

[22] M. Robinson, T. Benson, C. Christopoulos, J. Dawson, M. D. Ganley, A. Marvin, S. Porter, and D. Thomas, "Analytical formulation for the shielding effectiveness of enclosures with apertures," *IEEE Transactions on Electromagnetic Compatibility*, vol. 40, pp. 240–248, Aug 1998.

[23] B. S. Guru and H. R. Hiziruglu, *Electromagnetic Field Theory Fundamentals*. Cambridge University Press, 2nd ed., 2004.

[24] B. Szentkuti, "Shielding quality of cables and connectors: some basics for beller understanding of test methods," in *IEEE International Symposium on Electromagnetic Compatibility*, pp. 294–301, Aug. 1992.

[25] F. van Horck, A. van Deursen, P. van der Laan, P. Bruins, and B. Paagmans, "A rapid method for measuring the transfer impedance of connectors," *IEEE Transactions on Electromagnetic Compatibility*, vol. 40, pp. 193–200, Aug 1998.

[26] K. Casey and E. Vance, "EMP coupling through cable shields," *IEEE Transactions on Electromagnetic Compatibility*, vol. EMC-20, pp. 100–106, Feb. 1978.

[27] E. Vance, "Shielding effectiveness of braided-wire shields," *IEEE Transactions on Electromagnetic Compatibility*, vol. EMC-17, pp. 71–77, May 1975.

[28] R. Otin, J. Verpoorte, and H. Schippers, "Finite element model for the computation of the transfer impedance of cable shields," *Electromagnetic Compatibility, IEEE Transactions on*, vol. 53, pp. 950–958, Nov 2011.

[29] T. Kley, "Optimized single-braided cable shields," *Electromagnetic Compatibility, IEEE Transactions on*, vol. 35, pp. 1–9, Feb 1993.

[30] IEC, "Cable assemblies, cables, connectors and passive microwave components - screening attenuation measurement by the reverberation chamber method," *IEC Std. 61726*, 1999.

[31] L. O. Hoeft, "A simplifed relationship between surface transfer impedance and mode stirred chamber shielding effectiveness of cables and connectors," in *International Symposium on Electromagnetic Compatibility Europe*, pp. 441–446, Sep. 2002.

[32] B. Eicher and L. Boillot, "Very low frequency to 40 ghz screening measurements on cables and connectors; line injection method and mode stirred chamber," in *International Symposium on Electromagnetic Compatibility*, pp. 302–307, Aug 1992.

[33] D. M. Pozar, *Microwave Engineering*. John Wiley, 3rd ed., 2005.

[34] D. A. Hill, *Electromagnetic Theory of Reverberation Chambers*, vol. 1506 of *NIST TN*. 1998.

[35] J. Kostas and B. Boverie, "Statistical model for a mode-stirred chamber," *IEEE Transactions on Electromagnetic Compatibility*, vol. 33, pp. 366–370, Nov. 1991.

[36] M. T. Ma, "Understanding reverberating chambers as an alternative facility for EMC testing," *Journal of electromagnetic waves and applications*, vol. 2, no. 3/4, pp. 339–351, 1988.

[37] D. Hill, "Plane wave integral representation for fields in reverberation chambers," *IEEE Transactions on Electromagnetic Compatibility*, vol. 40, pp. 209–217, Aug. 1998.

[38] H. Naus, "Statistical electromagnetics: complex cavities," *IEEE Transactions on Electromagnetic Compatibility*, vol. 50, pp. 316–324, May 2008.

[39] J. M. Ladbury, G. H. Koepke, and D. G. Camell, *Evaluation of the NASA Langley Mode-Stirred Facility Ladbury*. 1999. Tech. Note 1508, ftp://ftp.boulder.nist.gov/pub/remley/Reverb

[40] J. A. Andriambeloson, "Wideband coaxial cable transfer impedance for karroo array telescope," Master's thesis, University of Stellenbosch, Dec 2011. http://hdl.handle.net/10019.1/18066.

[41] T. Aurand, J. Dawson, A. Marvin, and M. Robinson, "Reverberation chamber calibration: Differences in results when using a slot instead of a dipole antenna," in *IEEE International Symposium on Electromagnetic Compatibility*, pp. 1–4, Jul. 2007.

[42] Y. J. Wang and W. J. Koh, "Coupling cross section and shielding effectiveness measurements on a coaxial cable by both mode-tuned reverberation chamber and gtem cell methodologies," *Progress In Electromagnetics Research*, vol. 47, pp. 61–73, 2004.

[43] M. Herlemann, H. Koch, "Measurement of the transient shielding effectiveness of shielding cabinets," *Advances in radio science*, vol. 6, pp. 293–298, 2008.

[44] M. Crawford and J. Ladbury, "Mode-stirred chamber for measuring shielding effectiveness of cables and connectors: An assessment of mil-std-1344a method 3008," in

IEEE International Symposium on Electromagnetic Compatibility, pp. 30–36, Aug. 1988.

[45] C. Holloway, D. Hill, J. Ladbury, G. Koepke, and R. Garzia, "Shielding effectiveness measurements of materials using nested reverberation chambers," *IEEE Transactions on Electromagnetic Compatibility*, vol. 45, pp. 350–356, May 2003.

[46] C. Holloway, D. Hill, M. Sandroni, J. Ladbury, J. Coder, G. Koepke, A. Marvin, and Y. He, "Use of reverberation chambers to determine the shielding effectiveness of physically small, electrically large enclosures and cavities," *IEEE Transactions on Electromagnetic Compatibility*, vol. 50, pp. 770–782, Nov 2008.

[47] G. Tait, C. Hager, M. Slocum, and M. Hatfield, "On measuring shielding effectiveness of sparsely moded enclosures in a reverberation chamber," *IEEE Transactions on Electromagnetic Compatibility*, vol. 55, pp. 231–240, April 2013.

[48] Q. Wang, E. Cheng, and Z. Qu, "On the shielding effectiveness of small-dimension enclosures using a reverberation chamber," *IEEE Transactions on Electromagnetic Compatibility*, vol. 53, pp. 562–569, Aug 2011.

[49] P. van der Merwe, *Cabling and Interfaces for Karoo Array Telescopes: Modelling and Metrology*. PhD thesis, Stellenbosch University, 2011.

[50] M. Hatfield, "Shielding effectiveness measurements using mode-stirred chambers: a comparison of two approaches," *IEEE Transactions on Electromagnetic Compatibility*, vol. 30, pp. 229–238, Aug 1988.

[51] T. Loughry and S. Gurbaxani, "The effects of intrinsic test fixture isolation on material shielding effectiveness measurements using nested mode-stirred chambers," *IEEE Transactions on Electromagnetic Compatibility*, vol. 37, pp. 449–452, Aug 1995.

[52] J. A. Andriambeloson, H. Reader, P. Wiid, and A. R. Botha, "Reverberation chamber and current injection cable system study in frequency and time domains," in *International Conference on Electromagnetics in Advanced Applications (ICEAA)*, pp. 686–689, Sept 2012.

[53] J. Andriambeloson, H. Reader, and A. Botha, "Time-domain nested-enclosure technique for shielding effectiveness characterisation," in *International Conference on Electromagnetics in Advanced Applications (ICEAA)*, pp. 901–904, Sept 2013.

[54] S. Evans and H. C. Reader, "An impulse generator for antenna measurements in the time domain," *Journal Phys. E: Sci. Instrum*, vol. 21, pp. 657–660, 1988.

[55] B. A, "Development of a real-time transient analyser for the ska," Master's thesis, 2014. http://hdl.handle.net/10019.1/86462.

[56] C. Holloway, J. Ladbury, J. Coder, G. Koepke, and D. Hill, "Measuring the shielding effectiveness of small enclosures/cavities with a reverberation chamber," in *Electromagnetic Compatibility, 2007. EMC 2007. IEEE International Symposium on*, pp. 1–5, July 2007.

[57] Y. He and A. Marvin, "Aspects of field statistics inside nested frequency-stirred reverberation chambers," in *IEEE International Symposium on Electromagnetic Compatibility*, pp. 171–176, Aug 2009.

[58] C. Lemoine, P. Besnier, and M. Drissi, "Advanced method for estimating number of independent samples available with stirrer in reverberation chamber," *Electronics Letters*, vol. 43, pp. 861–862, Feb. 2007.

[59] C. Lemoine, P. Besnier, and M. Drissi, "Estimating the effective sample size to select independent measurements in a reverberation chamber," *IEEE Transactions on Electromagnetic Compatibility*, vol. 50, no. 2, 2008.

[60] C. Tsigros, M. Piette, G. Vandenbosch, and D. Van Troyen, "Antenna efficiency determination in a reverberation chamber: From the relative to the e-field method," in *EMC Europe 2011 York*, pp. 164–169, Sept 2011.

[61] Azremi, "A study and investigation of small antenna efficiency measurement using reverberation chamber," *Journal of Engineering Reasearch and Education*, vol. Vol 3, pp. 129–138, 2006.

[62] C. Balanis, *Antenna Theory: Analysis and Design*. Wiley, 2012.

[63] C. Holloway, H. Shah, R. Pirkl, W. Young, D. Hill, and J. Ladbury, "Reverberation chamber techniques for determining the radiation and total efficiency of antennas," *IEEE Transactions on Antennas and Propagation*, vol. 60, pp. 1758–1770, April 2012.

[64] H. Wheeler, "The radiansphere around a small antenna," *Proceedings of the IRE*, vol. 47, pp. 1325–1331, Aug 1959.

[65] P. Karstadt and A. Gupta, "Radiation efficiency measurement of communication antennas with wheeler cap method," in *International Students and Young Scientists Workshop*, pp. 64–67, July 2011.

[66] W. McKinzie, "A modified wheeler cap method for measuring antenna efficiency," in *Antennas and Propagation Society International Symposium*, vol. 1, pp. 542–545 vol.1, July 1997.

[67] A. A. H. Azremi, H. Ghafouri Shiraz, and P. Hall, "Reverberation chamber for efficiency measurement of small antennas," in *1st International Conference on Computers, Communications, Signal Processing with Special Track on Biomedical Engineering*, pp. 25–29, Nov 2005.

[68] D. Hill, M. Ma, A. Ondrejka, B. Riddle, M. Crawford, and R. Johnk, "Aperture excitation of electrically large, lossy cavities," *IEEE Transactions on Electromagnetic Compatibility*, vol. 36, pp. 169–178, Aug 1994.

[69] C. L. Bennett and G. Ross, "Time-domain electromagnetics and its applications," *Proceedings of the IEEE*, vol. 66, pp. 299–318, March 1978.

[70] A. Botha, H. Reader, J. Manley, S. Malan, H. Kriel, P. van der Merwe, P. Meyer, P. van der Walt, W. Croukamp, and R. Anderson, "Dynamic rfi measurement systems on a roach-2 platform iceaa-ieee apwc-ems," in *International Conference on Electromagnetics in Advanced Applications (ICEAA)*, pp. 502–505, Sept 2013.

[71] X. Chen, "On independent platform sample number for reverberation chamber measurements," *IEEE Transactions on Electromagnetic Compatibility*, vol. 54, pp. 1306–1309, Dec 2012.

[72] X. Chen, "Experimental investigation of the number of independent samples and the measurement uncertainty in a reverberation chamber," *IEEE Transactions on Electromagnetic Compatibility*, vol. 55, pp. 816–824, Oct 2013.

[73] K. Remley, R. Pirkl, H. Shah, and C.-M. Wang, "Uncertainty from choice of mode-stirring technique in reverberation-chamber measurements," *IEEE Transactions on Electromagnetic Compatibility*, vol. 55, pp. 1022–1030, Dec 2013.

[74] K. Madsen, P. Hallbjorner, and C. Orlenius, "Models for the number of independent samples in reverberation chamber measurements with mechanical, frequency, and combined stirring," *Antennas and Wireless Propagation Letters, IEEE*, vol. 3, pp. 48–51, Dec. 2004.

[75] O. Lundén and M. Bäckström, "Stirrer efficiency in FOA reverberation chambers. Evaluation of correlation coefficients and chi-squared tests," in *IEEE International Symposiumon Electromagnetic Compatibility*, vol. 1, pp. 11–16, 2000.

[76] J. Coder, J. Ladbury, and C. Holloway, "Using nested reverberation chambers to determine the shielding effectiveness of a material: Getting back to the basics with a "lei"-person's approach," in *IEEE International Symposium on Electromagnetic Compatibility*, pp. 1–6, July 2007.

[77] U. Bakshi and A. Bakshi, *Antenna And Wave Propagation*. Technical Publications, 2009.

[78] Mini-Circuits, *Understanding Power Splitters -Application note AN10006*. 2005. http://www.minicircuits.com/app/AN10-006.pdf.

Appendices

APPENDIX A

Pulse Generator Description

The pulse generators used within the dissertation, referred as PG1 and PG2, are built around an avalanche transistor and a step-recovery diode. Figure A.1 shows the pulse generators and in the table are given the main characteristics of each circuit.

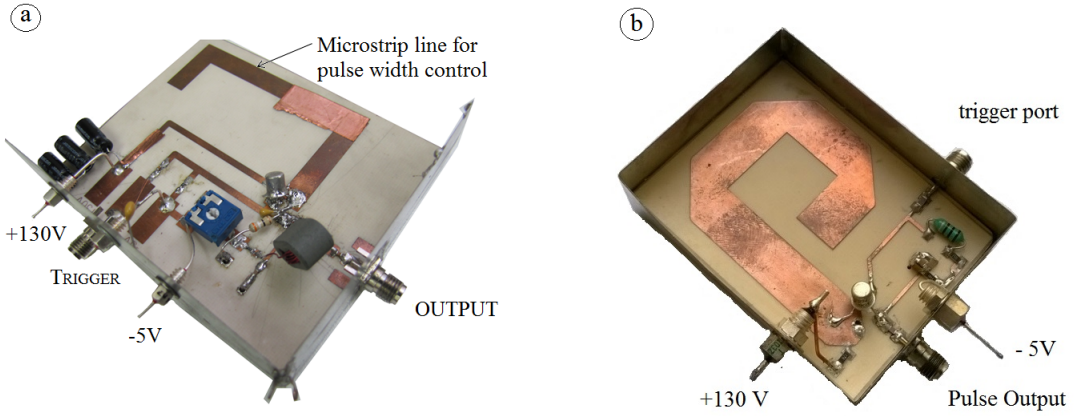

Figure A.1: The pulse generators used throughout the dissertation. (a) and (b) respectively shows PG1 and PG2

Table A.1: Main characteristic of each pulse generator

	PG1	PG2
Transistor	2N2369A	2N2369A
SRD	MMD810-T86	MMD820-T86
Voltage Output	27 V	27 V

APPENDIX B

MATLAB Program Listing

B.1 Kley's Model

```
%-------------------------------------------------------------------------
%
%                COAXIAL AIRLINE MODEL ACCORDING TO KLEY
%
%-------------------------------------------------------------------------

clear all;
close all;
clc;

%-------------------------------------------------------------------------
%                     THEORETICAL TRANSFER IMPEDANCE
%-------------------------------------------------------------------------
% Radius of the air-line
% (a : inner radius | b : outer radius)
%-----------------------------------------
a = (13.7e-3)/2;
b = (15e-3)/2;
Inner_radius_tube = a;


% Cable length
%--------------
L_CBL = 0.764;
```

```
% Radius of the hole
%————————————————
Radius_hole = (5e-3)/2;

Z1 = 50;
Z2 = 377;

% Thickness D of the sheath
%————————————————————————
D = b - a;
Thickness_tube = D;

% Permeability u
%————————————————
u0 = 4*pi*1e-7;

F = [200e6:0.1e6:4e9];

% Conductivity of a copper
%————————————————————————
sigma = 5.96e+7;     %IACS at 20 deg C

% Permeability u
%————————————————
u0 = 4*pi*1e-7;
ur = 1;
u = u0*ur;

%%                      SKIN DEPTH EFFECT
%————————————————————————————————————————————————————————————————————————
% Skin depth
skin = 1./sqrt(pi*F*u*sigma);

% DC Resistance
M = (1+1i)*Thickness_tube./skin;
Rdc = 1/(2*pi*sigma*Inner_radius_tube*Thickness_tube);

% Zt of the tubular shield
Zt_DC = Rdc.*M./sinh(M);


%%                  COUPLING THROUGH APERTURE (circular hole)
%————————————————————————————————————————————————————————————————————————

% Kley's model parameter (R_Shield represents the shield mean radius)
R_Shield = Inner_radius_tube + Thickness_tube/2;

MLL = (0.875*u0*Radius_hole.^3/(3*(pi*R_Shield)^2))*exp(-1.84*Thickness_tube/Radius_hole);
LSL = (Thickness_tube*Radius_hole/(2*(R_Shield)^2))*exp(-2.30*Thickness_tube/Radius_hole)*sqrt(u./(2*sigma*2.*

Zt_Hole = j*2*pi.*F.*MLL + (1+j)*2*pi.*F.*LSL;

%%                  TRANSFER IMPEDANCE OF THE AIR-LINE
%————————————————————————————————————————————————————————————————————————
N = 20/L_CBL;
Zt = N.*(Zt_DC + Zt_Hole);
```

```
figure;
semilogx(F,20*log10(abs(Zt)));
grid on;
grid on;
xlabel('Frequency in Hz');
ylabel('Transfer impedance in dB\Omega/m')
```

B.2 Vance's Model

```
%function [Zt] = Zt_theory(F,Radius_hole,Inner_radius_tube,Thickness_tube,Length_tube,sigma)

clear all;
close all;
clc;

%--------------------------------------------------------------------------
%                    THEORETICAL TRANSFER IMPEDANCE
%--------------------------------------------------------------------------
% Radius of the air-line
% (a : inner radius | b : outer radius)
%-----------------------------------------
a = (13.7e-3)/2;
b = (15e-3)/2;
Inner_radius_tube = a;


% Cable length
%--------------
L_CBL = 0.764;

% Radius of the hole
%--------------------
Radius_hole = (5e-3)/2;

Z1 = 50;
Z2 = 377;

% Thickness D of the sheath
%---------------------------
D = b - a;
Thickness_tube = D;

% Permeability u
%---------------
u0 = 4*pi*1e-7;

F = [200e6:0.1e6:4e9];

% Conductivity of a copper
%-------------------------
sigma = 5.96e+7;      %IACS at 20 deg C
```

```
% Permeability u
%----------------
u0 = 4*pi*1e-7;
ur = 1;
u = u0*ur;

%%                      SKIN DEPTH EFFECT
%-------------------------------------------------------------------------
% Skin depth
skin = 1./sqrt(pi*F*u*sigma);

% DC Resistance
M = (1+i)*Thickness_tube./skin;
Rdc = 1/(2*pi*sigma*Inner_radius_tube*Thickness_tube);

% Zt of the tubular shield
Zt_DC = Rdc.*M./sinh(M);

%%                  COUPLING THROUGH APERTURE (circular hole)
%-------------------------------------------------------------------------
% M12 = u0*alpha_eff/(pi*D)^2   D = diameter of the shield
% with alpha_eff = 3/2 alpham
% alpham = 4/3*radius_hole^3;
%-------------------------------------------------------------------------

% mutual inductance using alpha_m_eff
%-------------------------------------
D_Shield = 2*(Inner_radius_tube + Thickness_tube);

M12 = 2*u0*Radius_hole.^3/(pi*D_Shield)^2;

Zt_Hole = M12*2*pi*F;

%%                  TRANSFER IMPEDANCE OF THE AIR-LINE
%-------------------------------------------------------------------------
N = 20/L_CBL;
Zt = abs(Zt_DC) + i*Zt_Hole;

figure;
semilogx(F, 20*log10(abs(N*Zt)));
grid on;
xlabel('Frequency in Hz');
ylabel('Transfer impedance in dB\Omega/m')
```

B.3 LPDA Efficiency Computation

```
%-------------------------------------------------------------------------
%
%                          LPDA ANTENNA EFFICIENCY
%
%-------------------------------------------------------------------------
```

```
clc;
close all;
clear all;

Freq = [200e6:1e6:4e9];

%%
%.....................................................................
%                              FEKO SIMULATION
%.....................................................................
FEKO   = importdata('data\Dipole_Eff_FEKO.csv','\t');
FEKO_F = FEKO(:,1);
FEKO_Eff = interp1(FEKO_F,FEKO(:,2),Freq);


%%
%.....................................................................
%                        MEASUREMENT DATA
%.....................................................................
D2K     = load('data\Dipole_Only\Dipole2Airline.mat');
K2K     = load('data\Dipole_Only\LPDA2Airline.mat');

%figure;
for m = 1:8
    varname = ['Position' num2str(m)];
    varname = genvarname(varname);
    D2K_Tmp   = Sparam_per_Angle(D2K.(varname),72);
    K2K_Tmp   = Sparam_per_Angle(K2K.(varname),72);

    D2K.S11Avg(:,m) = interp1(D2K_Tmp.F,D2K_Tmp.S11_Avg,Freq);
    D2K.S22Avg(:,m) = interp1(D2K_Tmp.F,D2K_Tmp.S22_Avg,Freq);
    D2K.S21Avg(:,m) = interp1(D2K_Tmp.F,D2K_Tmp.S21_Avg,Freq);

    K2K.S11Avg(:,m) = interp1(K2K_Tmp.F,K2K_Tmp.S11_Avg,Freq);
    K2K.S22Avg(:,m) = interp1(K2K_Tmp.F,K2K_Tmp.S22_Avg,Freq);
    K2K.S21Avg(:,m) = interp1(K2K_Tmp.F,K2K_Tmp.S21_Avg,Freq);
end


%%
%.....................................................................
%                          KLPDA ANTENNA EFFICIENCY
%.....................................................................

for m = 1:8
    Dipole_Term    = ((1 - D2K.S11Avg(:,m).^2).*(1 - D2K.S22Avg(:,m).^2))./D2K.S21Avg(:,m).^2;
    LPDA_Term      = K2K.S21Avg(:,m).^2./((1 - K2K.S11Avg(:,m).^2).*(1 - K2K.S22Avg(:,m).^2));
    n_KLPDA4(:,m)  = smooth(Eff_Cone'.*LPDA_Term.*Dipole_Term,45);

    Tot_LPDA_Term      = K2K.S21Avg(:,m).^2./(1 - K2K.S11Avg(:,m).^2);
    Tot_n_KLPDA4(:,m)  = smooth(FEKO_Eff'.*Tot_LPDA_Term.*Dipole_Term,45);
end

% Mean Efficiency
n_KLPDA4_Mean     = mean(n_KLPDA4');
Tot_n_KLPDA4_Mean = mean(Tot_n_KLPDA4')
```

```
S11_KLPDA4_Mean    = smooth(mean(K2K.S11Avg'),15);

Std_Error          = std(n_KLPDA4);

figure(1);
h1 = plot(Freq*1e-9,n_KLPDA4_Mean,'r','linewidth',2);
xlabel('Frequency in GHz');
ylabel('Radiation Efficiency');
title('KLPDA4 Efficiency (source KLPDA2)');
legend(h1,'KLPDA4 Mean efficiency');

figure(2);
h1 = plot(Freq*1e-9,Tot_n_KLPDA4_Mean,'r','linewidth',2);
grid on;
hold on
xlabel('Frequency in GHz');
ylabel('Total Efficiency');
title('KLPDA4 Total  Efficiency (source KLPDA2)');
legend(h1,'KLPDA4 Mean Total efficiency');

figure(3);
h1 = plot(Freq*1e-9,20*log10(S11_KLPDA4_Mean),'r','linewidth',2);
xlabel('Frequency in GHz');
ylabel('S11 in dB');
title('KLPDA4 REflection (source KLPDA2)');
legend(h1,'KLPDA4 Mean S11');

%%
%.....................................................................
%                              EXPORT RESULTS
%.....................................................................

Data = [Freq' n_KLPDA4_Mean'];
csvwrite('KLPDA4_Eff_dipoleonly.csv',Data);

Data = [Freq' Tot_n_KLPDA4_Mean'];
csvwrite('KLPDA4_TotEff_dipoleonly.csv',Data);
```

B.4 Coaxial Air-line Z_T

```
%=====================================================================
%
%   SHIELDING EFFECTIVENESS INVESTIGATION USING A REVERBERATION CHAMBER
%
%=====================================================================
% Frequency range : 300MHz - 1300MHz
%-----------------
% Input power     : 25 dBm
% Measurement BandWidth : 100 Hz
%=====================================================================
close all;
clear all;
clc;
```

```
%% Initialisation
%------------------
% LPDA efficiency
Ant_eff = 0.75;

% Length of the air-line
L_CBL = 1.304;

%% USER Prompt
%---------------------
filename = input('Enter the file name : ','s');

%% Load the chamber's parameters and the Current Probe Zt
%-------------------------------------------------------------
% Antenna calibration factor obtained for RC calibration
IL  = importdata('data\IL_efficiency_0,75.csv');

% Transfer impedance of the current probe (EMCO 50999) in dBOhm
%-------------------------------------------------------------
EMCO = importdata('data\EMCO_Probe_Zt.csv');

% measurement's data filename (from the RC)
file1 = strcat(filename,'_HF.s2p');
file1 = strcat('Measurement\',file1);
% measurement's data filename (from the field to wire method)
file2 = strcat(filename,'_LF.s3p');
file2 = strcat('Measurement\',file2);

% LOAD DATA
%-------------
[S11_CBL,S11max_CBL,S21_CBL,S21max_CBL,S12_CBL,S12max_CBL,S22_CBL,S22max_CBL,F_HF] = ZVBSegFRead(file1,72);
[F_LF,S11_C,S12_C,S13_C,S21_C,S22_C,S23_C,S31_C,S32_C,S33_C] = ZVBRead_s3p(file2);

%% ========================================================================
%                       HIGH FREQUENCY PART OF ZT
%=========================================================================
% Resampling IL
%---------------
IL_F     = IL(:,1);
IL_Data  = IL(:,2);
IL       = interp1(IL_F,IL_Data,F_HF);

% Mismatches evaluation
%-----------------------
% antenna input
Ant_mis_CBL  = 1 - S22max_CBL.^2;

% Mismatches at the input of the cable
CBL_Mis  = 1 - S11max_CBL.^2;

%%  SHIELDING EFECTIVENESS CALCULATION
%-------------------------------------
% Corrected Shielding effectiveness of the cable
%-----------------------------------------------
SE_CBL = S21max_CBL.^2./(Ant_eff.*Ant_mis_CBL.*CBL_Mis.*IL);
```

```
%% HF TRANSFER IMPEDANCE
%————————————————————
% Boilot and Eicher Foramulation
Z1 = 50;
Z2 = 377;
Zt_HF  = sqrt(2*Z1*Z2*SE_CBL);

%% ========================================================================
%                       LOW FREQUENCY PART OF ZT
%=========================================================================

% Resampling The EMCO Zt
%————————————————————
EMCO_F      = EMCO(:,1);
EMCO_Ztt_dB = EMCO(:,2);
EMCO_Ztt    = 10.^(EMCO_Ztt_dB/20);
Ztt         = interp1(EMCO_F,EMCO_Ztt,F_LF);

% CORRECTION FACTOR
%————————————————————
er = 2.25;
lambda_0 = 3e8./F_LF;
B0 = 2*pi./lambda_0;
C = cos(sqrt(er)*B0*L_CBL) - cos(B0*L_CBL);
S = sqrt(er).*B0.*sin(sqrt(er).*B0.*L_CBL) - B0.*sin(B0.*L_CBL);

N = (sqrt(er)*B0).^2 - B0.^2;
M = sqrt(er*(B0.^2).*(C.^2) + S.^2);

CF = N./M;

% TRANSFER IMPEDANCE OF THE CABLE
%————————————————————————————
Zt_C = 4*Ztt.*abs(S21_C).*CF./abs(S31_C);

% Resonant frequency
%————————————————————
F_res = 3e8/(L_CBL*4);
F_step   = (F_res - F_LF(1))/501;
F        = [F_LF(1):F_step:F_res];

% LF part of Zt up to F_res
%————————————————————————
Zt_LF    = interp1(F_LF,abs(Zt_C),F);

%% ========================================================================
%                            THEORETICAL VARIATION
%————————————————————————————————————————————————————————————————————————
% The transfer impedance at high frequency is reduced to Ztot = jM12w
%————————————————————————————————————————————————————————————————————————

% Radius of the air-line
% (a : inner radius | b : outer radius)
%————————————————————————————————————
a = (7.19e-3)/2;
```

```
b = (7.94e-3)/2;

% Radius of the hole
%--------------------
a_Hole = (2.9e-3)/2;

% Thickness D of the sheath
%--------------------------
D = b - a;

% Permeability u
%---------------
u0 = 4*pi*1e-7;

F_calc = [F_LF(1):1e4:F_HF(length(F_HF))];

% Conductivity of a copper, brass
%--------------------------------
sigma_IACS = 5.8108e+7      % IACS at 20 deg C
sigma = 0.2*sigma_IACS;     % for brass C85400 (recommended by Wessel Croucamp)
                            % 20% IACS

Zt_calc = Zt_theory(F_calc,a_Hole,a,D,L_CBL,sigma);


%% INTERPOLATION OF ZT AT HF
%--------------------------
% Method: Least mean square
%--------------------------

% Definition of the data to be adjusted
%--------------------------------------
x = [10e6:10e6:1.3e9];
X = log10(F_HF);
Y = 20*log10(Zt_HF);

% The means
%----------------------
X_m = mean(X);
Y_m = mean(Y);

% Calculation of the LMS coefficients
%------------------------------------
n = length(X);
A = (n*sum(X.*Y) - sum(X)*sum(Y))/(n*sum(X.^2) - sum(X).^2);
B = Y_m - A*X_m;

% The approximated Zt from
%-------------------------
Zt_Approx = x.^(A/20).*(10^(B/20));

%% COMBINING THE 2 TRANSFER IMPEDANCE
%------------------------------------
% by interpolation
%-----------------
Zt_Freq = [F' ; F_HF(:,1)];
```

```
Zt_full = [Zt_LF' ; Zt_HF];
Freq    = [300e3:500e3:1000e6];
Zt_CBL  = interp1(Zt_Freq,Zt_full,Freq);

%% PLOTTING
%----------
% Tranfer impedance
figure;
semilogx(F_calc,20*log10(abs(Zt_calc)),'-.k');
grid on;
hold on;
semilogx(x,20*log10(Zt_Approx),'r');
semilogx(F,20*log10(Zt_LF));
semilogx(F_HF,20*log10(Zt_HF));
legend('Vance Zt Model','Slope of the Zt measurement');
xlabel('Frequency in Hz');
ylabel('Transfer impedance in dBOhm\m');
```

B.5 Enclosure SE Calculation in FD

```
clear all;
clc;
close all;

Pos_Num = 1;    %Number of antenna possition used for the investigation


% Chamber Loss in FD obtained from RC calibration
%------------------------------------------------

% Load AVF
%---------
CCF = importdata('Extra data\CH_Loss.csv',',');
F_CCF = CCF(:,1);
CCF   = CCF(:,2);

% Load the measured KPLDA efficiency
%-----------------------------------
LPDA_Eff    = importdata('Extra data\KLPDA4_Eff_dipoleonly.csv','\t');
LPDA_F      = LPDA_Eff(:,1);
LPDA_Eff    = LPDA_Eff(:,2);


% Load Enclosure SE Measurement
%------------------------------
Enc         = load('data\Loop_Stirred_Taped_4H.mat');


%%
%-------------------------------------------------------------------------
%
%                       Extract S_Parameter per stirrer position
%
```

```
%-------------------------------------------------------------------------

for m = 1:Pos_Num
    disp(['Processing Antenna Position: ' num2str(m)]);
    varPos      = ['Position',num2str(m)];
    varPos      = genvarname(varPos);
    Enc_S(m)    = Sparam_per_Angle(Enc.(varPos),72);
end
clear Enc;

% Matching KPLDA efficiency and chamber loss data with the measurement
LPDA_Eff = interp1(LPDA_F,LPDA_Eff,Enc_S(1,1).F);
CH_Loss  = interp1(F_CCF,CCF,Enc_S(1,1).F);


%%
%-------------------------------------------------------------------------
%
%                SHIELDING EFFECTIVENESS COMPUTATION
%
%-------------------------------------------------------------------------

% Load data Spliter-attenuation measured data
% For S1, the first splitter output port is matched to 50 Ohm and the
% second output is conected to the VNA Port.
% For S2, the connection is iverted.

S1 = importdata('Extra data\Split_Feed_Meas_P1_P2_M.s2p',' ',5);
S2 = importdata('Extra data\Split_Feed_Meas_P2_P1_M.s2p',' ',5);

F = Open.data(:,1);
S1.S11 = S1.data(:,2) + 1i*S1.data(:,3);
S1.S21 = S1.data(:,4) + 1i*S1.data(:,5);
S1.S12 = S1.data(:,6) + 1i*S1.data(:,7);
S1.S22 = S1.data(:,8) + 1i*S1.data(:,9);

S2.S11 = S2.data(:,2) + 1i*S2.data(:,3);
S2.S21 = S2.data(:,4) + 1i*S2.data(:,5);
S2.S12 = S2.data(:,6) + 1i*S2.data(:,7);
S2.S22 = S2.data(:,8) + 1i*S2.data(:,9);

% Splitter power attenuation for both channels
P_P1 = interp1(F,abs(S1.S21.^2./((1 - abs(S1.S11).^2).*(1 - abs(S1.S22).^2))),Enc_S(1,1).F);
P_P2 = interp1(F,abs(S2.S21.^2./((1 - abs(S2.S11).^2).*(1 - abs(S2.S22).^2))),Enc_S(1,1).F);

for m = 1:Pos_Num
    SE_Avg(m,:) = (Enc_S(1,m).S21_Avg.^2)./((P_P1' + P_P2').*(1 - Enc_S(1,m).S11_Avg.^2).*(1 - Enc_S(1,m).S22_
end

figure;
semilogx(Enc_S(1,1).F*1e-9,10*log10(1./SE_Avg));
grid on;
hold all;
xlabel('Frequency in GHz');
ylabel('SE in dB');
```

B.6 Function for S-Parameter Extraction for SE Calculation in FD

```
function S = Sparam_per_Angle(Calibration_Pos,Pos_per_Rev)

% Frequency range of the measurement
S.F = Calibration_Pos.Angle0.F;

% [S] Average and Max Calculation
for q = 1:length(S.F)
    for k=0:Pos_per_Rev-1
        p = k*(360/Pos_per_Rev);
        Var = strcat('Angle',num2str(p));
        Var = genvarname(Var);
        S11(q,k+1) = Calibration_Pos.(Var).S11(q);
        S21(q,k+1) = Calibration_Pos.(Var).S21(q);
        S12(q,k+1) = Calibration_Pos.(Var).S12(q);
        S22(q,k+1) = Calibration_Pos.(Var).S22(q);
    end

    % Average reading over one revolution
    S11_Avg(q) = mean(abs(S11(q,:)));
    S21_Avg(q) = mean(abs(S21(q,:)));
    S12_Avg(q) = mean(abs(S12(q,:)));
    S22_Avg(q) = mean(abs(S22(q,:)));

    % Max reading over one revolution
    [S21_Max(q),I(q,1)] = max(abs(S21(q,:)));
    S11_Max(q) = abs(S11(q,I(q,1)));
    S22_Max(q) = abs(S22(q,I(q,1)));
    [S12_Max(q),I(q,1)] = max(abs(S12(q,:)));
    %S22_Max(q) = abs(S22(q,I(q,1)));
end
S.S11_Avg = S11_Avg';
S.S21_Avg = S21_Avg';
S.S12_Avg = S12_Avg';
S.S22_Avg = S22_Avg';

S.S11_Max = S11_Max';
S.S21_Max = S21_Max';
S.S12_Max = S12_Max';
S.S22_Max = S22_Max';

S.S21 = S21;
S.S11 = S11;
S.S12 = S12;
S.S22 = S22;
```

B.7 Enclosure SE Calculation in TD for CH1

```
%*************************************************************************
% Code for SE calculation
%
% Measurement Setup
%--------------------
% Direct pulse measurement
%
%    ___________      ________________     ___________
%    |  PG     |  =>  | Attenuators |  => | RATTY |
%    ___________      ________________     ___________
%
%
% RC-pulse measurement
%                              RC
%                  ___________________________________
%                  |                                 |
%    ___________   | ________________   _________    |    ___________
%    |  PG     |  => |->| Enclosure |    | LPDA |    |  => | RATTY |
%    ___________   | ________________   _________    |    ___________
%                  |                                 |
%                  ___________________________________
%
%*************************************************************************


clc;
clear all;
close all;

% Loading necessary data
% ----------------------
% set(0,'DefaultFigureWindowStyle','docked');

% Ratty sampling frequency
Fs = 1800e6;

% Channel 1 frequency range
Freq_CH1 = [300e6:1e6:800e6];

% Chamber Loss in FD
CCF = importdata('Extra data\CH_Loss.csv',',');
F_CCF = CCF(:,1);
CCF   = CCF(:,2);

% LPDA measured Efficiency
LPDA_Eff    = importdata('Extra data\KLPDA4_Eff_dipoleonly.csv','\t');
LPDA_F      = LPDA_Eff(:,1);
LPDA_Eff    = LPDA_Eff(:,2);

% Load measurement data
Enc       = load('Extra data\Loop_LU.mat');

%%
% Extract S_Parameter per angle
for m = 1:1
    disp(['Processing Antenna Position: ' num2str(m)]);
```

```
    varPos      = ['Position',num2str(m)];
    varPos      = genvarname(varPos);
    Enc_S(m)    = Sparam_per_Angle(Enc.(varPos),72);
end


%%
%*************************************************************************
%
%                RC RADIATED POWER ESTIMATION USING RATTY DATA
%
%*************************************************************************

% Attenuation used for the RC measurement
CH1_Att_dB = 0 + 8;
Ext_Att_dB = 0;
RC_CH1_Att    = 10^((CH1_Att_dB+Ext_Att_dB)/20);


% CHANNEL 1
% ----------
% Laod extracted RATTY pulses
hinfo = hdf5info('Radiated_P_CH1.h5');

for m = 1:length(hinfo.GroupHierarchy.Datasets)-1
    datasetname = strcat('/Stirrer',num2str(m));
    CH1(m,:,:) = hdf5read('Radiated_P_CH1.h5',datasetname)*B2V*RC_CH1_Att/Gain_CH1;
end

% Read Time variable for Channel 1
T_CH1 = hdf5read('Radiated_P_CH1.h5','/Time');


%-------------------------------------------------------------------------
%                             RC PULSE SPECTRUM
%-------------------------------------------------------------------------
for m = 1:length(CH1(:,1,1))
    for n = 1:length(CH1(1,1,:))
        % compute the fft of the current TD mean pulse
        [X_RC_CH1,Amp_X_RC_CH1(n,:),F_RC_CH1] = FFT_Pulse(T_CH1,CH1(m,:,n));

    end
    clear X_RC_CH1;
    Amp_RC_CH1_Avg(m,:) = mean(Amp_X_RC_CH1(:,1:length(F_RC_CH1)));
end

clear Amp_X_RC_CH1;

% Average of Radiated_P
Radiated_P_CH1_Avg = mean(Amp_RC_CH1_Avg);

% Matching the RC attenuation data and the antenna efficiency with the
% measurement frequency range
CCF_CH1_S = transpose(interp1(F_CCF,CCF,Freq_CH1));
LPDA_Eff_CH1 = interp1(LPDA_F,LPDA_Eff,Freq_CH1);
```

```
Loop_S11 = interp1(Enc_S(1,1).F,Enc_S(1,1).S22_Avg,Freq_CH1);
Radiated_P_CH1 = interp1(F_RC_CH1,Radiated_P_CH1_Avg,Freq_CH1)./(CCF_CH1.*(1 - Loop_S11.^2));

figure;
plot(Freq_CH1,20*log10(Radiated_P_CH1));
grid on;
title('Radiated Signal on KLPDA2');

% Radiated_Power
P_Radiated_CH1 = Radiated_P_CH1.^2;


%%
%*************************************************************************
%
%                          DIRECT PULSE INPUT POWER
%
%*************************************************************************

% Attenuation used for the Input measurement
CH1_Att_dB = 2 + 13;
Ext_Att_dB = 66;
Coupler_dB = 20;
Input_CH1_Att    = 10^((CH1_Att_dB+Ext_Att_dB+Coupler_dB)/20);


% CHANNEL 1
% ----------
hinfo = hdf5info('Input_P_CH1.h5');

for m = 1:length(hinfo.GroupHierarchy.Datasets)-1
    datasetname = strcat('/Stirrer',num2str(m));
    CH1 = hdf5read('Input_P_CH1.h5',datasetname)*B2V*Input_CH1_Att/Gain_CH1;
end

% Time variable for Channel 1
T_CH1 = hdf5read('Input_P_CH1.h5','/Time');

%-------------------------------------------------------------------------
%                             DIRECT PULSE SPECTRUM
%-------------------------------------------------------------------------
% compute the fft of the current TD mean pulse
[X_Input_CH1,Amp_X_Input_CH1,F_Input_CH1] = FFT_Pulse(T_CH1,CH1);

clear Amp_X_Input_CH1;
% Average of the all Radiated_P

Input_P_CH1_Avg = abs(mean(X_Input_CH1'));
Input_P_CH1_Avg = Input_P_CH1_Avg(1:length(F_Input_CH1));

Input_P_CH1 = interp1(F_Input_CH1,Input_P_CH1_Avg,Freq_CH1);

%%
%-------------------------------------------------------------------------
%
%                           SE CALCULATION
```

```
%
%------------------------------------------------------------------------
% Load splitter data
S1 = importdata('Extra data\Split_Feed_Meas_P1_P2_M.s2p',' ',5);
S2 = importdata('Extra data\Split_Feed_Meas_P2_P1_M.s2p',' ',5);

S1 = importdata('Extra data\Split_Feed_Meas_P1_P2_M.s2p',' ',5);
S2 = importdata('Extra data\Split_Feed_Meas_P2_P1_M.s2p',' ',5);

F = Open.data(:,1);
S1.S11 = S1.data(:,2) + 1i*S1.data(:,3);
S1.S21 = S1.data(:,4) + 1i*S1.data(:,5);
S1.S12 = S1.data(:,6) + 1i*S1.data(:,7);
S1.S22 = S1.data(:,8) + 1i*S1.data(:,9);

S2.S11 = S2.data(:,2) + 1i*S2.data(:,3);
S2.S21 = S2.data(:,4) + 1i*S2.data(:,5);
S2.S12 = S2.data(:,6) + 1i*S2.data(:,7);
S2.S22 = S2.data(:,8) + 1i*S2.data(:,9);

% Splitter power attenuation for both channels
P_P1 = interp1(F,abs(S1.S21.^2./((1 - abs(S1.S11).^2).*(1 - abs(S1.S22).^2))),Enc_S(1,1).F);
P_P2 = interp1(F,abs(S2.S21.^2./((1 - abs(S2.S11).^2).*(1 - abs(S2.S22).^2))),Enc_S(1,1).F);

SE = (P_Input_CH1./P_Radiated_CH1)./ (P_P1 + P_P2);

figure;
plot(Freq_CH1*1e-9,10*log10(SE));
grid on;
title('Enclosure SE')
```

B.8 Enclosure SE Calculation in TD for CH2

```
%************************************************************************
% Code for SE calculation
%
% Measurement Setup
%--------------------
% Direct pulse measurement
%
%    ---------      ---------------     ---------
%    |  PG   |  =>  | Attenuators |  => | RATTY |
%    ---------      ---------------     ---------
%
%
% RC-pulse measurement
%                                RC
%                  ---------------------------------
%                  |                               |
%    ---------     |  ---------------    --------  |     ---------
%    |  PG   |  => |->| Enclosure |    | LPDA |  |  => | RATTY |
%    ---------     |  ---------------    --------  |     ---------
%                  |                               |
```

```
%                  ____________________________
%
%*************************************************************************


clc;
clear all;
close all;

% Constants and measurement parameters
% ____________________________________

set(0,'DefaultFigureWindowStyle','docked');

% Ratty sampling frequency
Fs = 1800e6;
F_Mixer = 1500e6;

% Frequency range for RATTY CHannel2
Freq_CH2 = [800e6:1e6:1200e6];

% Chamber Loss in FD
%____________________
% Load RC loss data (AVF)
CCF = importdata('Extra data\CH_Loss.csv',',');
F_CCF = CCF(:,1);
CCF   = CCF(:,2);

% LPDA Efficiency data
LPDA_Eff    = importdata('Extra data\KLPDA4_Eff_dipoleonly.csv','\t');
LPDA_F      = LPDA_Eff(:,1);
LPDA_Eff    = LPDA_Eff(:,2);

Enc       = load('Extra data\Loop_LU.mat');
%%
% Extract S_Parameter per angle
for m = 1:1
    disp(['Processing Antenna Position: ' num2str(m)]);
    varPos      = ['Position',num2str(m)];
    varPos      = genvarname(varPos);
    Enc_S(m)    = Sparam_per_Angle(Enc.(varPos),72);
end


%%
%*************************************************************************
%
%                              RADIATED POWER
%
%*************************************************************************

% Attenuation used for the RC measurement
CH2_Att_dB = 0 + 2;
Ext_Att_dB = 0;
Ext_Att = 10^(Ext_Att_dB/20);
```

```
% Load RATTY Gain
RATTY_Gain = load('Extra data\RATTY_Cal.mat');

% RC MEasurement Gain and attenuation
RC_Gain.CH2(1,:)    =  10.^(RATTY_Gain.C2_gain(0+1,2+1,:)/20);

% Read CHANNEL2 Extratced Pulses
% ---------------------------------
hinfo = hdf5info('Radiated_P_CH2.h5');

for m = 1:length(hinfo.GroupHierarchy.Datasets)-1
    datasetname = strcat('/Stirrer',num2str(m));
    CH2(m,:,:) = hdf5read('Radiated_P_CH2.h5',datasetname)*Ext_Att;
end

% Time variable for Channel 2
T_CH2 = hdf5read('Radiated_P_CH2.h5','/Time');


%-------------------------------------------------------------------------
%                              RC PULSE SPECTRUM
%-------------------------------------------------------------------------
for m = 1:length(CH2(:,1,1))
    for n = 1:length(CH2(1,1,:))
        % compute the fft of the current TD mean pulse
        [X_RC_CH2,Amp_X_RC_CH2(n,:),F_RC_CH2] = FFT_Pulse(T_CH2,CH2(m,:,n));

    end
    clear X_RC_CH2;
    Amp_RC_CH2_Avg(m,:) = mean(Amp_X_RC_CH2(:,1:length(F_RC_CH2)));
    Amp_RC_CH2_Max(m,:) = max(Amp_X_RC_CH2(:,1:length(F_RC_CH2)));
end

clear Amp_X_RC_CH2;

% Remove mixer frequency from data
F_RC_CH2 = F_Mixer - F_RC_CH2;

RC_Gain.CH2 = interp1(F_Mixer - RATTY_Gain.fc2, RC_Gain.CH2,Freq_CH2);
Radiated_P_CH2_Avg = mean(Amp_RC_CH2_Avg);
Radiated_P_CH2_Max = mean(Amp_RC_CH2_Max);

% Chamber loss correction
CCF_CH2 = interp1(F_CCF,CCF,Freq_CH2);
LPDA_Eff_CH2 = interp1(LPDA_F,LPDA_Eff,Freq_CH2);
CCF_CH2_S = CCF_CH2'

LPDA_S11 = interp1(Enc_S(1,1).F,Enc_S(1,1).S11_Min,Freq_CH2);
Radiated_P_CH2 = interp1(F_RC_CH2,Radiated_P_CH2_Max,Freq_CH2)./(LPDA_Eff_CH2.*CCF_CH2.*(1 - abs(LPDA_S11).^2)
Radiated_P_CH2 = Radiated_P_CH2./RC_Gain.CH2;

figure;
plot(Freq_CH2,20*log10(Radiated_P_CH2));
grid on;
title('Radiated Signal on KLPDA2');
```

```
% Radiated_Power
P_Radiated_CH2 = Radiated_P_CH2.^2;


%%
%*************************************************************************
%
%                           DIRECT PULSE CHARACTERISATION
%
%*************************************************************************

% Attenuation used for the Input measurement
CH2_Att_dB = 2 + 0;
Ext_Att_dB = 66;
Coupler_dB = 20;
Ext_Att = 10^((Ext_Att_dB+Coupler_dB)/20);


% Input Pulse Gain and attenuation
Pulse_Gain.CH2(1,:)    =  10.^(RATTY_Gain.C2_gain(2+1,0+1,:)/20);

% Load extracted pulses  for CHANNEL 2
% ------------------------------------
hinfo = hdf5info('Input_P_CH2.h5');

for m = 1:length(hinfo.GroupHierarchy.Datasets)-1
    datasetname = strcat('/Stirrer',num2str(m));
    CH2_Pulse = hdf5read('Input_P_CH2.h5',datasetname).*Ext_Att;
end

% Time variable for Channel 1
T_CH2 = hdf5read('Input_P_CH2.h5','/Time');

%-------------------------------------------------------------------------
%                             DIRECT PULSE SPECTRUM
%-------------------------------------------------------------------------

% compute the fft of the current TD mean pulse
[X_Input_CH2,Amp_X_Input_CH2,F_Input_CH2] = FFT_Pulse(T_CH2,CH2_Pulse);

clear Amp_X_Input_CH2;

% Remove mixer frequency from data
F_Input_CH2 =  F_Mixer - F_Input_CH2;

Pulse_Gain.CH2 = interp1(F_Mixer-RATTY_Gain.fc2,Pulse_Gain.CH2,Freq_CH2);

Input_P_CH2_Avg = abs(mean(X_Input_CH2'));
Input_P_CH2_Avg = Input_P_CH2_Avg(1:length(F_Input_CH2));

Input_P_CH2 = interp1(F_Input_CH2,Input_P_CH2_Avg,Freq_CH2)./Pulse_Gain.CH2;
Loop_S11 = interp1(Enc_S(1,1).F,Enc_S(1,1).S22_Min,Freq_CH2);

% Input power correction
P_Input_CH2 = (Input_P_CH2.^2).*((1 - Loop_S11.^2));
```

```
%%
%-------------------------------------------------------------------------
%
%                           SE CALCULATION
%
%-------------------------------------------------------------------------


% Load data
S1 = importdata('Extra data\Split_Feed_Meas_P1_P2_M.s2p',' ',5);
S2 = importdata('Extra data\Split_Feed_Meas_P2_P1_M.s2p',' ',5);

S1 = importdata('Extra data\Split_Feed_Meas_P1_P2_M.s2p',' ',5);
S2 = importdata('Extra data\Split_Feed_Meas_P2_P1_M.s2p',' ',5);

F = Open.data(:,1);
S1.S11 = S1.data(:,2) + 1i*S1.data(:,3);
S1.S21 = S1.data(:,4) + 1i*S1.data(:,5);
S1.S12 = S1.data(:,6) + 1i*S1.data(:,7);
S1.S22 = S1.data(:,8) + 1i*S1.data(:,9);

S2.S11 = S2.data(:,2) + 1i*S2.data(:,3);
S2.S21 = S2.data(:,4) + 1i*S2.data(:,5);
S2.S12 = S2.data(:,6) + 1i*S2.data(:,7);
S2.S22 = S2.data(:,8) + 1i*S2.data(:,9);

% Splitter power attenuation for both channels
P_P1 = interp1(F,abs(S1.S21.^2./((1 - abs(S1.S11).^2).*(1 - abs(S1.S22).^2))),Enc_S(1,1).F);
P_P2 = interp1(F,abs(S2.S21.^2./((1 - abs(S2.S11).^2).*(1 - abs(S2.S22).^2))),Enc_S(1,1).F);

SE = (P_Input_CH2./P_Radiated_CH2)./ (P_P1 + P_P2);

figure;
plot(Freq_CH2*1e-9,10*log10(SE));
grid on;
title('Enclosure SE');
```